PHOTOVOLTAICS LARGE AND SMALL:

ATOMICALLY THIN SEMICONDUCTOR GROWTH AND KILOWATT-SCALE
TRANSMISSIVE PHOTOVOLTAIC SYSTEMS

A DISSERTATION

SUBMITTED ON THE TWENTY SECOND DAY OF FEBRUARY 22 2019

TO THE DEPARTMENT OF PHYSICS

IN PARTIAL FULFILLMENT OF THE REQUIREMENTS

OF THE SCHOOL OF SCIENCE AND ENGINEERING

OF TULANE UNIVERSITY

FOR THE DEGREE

OF

DOCTOR OF PHILOSOPHY

BY

_____

JOHN T. ROBERTSON

APPROVED: _____

MATTHEW D. ESCARRA, Ph.D.
DIRECTOR

_____

JIANG WEI, Ph.D.

_____

DOUGLAS B. CHRISEY, Ph.D.

PHOTOVOLTAICS LARGE AND SMALL:

ATOMICALLY THIN SEMICONDUCTOR GROWTH AND KILOWATT-SCALE
TRANSMISSIVE PHOTOVOLTAIC SYSTEMS

AN ABSTRACT

SUBMITTED ON THE TWENTY SECOND DAY OF FEBRUARY 22 2019

TO THE DEPARTMENT OF PHYSICS

IN PARTIAL FULFILLMENT OF THE REQUIREMENTS

OF THE SCHOOL OF SCIENCE AND ENGINEERING

OF TULANE UNIVERSITY
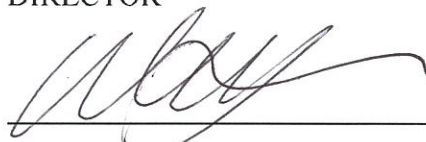
FOR THE DEGREE

OF

DOCTOR OF PHILOSOPHY

BY

_____

JOHN T. ROBERTSON

APPROVED: _____
MATTHEW D. ESCARRA, Ph.D.
DIRECTOR

_____
JIANG WEI, Ph.D.

_____
DOUGLAS B. CHRISEY, Ph.D.

ABSTRACT

This dissertation describes several key developments in semiconductor devices and technologies designed for solar power conversion and other applications. The first development is of two new growth techniques for producing large-area two-dimensional molybdenum disulfide (MoS_2). Such two-dimensional materials have the potential to miniaturize photovoltaic volume and mass by orders of magnitude without sacrificing performance. While large-scale 2D-material-based photovoltaics have not yet been realized, large-area growths such as those described in this dissertation provide meaningful progress toward that goal. The described techniques enable 2D MoS_2 thickness control on the order of angstroms and increase 2D MoS_2 growth speed by two orders of magnitude relative to the current state of the art. Furthermore, the grown materials are developed into preliminary optoelectronic devices, with performance characterization, as a step toward more advanced photovoltaic devices.

The second development presented in this dissertation is the design, fabrication, test, and analysis of a kW-scale hybrid spectrum-splitting photovoltaic module. The module is designed to be transmissive to incident infrared radiation, allowing for infrared light to be separately collected by a thermal receiver, while simultaneously collecting high-energy visible and ultraviolet light via photovoltaics. A system is built and tested on an outdoor testbed and shows 75% total power conversion efficiency (thermal and electric) of the incident solar spectrum, surpassing the capability of conventional photovoltaics. This

high efficiency and combination of electrical and thermal power accelerates solar energy penetration into new applications requiring multiple power streams.

Across these varied length scales, this dissertation gives glimpses into new innovations throughout the photovoltaic and semiconductor fields and aims to share this knowledge and outlook with the next generation of researchers.

ACKNOWLEDGEMENTS

I dedicate this dissertation to my mother and father, who love and support me without

hesitation.

I give deep thanks to Dr. Matthew Escarra, who taught and encouraged me constantly

I am also grateful to Dr. Jiang Wei and Dr. Doug Chrisey for their mentorship during my

studies and for serving on my dissertation committee.

I give endless thanks to my wife Ellie, who pushes me to reach my potential.

And to God, through whom I do all things with joy.

To Reach For The Stars.

FORWARD

Before I knew much about them, I had a fascination with semiconductors. I didn't know the details of their operation, but I understood that they were important. Semiconductors seemed to underpin virtually every new electronic technology developed during the past half century, a period of time that saw an explosion in technological capability. They have revolutionized the way we live, work, and interact with each other and our environment. My goal during my PhD program was to better understand these miracle materials, and to contribute to the field during the process.

This journey led me to the world of photovoltaics, an application that is growing to be among the most important uses of semiconductors. I do not see photovoltaics as the one true way to solve the world's energy needs, or as the sole antidote to climate change. Rather, I see photovoltaics as a powerful and underused technology that has not yet reached its maturity. Every year, solar cell technologies become more efficient, smaller, and less expensive to manufacture. As solar cells mature, more applications will become available. Among these applications, I am personally most excited about the prospects of electric vehicle-integrated photovoltaics, turning every car into a mobile power plant complete with storage. I also believe that spaceflight photovoltaics will continue to pioneer new solar cell technologies, as has done from the beginning. Both of these applications share a need for high-efficiency and lightweight solar cells, and will continue to drive innovation in these spaces. The work presented within this dissertation is directly applicable to these goals and explores new avenues for reaching them. I am

hopeful that this work may play a role in advancing these fields, and that photovoltaics

will become a more mainstream means of producing electrical power in the near future.

TABLE OF CONTENTS

TABLES

FIGURES

1 INTRODUCTION

Photovoltaics (PV) are a class of semiconductor devices that convert incident optical power to electrical power in a circuit. [1] The sun bathes the average square meter of earth with approximately one kilowatt of optical power during daylight hours, and photovoltaics that convert sunlight to power are commonly called "solar cells". Solar cells are commonly used both terrestrially and in spaceflight applications, and the solar resource reaches a larger 1357 W/m^2 in space.[2] As the 21st century progresses, it has become increasingly clear that photovoltaic conversion of sunlight into electricity will play a major role in meeting the future energy needs of the planet.[3] This dissertation investigates two distinct avenues for future photovoltaic collection improvement and innovation. The first is the development of two-dimensional (2D) semiconductors and their prospects for ultra-thin photovoltaics and optoelectronic devices. The second is the optimized collection of full-spectrum sunlight using hybrid photovoltaic cells. Through these two paths, we seek to improve photovoltaics in terms of energy density, cost, and efficiency. We will also discuss some specific applications that would benefit from these innovations, notably in industrial-scale power generation, building-integrated PV, vehicle-integrated PV, and spacecraft solar arrays.

1.1 2D MATERIALS

Although we live in a world with three physical dimensions, a class of materials exist that scientists collectively refer to as two-dimensional (2D) materials.[4,5] These 2D materials are not truly spatially two dimensional. By having a sufficiently small 3rd dimension on the order of angstroms they are quantum mechanically confined to two dimensions and electronically behave as if only two dimensional. In 2004, Andre Geim and Konstantin Novoselov reported their experimental discovery of graphene, a 1-atom-thick sheet of carbon, and the first confirmed 2D material.[6] In 2010, only six years later, they were jointly awarded the Nobel prize in physics for their discovery of graphene and for effectively creating an entire new research field of 2D materials.[7] Impressive already was the fact that graphene could even exist in a singular atomic layer without destroying itself through environmental reactions or surface-energy distortions. More incredible still was the large field effect in graphene-based electronic devices, with possible carrier mobility up to 200,000 $cm^2V^{-1}s^{-1}$.[8] These sub-nanometer thick films possessed field effect mobilities and mechanical robustness equal to, or better than, macroscopic crystals, ushering in a new world of nanoscale device possibilities.

Since 2004, it has become clear that semimetal graphene is merely one member of a larger 2D materials family, including a host of 2D semiconductors with a wide range of bandgaps[9] and 2D insulators such as hexagonal boron nitride (hBN).[10,11] In this section we go over the history and physics of 2D materials, with emphasis on 2D semiconductors, and MoS_2 as the primary example and subject of this dissertation work.

1.1.1 History of Van Der Waals Materials

The common characteristic of all 2D materials is the presence of covalently bonded molecular sheets, with adjacent sheets weakly bonded to each other by Van Der Waals forces. Before 2D materials were experimentally isolated in 2004, their existence as a unique family of materials was known about and researched. For example, graphite had been analyzed, experimentally and theoretically, as an intercalation compound in which intercalating agents could penetrate the unbonded space between adjacent basal planes to reveal new properties.[12] Methods to isolate graphene, such as cleavage, had also been proposed prior to 2004.[13] However, before 2004, no experimental evidence existed that a single atomic layer of graphite could physically exist without quickly deforming into globular graphite clusters.[14]

In addition to academic research interests, an original application of 2D materials such as graphite and MoS_2 was as solid-state lubricant. Due to the Van Der Waals forces within their bulk crystals, these 2D materials acted as a low-friction powder used in automotive components such as ball bearings. MoS_2 is a binary 2D material that naturally occurs in the form of the mineral molybdenite[15], but unlike graphene is a semiconductor with a bandgap. By the 1970's MoS_2 was being investigated in its bulk form to determine its electronic band properties and potential, although its 2D form had not yet been conceived.[16,17]

The crystal structure of MoS_2 is shown in Figure 1-1, in which all bonding within each monolayer is covalent, whereas interlayer bonding is Van Der Waal in nature. MoS_2 is composed primarily of the 2H hexagonal phase, in which an internal layer of Mo atoms (purple) is covalently bound between two layers of S atoms. However, the S atoms do

not have any dangling bonds above or below the molecular sheet, making each layer

relatively chemically stable and unreactive. This structure is also found in other

compounds in the transition metal dichalcogenides (TMDC) of formula MX_2 (M = Mo,

W, X = S, Se, Te), which comprise the most studied group of 2D semiconductors.[5]
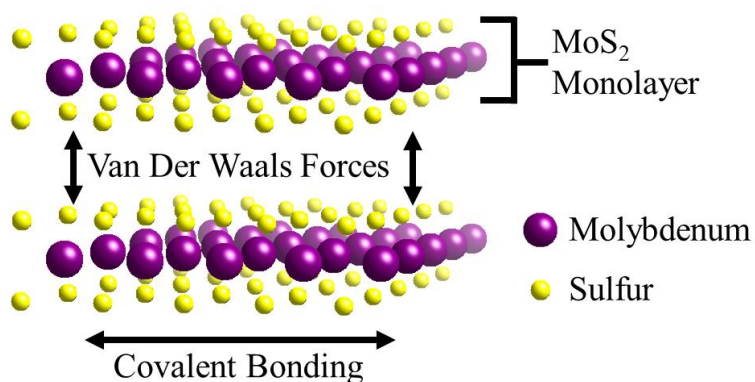
Figure 1-1: MoS_2 crystal structure

It was not until 2010 that MoS_2 became the first experimentally isolated monolayer

TMDC, six years after the discovery of graphene.[18,19] While the most prominent feature

of graphene was its large field effect mobility in monolayer form, MoS_2 in contrast

possessed a relatively small field-effect mobility, but instead contained the amazing

ability to transition from an indirect bandgap semiconductor to a direct gap

semiconductor in the monolayer form.[19,20] In the years following the discovery of

monolayer MoS_2, many more remarkable properties would emerge, making 2D MoS_2 and

other TMDC's one of the top research areas in all of physics.

1.1.2 Transition Metal Dichalcogenides (TMDC's)

Of all 2D materials, TMDC's are the most relevant to optoelectronic applications,

including photovoltaics, due to their visible and NIR direct bandgaps in monolayer form.

Therefore, for the scope of this dissertation, we will primarily focus on the semiconductor 2D TMDC's, of which MoS_2 is the most commonly studied due to its long-term stability in air. The bandgaps of TMDC's range from 1.85 eV (MoS_2) to 1.02 eV ($MoTe_2$), a broad spread that is well-suited for photovoltaic collection of the solar spectrum. In its bulk form, MoS_2 has an indirect bandgap of 1.3 eV, while its monolayer form possesses a 1.85 eV direct bandgap. This remarkable transition, which takes place in the "few-layer" regime of 1-5 atomic layers, suddenly made MoS_2 a top candidate for the ultra-thin optoelectronic devices of the future. In addition, this indirect-to-direct transition was also observed in WS_2, $MoSe_2$, and WSe_2.[21] Therefore, although the majority of the work discussed in this thesis features MoS_2 as the stable test piece, it is expected that analogous qualities and capabilities will be found in the other TMDC's with due progress.

The easiest way to communicate the promise of 2D TMDC's is to highlight their extraordinary measured attributes. For example, monolayer MoS_2, passivated by submersion in a superacid, produced 99% photoluminescence quantum yield, a quality exhibited by only a few other known materials.[22] With the aid of index-matched metal back reflector contacts, TMDC-based photovoltaics achieved optical absorption $> 90\%$[23] and 50% photovoltaic external quantum efficiency.[24] Furthermore, when encapsulated within 2D hBN and edge-contacted with graphene, MoS_2 transistors can exhibit Hall mobility of up to 34,000 $cm^2V^{-1}s^{-1}$.[25] All of these properties occur within materials only nanometers thick. In fact, the attributes arising from quantum-confined few-layer TMDC's display stronger light interaction and field effect response than their bulk counterparts; like a candle that produces more light than a lighthouse, these effects are

counterintuitive and enable device miniaturization that is simply not possible with traditional 3D materials.

While the world-changing possibilities of 2D materials have always been present, they are tempered by the difficulty in obtaining and engineering large-scale 2D samples. In light of this limitation, much of the work described in this dissertation regarding 2D materials revolves around large-scale growth techniques and resultant device fabrication. Therefore, we now begin a detailed discussion of the synthesis history of 2D materials, with a focus on MoS_2, and an emphasis on the needs that still must be addressed before 2D material development can progress further.

1.1.3   2D TMDC Growth Techniques

The critical requisite for the advancement of 2D materials into useful technologies is large-scale material growth without sacrificing intrinsic material quality. When graphene was originally obtained in 2004, it was procured using the "mechanical exfoliation" technique.[6] Mechanical exfoliation is a simple but effective way of isolating 2D material monolayers by peeling them away using scotch tape. By repeatedly pressing tape against a bulk 2D sample and peeling it off, some flakes inevitably are stuck to the adhesive on the tape and peeled away. When the tape is then pressed against a substrate, flakes can be re-deposited onto the substrate. By repeating this process, a large and random scattering of 2D flakes of various sizes is deposited on a substrate, and monolayers can be identified via optical microscope.[26,27] Mechanical exfoliation still remains the easiest and most common way of obtaining flakes of 2D materials for scientific analysis, including 2D TMDC's. However, mechanical exfoliation produces isolated flakes of material which are rarely larger than 50 microns wide. Because of this,

mechanical exfoliation is not a good candidate for large-scale 2D material synthesis, and therefore is not suitable for practical commercial applications such as photovoltaics or detectors.

In order for MoS_2 and other TMDC's to be incorporated into commercial-scale devices, sheets of 2D materials must be synthesized on the scale of tens of centimeters, if not larger. The films must be continuous and uniform. At the same time, the quality of these large sheets must be comparable to benchmark values from exfoliated samples. Once all of these criteria are met, the synthesis of 2D materials must be further developed to be cost-effective and economically viable. Several growth techniques have been developed that achieve combinations of these criteria, and two more are here presented in this dissertation as original contributions to this body of work.

Discussion of large-scale TMDC growth must start with molybdenum oxide-precursor chemical vapor deposition (CVD). The first reported large-scale CVD growth of a 2D TMDC was by Y. Lee in 2012,[28] which set the stage for dozens of follow-on growth innovations and improvements. The growth accomplished by Lee et al. worked by evaporating solid MoO_3 powder precursor in a 650 ℃ vacuum tube furnace. Placed directly above the MoO_3 powder are Si/SiO_2 substrates spin-coated with a reduced graphene oxide (rGO) solution, which acted as a seed promoter for MoS_2 nucleation. Meanwhile, upstream and in a cooler region of the furnace, solid sulfur precursor was evaporated and flowed toward the MoO_3 and substrates via N_2 carrier gas. The MoO_3 and sulfur vapors react in the proximity of the substrates, and form crystalline 2D MoS_2 deposits with the aid of the rGO.

Although the first report by Lee in 2012 achieved only modest carrier mobility of $0.02 \text{cm}^2\text{V}^{-1}\text{s}^{-1}$ and showed little control over the final MoS_2 thickness, subsequent reports over the past seven years have steadily improved the technique to give very high quality MoS_2 crystals with precise thickness control. For example, Yu and coworkers in 2013 utilized $MoCl_5$ as the precursor instead of MoO_3 and used tight control of sulfur partial pressure to yield layer-by-layer control of MoS_2 thickness across an entire wafer.[29] Although the carrier mobility of this method remained in the low range of 0.003 – 0.03 $\text{cm}^2\text{V}^{-1}\text{s}^{-1}$, the uniformity and thickness control was a noteworthy advancement. In 2015, Dumcenco et al. demonstrated that monolayer MoS_2 could be epitaxially grown on annealed sapphire substrates, reducing defects at grain boundaries and yielding incredible carrier mobilities of $22 – 25 \text{ cm}^2\text{V}^{-1}\text{s}^{-1}$, although with growth confined to a region only a few millimeters wide.[30] This growth represents near-ideal MoS_2, and is only held back by its requirement for expensive sapphire lattice-matched substrates, long growth time, and relatively small scale.

In addition, many other innovations have led to improvements in the basic MoO_3-precursor setup. For example, solid sulfur source can be replaced with gaseous H_2S to improve the control of sulfur source into the reaction.[31] The critical interplay between the concentrations of oxygen and hydrogen within the growth chamber has also been studied, with hydrogen injected to reduce oxidation, and oxygen injected to increase active bonding site density.[32] Ultimately, some trace presence of oxygen in the chamber proved critical to obtaining large MoS_2 single domains up to 350 μm wide with carrier mobility up to $90 \text{ cm}^2\text{V}^{-1}\text{s}^{-1}$.[33] However, the very nature of these results shows that the sensitivity of these reactions is high; for example, researchers often anecdotally talk of

obtaining different growth results based on the weather on any particular day. In addition, the CVD reaction tends to be limited to smaller areas on the order of a few mm^2, and so large-scale throughput and reliability innovations now come into focus before large-scale implementation can progress.

1.1.4 Potential Applications of 2D Semiconductors

There is an old phrase common in the world of energy research: "Even if it works, will it matter?" This phrase is meant to check new technologies and materials that carry excitement due to their novelty, but fundamentally will not outperform established status-quo technologies. With this caution in mind, we seek to answer the question: even if large-scale, high-quality 2D TMDC growth is perfectly accomplished, how useful would it be?

First, MoS_2-based field-effect transistors (FET) have the potential to be miniaturized beyond the lower size limits of silicon transistors. This has already been experimentally demonstrated on the laboratory scale, as a 2 nm thick sheet of few-layer MoS_2 has been used, in conjunction with a single wall carbon nanotube gate electrode, to make the world's smallest transistor with a gate dielectric thickness of 1 nm and an effective channel length of $1 - 4$ nm.[34] This miniaturization is due partially to the chemical stability of MoS_2 arising from its lack of out-of-plane bonding with neighboring atoms. However, MoS_2 transistors also possess intrinsically smaller source-drain tunneling currents due to the relatively large electron specific mass of MoS_2, allowing MoS_2-based transistors to be reduced to atomic thicknesses and lengths with minimal tunneling leakage.[34] As Moore's law continues to play out, and the size of transistors continues to shrink, MoS_2 presents a means to shrink transistors smaller than is possible with silicon.

A second potential application for large-area MoS_2, and one more relevant to the themes of this thesis, is in ultra-sensitive photodetection. Owing to the direct bandgap of monolayer MoS_2, photons incident on MoS_2 device active areas can be converted to conduction electrons very efficiently. In 2013, a monolayer MoS_2 phototransistor demonstrated a responsivity of 880 A/W under 24 μWcm^{-2} illumination at 561 nm, roughly two orders of magnitude higher than state-of-the-art silicon avalanche photodiodes.[35] This performance can be attributed to the direct bandgap of monolayer MoS_2 and high absorption coefficient of $\sim 5.0e^{-5}$ cm^{-1}. [36] The large optical absorption of monolayer MoS_2 is also due to a large density of states for d-orbital dipole transitions in MoS_2, in addition to the excitonic coupling of these states.[37] These two effects combine to yield a particularly large absorption coefficient, which combined with the ability of MoS_2 to be thinned to a few nanometers, makes MoS_2 uniquely qualified to form ultra-thin photodetectors.

For many of the same reasons that MoS_2 has distinguished itself as a high responsivity photodetector with nanometer-scale thickness, MoS_2 and other TMDC's are outstanding candidates to achieve photovoltaic conversion efficiencies comparable to traditional semiconductor materials, while requiring three order of magnitude thinner photovoltaics and lower mass. In 2013, M. Bernardi and coworkers determined that monolayer TMDC photovoltaic devices could obtain a power conversion density of 450 – 1800 kW/kg, two orders of magnitude higher than the 54 kW/kg of the current best state-of-the-art gallium arsenide cells. Furthermore, D. Jariwala and coworkers calculated via detailed balance in 2017 that 2D TMDC-based photovoltaics can achieve a maximum power conversion efficiency of 26%-27%, similar to silicon and other established technologies. Based on

these numbers, we may entertain some specific examples of the impact of this reduced PV mass. Epitaxially lifted off (ELO) GaAs solar cells represent the current best power density for photovoltaic cells, with a bare cell power density of ~54 kW/kg, or 18.5 g/kW.[38] In contrast, it is predicted that 2D MoS_2/WS_2 heterostructures could achieve power densities as high as 2500 kW/kg, or 0.4 g/kW.[37] By subtracting these two, it can be seen that 2D-based photovoltaics have the potential to reduce solar cell mass by up to 18.1 g/kW. By similar arguments, crystalline silicon photovoltaics 35 μm thick possess power densities as low as 2.5 kW/kg, corresponding to 400 g/kW, 399.96 g/kW larger than the potential 2D-based photovoltaic case. One application that requires large arrays of lightweight photovoltaics is spaceflight power generation. For example, the largest current in-space solar array powers the international space station (ISS), outputting up to 120 kW of electrical power. Considering that the ISS currently uses silicon-based photovoltaics, 2D photovoltaics alone could reduce the mass of the ISS solar arrays by ~48 kg relative to silicon, a significant mass reduction for objects launched into space. Furthermore, this reduction in cell mass will certainly also lead to reduced mass of the support structures and substrates adjacent to the cells. Even in the comparison case of ELO GaAs cells, 2D photovoltaics would lead to a mass reduction of ~2.2 kg for the ISS solar arrays and make the photovoltaic mass itself practically negligible.

These mass reductions lead to reduced space mission costs or increased launch payload capacity in the place of heavier photovoltaics. Given a launch cost of $2720 per kg of payload delivered to low earth orbit (LEO) on a Falcon 9 rocket, and based on the cost values calculated above, switching from silicon to 2D PV will reduce the costs of sending solar energy generation systems into space by $1,097 per kW of power generation

launched relative to silicon PV. For the more common commercial case of geosynchronous transfer orbit launches, the launch cost is $7470 per kg launched, corresponding to $2985 savings per kW launched if 2D-based PV are used in place of silicon. These values are even higher for interplanetary missions. Additional packaging gains may be made due to the flexible nature of 2D PV. As proposed spacecraft, satellites, space stations, lunar bases, and interplanetary outposts feature progressively larger solar arrays, such as those seen in proposed Sunflower spacecraft, this mass reduction will become even more critical.[39] A similar case can also be made for terrestrial vehicle-integrated PV (VIPV) such as solar-powered cars and aircraft. It is worth noting that the decrease in mass gained from using 2D PV is small relative to the mass of the vehicles in both of these cases, but 2D PV would still require less mass than any other known PV technology, and may enable such photovoltaic integration to accelerate.

We therefore believe that 2D TMDC-based photovoltaics have the potential to improve low-mass power generation without sacrificing efficiency; however, we also recognize that larger strides in 2D materials growth and processing capabilities are required first. With this perspective in mind, we focus our efforts on MoS_2 large-area growth with the expectation that abundantly available cm^2-scale MoS_2 will accelerate the development of 2D TMDC photovoltaics.

1.2 IR-TRANSMISSIVE PHOTOVOLTAICS

We now pivot away from 2D materials to discuss an altogether different strategy for photovoltaic energy production. Here we address a very specific loss mechanism: sub-

bandgap infrared radiation. By utilizing spectrum-splitting photovoltaics, we aim to capture low-energy infrared radiation in the form of heat, therefore utilizing a significant portion of the solar spectrum that cannot be converted by traditional photovoltaics. In order to understand this loss-mechanism, and how to mitigate it, we first review basic photovoltaic operation principles.

1.2.1 Full-Spectrum Utilization

A fundamental property of any semiconductor is its bandgap, E_g, defined as the energy difference between the highest energy point of the valence band and the lowest energy point of the conduction band. The bandgap energy is therefore the minimum energy required to raise an electron from the valence band to the conduction band. When irradiated by photons of energy greater than or equal to the bandgap, incident photons will impart their energy to valence band electrons and excite them into the conduction band. Photovoltaics operate by using an internal electric field to separate the excited electrons, resulting in an internal voltage that can be used to drive an external circuit. However, this photovoltaic process is only available to photons with energy greater than the bandgap, or $\lambda < \lambda(E_g)$. Lower energy photons either transmit through the photovoltaic material, or are absorbed by impurities or dopants within the semiconductor and converted to heat. In virtually all PV devices, IR light becomes a parasitic source of loss which further reduces the efficiency of the cell by raising the cell temperature. The solar spectrum incident on the earth at most latitudes, AM1.5G, is shown in Figure 1-2. As noted in the figure, approximately 81.2% of the incident solar spectrum power is composed of photons of higher energy than the silicon bandgap and can therefore be photovoltaically converted to electrical current. However, 18.8% of the spectral power is

below the bandgap, and therefore is unable to be converted to electricity by the silicon. This 18.8% is typically considered a loss, but some hybrid PV seek to collect this infrared energy using alternative thermal collection means. In this way, total system efficiency may be boosted by increasing the total spectral power conversion efficiency.
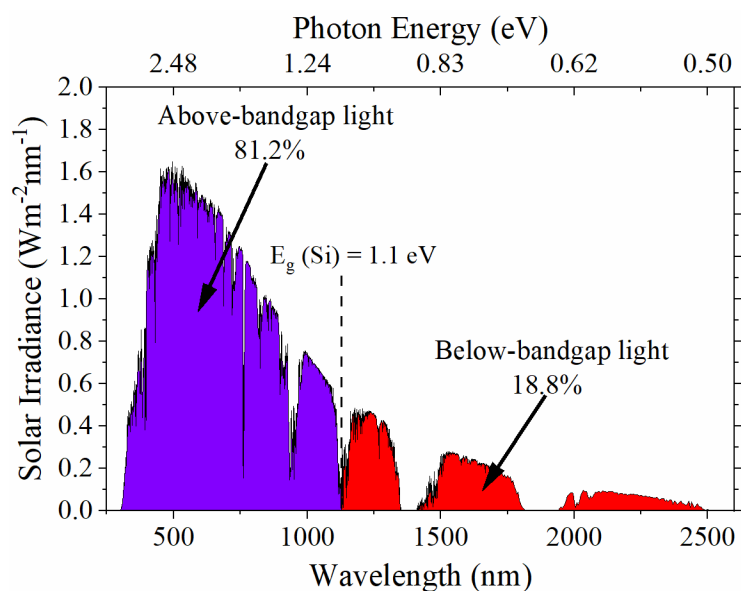
Figure 1-2 AM1.5G solar spectrum with Si bandgap highlighted

1.2.2 Transmissive Concentrator Photovoltaic Cells

While several strategies are in development to capture the otherwise-wasted sub-bandgap infrared radiation on solar cells, the most relevant one for this dissertation is of IR-transmissive photovoltaic cells. In 2016, Xu and coworkers developed transmissive III-V triple-junction solar cells designed to transmit light of energy less than the bandgap of the GaAs substrates, or $\lambda > 870$ nm. Of the "inband" light of wavelength $\lambda < 870$, the cells demonstrated a high conversion efficiency of 40.2% under 1 sun, and 47.6% under concentration. Of the "out-band" light, 76.5% is transmitted through the cells.[40] The cells contained several design points to improve their in-band efficiency and out-band

transmission, such as the incorporation of back-contact grid fingers and the utilization of a GaAs substrate rather than the more common Ge substrate. In this way, the cells are able to effectively "split" the solar spectrum by converting visible light to electricity while simultaneously transmitting infrared light, where it can be collected by a thermal receiver. In doing so, the power of the infrared wavelength photons can be collected and used, rather than wasted, bringing about the potential for full-spectrum efficiency surpassing that of even the highest efficiency photovoltaics. This combination can lead to collection of upwards of 75% of the solar spectrum as combined heat and power, far greater than the typical 20% - 30% associated with photovoltaics. A key future challenge will be implementing this technology in such a way that is economically viable and physically durable, as is discussed later in this thesis.

1.3   THESIS OVERVIEW

Having introduced the major relevant concepts of 2D material physics, application, and growth, and also full-spectrum solar energy collection, we now proceed to provide an overview of the content of this thesis. The content can be broken down into three main sections. The first section is contained in chapter 2 and chapter 3 and seeks to address the need for large-scale and high-quality MoS_2. We first use chapter 2 to detail the development of a new MoS_2 growth technique called thermal vapor sulfurization (TVS) as a way to achieve wafer-scale MoS_2 with layer-by-layer control of the MoS_2 thickness.[41] The specific innovations brought about by this TVS technique are explained, such as using powder MoS_2 as a highly-controllable sulfur vapor source. We demonstrate TVS as a reliable growth technique, and detail the quality of the resultant MoS_2 growth in comparison to peer growth techniques.

Chapter 3 recognizes that a primary limitation of existing MoS_2 growth techniques, including TVS, is the long MoS_2 growth process time on the order of hours. The chapter then goes on to introduce a new MoS_2 growth technique using rapid thermal processing (RTP), which grows MoS_2 within 15 minutes, an order of magnitude faster than the next closest alternative. In this way, we show that MoS_2 on the scale of hundreds of cm^2 can be synthesized within minutes, with the possibility of dozens of iterations per day. The quality of the grown MoS_2 is shown to be comparable to alternative techniques, while possessing an undisputed advantage in throughput.

The next major section of this thesis focuses on the development of optoelectronic devices from grown MoS_2 and is concentrated in chapter 4. Since the end-goal of MoS_2 synthesis is not merely to produce MoS_2, but to use it as a foundation for MoS_2-based optoelectronic devices, we limit our discussion to devices fabricated on synthetically grown large-area MoS_2. We will present devices made on MoS_2 grown via both TVS and RTP. The primary device discussed will be the phototransistor, and external quantum efficiency (EQE) and responsivity measurements are used to quantitatively indicate fundamental device performance in converting incident photons to conduction electrons. Spectral EQE is introduced as a powerful tool to show spectral detector performance and to identify spectral features such as the excitonic A and B peaks. We also outline steps necessary to progress from lateral photodetectors to vertical photovoltaics, and provide a roadmap to obtain the first ever demonstrated large-area 2D TMDC-based solar cell.

For the third major section of this thesis, we transition away from 2D materials toward full-spectrum solar energy conversion using transmissive solar cells in chapter 5. This effort focuses on the development of a transmissive photovoltaic module that houses an

array of IR-transmissive PV cells. The module is designed for concentration of up to 500 suns, which enables the transmitted IR light to be collected at valuable high temperatures, but also necessitates active cooling of the PV cells to maintain reasonable cell temperatures. The performance of the cells and the transparent active cooling system is detailed, and the results from multiple weeks of outdoor testing are presented. Ultimately, full-spectrum utilization is achieved, and parallel electrical and thermal output streams are produced. A roadmap to develop larger and higher quality systems is also introduced, with insights for continued development toward commercially competitive systems.

We end this thesis with a summary and conclusions section, and also with an outlook for each of the technologies presented herein. This final section will suggest future directions and surmise possible short-term and long-term results for the 2D photovoltaics and transmissive photovoltaics. Several appendices are located at the end of the text to provide additional experimental details for interested readers.

2 WAFER-SCALE SYNTHESIS OF MONOLAYER AND FEW-LAYER MOS2 VIA THERMAL VAPOR SULFURIZATION

This chapter details the development of a MoS_2 growth technique known as thermal vapor sulfurization (TVS). In particular, we detail novel developments to the TVS method, and analyze the resultant growth with a suite of electrical and materials science analysis tools.

As described earlier, MoO_3-based CVD is currently the most commonly utilized 2D MoS_2 synthetic growth technique. However, an alternative technique called thermal vapor sulfurization (TVS) presents unique advantages. Rather than solid powder MoO_3, TVS uses pre-deposited Mo or MoO_3 films as the Mo source, and flows hot sulfur gas over the films to synthesize MoS_2. TVS 2D MoS_2 growth was first demonstrated by Zhan et al. in 2012[42] and further developed by several following reports[43–46]. These reports demonstrate MoS_2 growth consistently down to three-layer thickness. Additionally, TVS is uniquely able to incorporate doping, patterning, and hybridization into its process by pre-modifying the solid molybdenum precursor[47,48]. However, because monolayer and few-layer TMDC growth with TVS has proved challenging, TVS is most often used to produce thicker (>5nm) MoS_2 films with high electron mobility and wafer-scale film coverage[49]. Few-layer MoS_2, even down to monolayer, has been observed from trials done using annealed MgO substrates or with the use of dangerous H_2S gas as a sulfur source [43,45]; however, these conditions limit the practicality of monolayer TVS growth. Patchy monolayer and few-layer MoS_2 growths have been

achieved using MoO_3 as a precursor, with further work needed to validate this method.[50] Furthermore, confirmation of layer-by-layer control in the monolayer and few layer regime is still needed in order to further validate 2D TVS MoS_2 growth. Accomplishing high quality single and few-layer TVS growth would allow the benefits of TVS synthesis to be combined with the high optical quality of few-layer MoS_2 for large-scale optoelectronic applications.

In this chapter, a modified TVS technique is developed that uses powder MoS_2 as the sulfur source, rather than solid sulfur powder or gaseous H_2S. The use of MoS_2 powder reduces the sulfur vapor flux in the reaction chamber, leading to slower, more stable growth. This modification proves critical to enabling monolayer MoS_2 via TVS, which in turn opens up TVS-grown MoS_2 for optoelectronic applications. Within this chapter we first analyze the films in terms of structure and morphology to confirm the presence and quality of MoS_2, and then transition to applications-based testing of optical and electrical qualities.

2.1 RESULTS & DISCUSSION

In this section we present the results of our TVS growth and compare it to those of alternative techniques.

2.1.1 TVS Growth

Unlike previous efforts, the TVS technique described below is modified to enable synthesis of monolayer and few-layer MoS_2 films. The growth technique is summarized and visualized in Figure 2-1A, in which sulfur vapor is reacted with thin molybdenum metal films inside a dual-chamber vacuum tube furnace to yield cm-scale MoS_2 films.

The resultant MoS_2 is macroscopically uniform over more than 2 centimeters, as shown in Figure 2-1B. Prior to the TVS process, precursor molybdenum films are deposited via electron beam evaporation onto SiO_2 and sapphire substrates; Figure 2-1C shows a precursor film step edge before the TVS reaction. The deposited molybdenum film thickness ranged from 0.1nm to 2.6nm, a range that includes monolayer, few-layer, and quasi-bulk MoS_2 thicknesses. Sulfur vapor is produced by heating up powder precursor MoS_2; when heated to 900°C, MoS_2 powder slowly outgasses sulfur, providing a steady stream of sulfur vapor with relatively low vapor pressure[49,51,52]. This slow flux and partial pressure of sulfur aides in the growth of monolayer MoS_2 without saturating the chamber and reaction with excess sulfur. The sulfur vapor is transported by argon carrier gas to react with the Mo-coated substrates in a downstream 830 °C region of the tube furnace. The low flow of sulfur from heated MoS_2 precursor promoted lateral MoS_2 growth on the substrate and limited vertical growth, resulting in an optimization of the optical and electronic properties of the grown MoS_2.

On the wafers, MoS_2 growth only occurs in regions previously covered with precursor Mo, as shown in Figure 2-1C and Figure 2-1D, with a crystal graphic above these figures representing the deposited Mo and the MoS_2 2H crystal structure.[15] The conversion to MoS_2 is evidenced by increased contrast between the film and the substrate, and a ~60% increase in thickness of the film as measured by AFM (inset). Based on this result, we infer that the primary MoS_2 growth mechanism is the reaction of sulfur vapor with the molybdenum the precursor film, and that physical evaporation of MoS_2 molecules from the powder source boat did not result in any significant deposition of molecular MoS_2 onto the substrates. In other words, the molybdenum precursor films are converted to

MoS$_2$, and substrate regions without molybdenum precursor remain bare after the TVS reaction. Subsequently, precursor films can be arbitrarily patterned via photolithography and run through the TVS process to produce a correspondingly patterned MoS$_2$.[48] This capability is unique to TVS and provides a route for MoS$_2$ patterning without defect-inducing post-growth photoresist patterning or etching of MoS$_2$ films[53], and future trials can leverage this capability to produce advanced MoS$_2$ patterns for applications such as integrated photonic sensors.
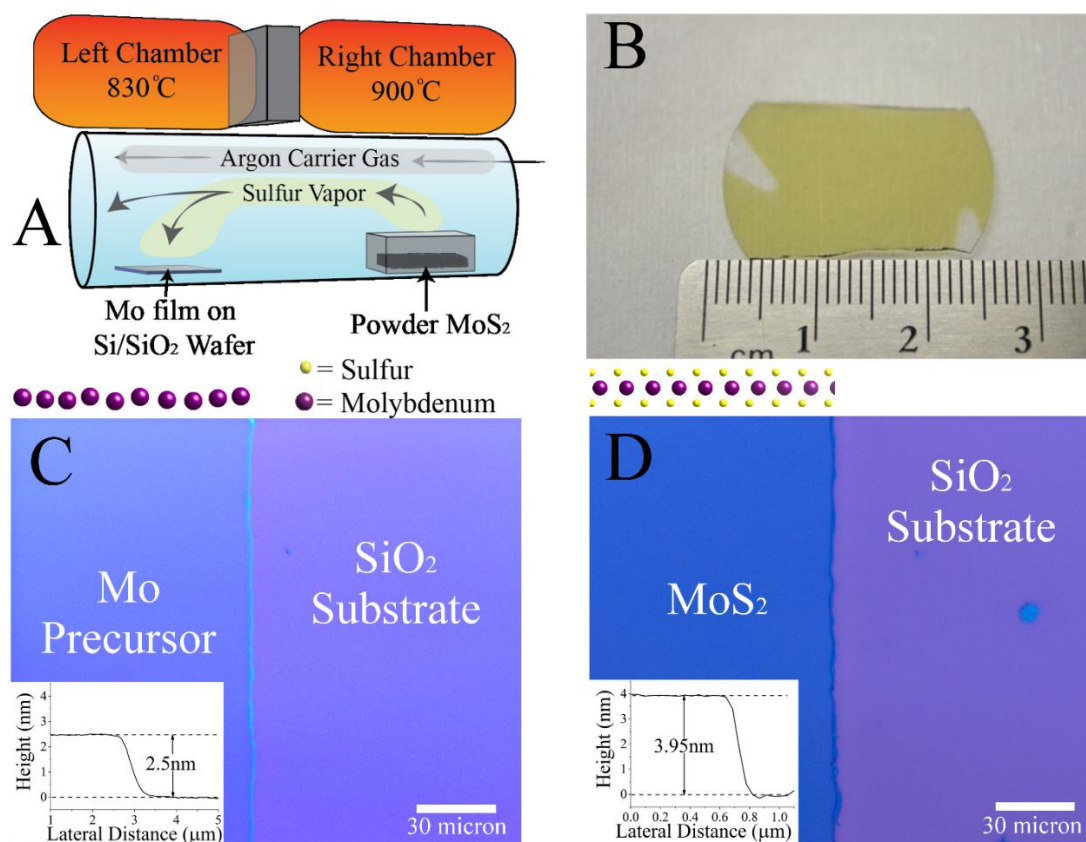
Figure 2-1 (a) TVS reaction schematic. (b) Photograph of wafer-scale MoS$_2$ growth on a sapphire wafer (cm-scale ruler for reference) (c) A Si/SiO$_2$ wafer showing a region of Mo precursor metal and a region of bare SiO$_2$ substrate. AFM profile shows height of example precursor Mo (inset). (d) MoS$_2$ growth after TVS process. Inset shows AFM profile of resultant MoS$_2$ film.

2.1.2 Thickness Control

As emphasized previously, the ability to control thickness is critical for 2D growth, especially for obtaining monolayer MoS_2. Atomic force microscopy (AFM) is a direct way of measuring height profiles with sub-angstrom resolution, and is therefore employed to evaluate the thickness and thickness control of the grown MoS_2. Figure 2-2a plots MoS_2 film thickness measured via AFM versus precursor molybdenum thickness. A linear regression (dashed line) with slope 1.735 is fit to the data, revealing a growth ratio of 0.65 nm MoS_2 (monolayer thickness) per approximately 0.37 nm molybdenum precursor. The linear trend implies very little residual Mo precursor remains after the TVS process within the range of 0-1.6 nm precursor. Additionally, a y-intercept of 0.163 nm (and x-intercept of -0.1nm) is present on the fitted line, a systematic error resulting from slightly inflated AFM step edge thickness measurements due to kinks in the MoS_2 basal plane and steps near the edges of scratches where thickness measurements are made. The linear regression relationship derived from this plot is used to mark the MoS_2 thickness displayed in the top x-axis in the subsequent plots in this chapter, allowing characterizations to be displayed as a function of both precursor Mo thickness and the resultant MoS_2 thickness.
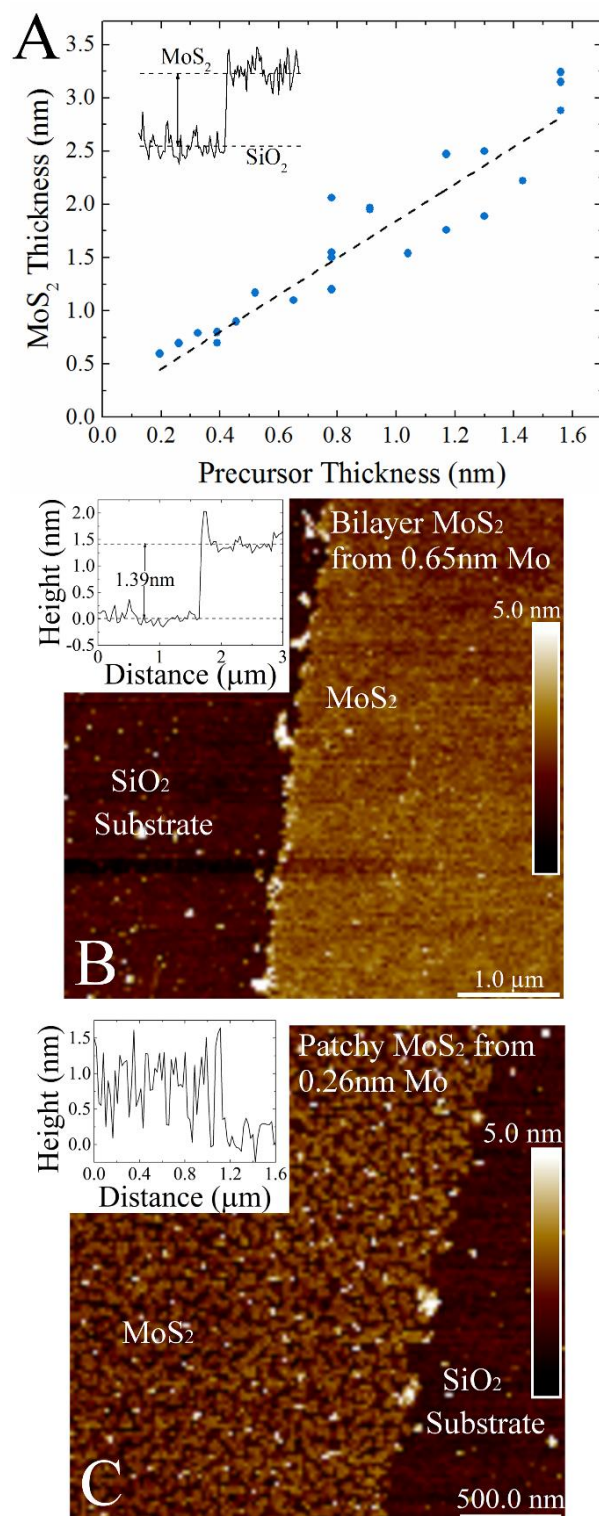
Figure 2-2 (a) AFM measured step heights of MoS₂ films measured at scratch locations (example in inset). (b) MoS₂ film from 0.65 nm Mo Precursor, roughness of 0.20 nm. (c) Discontinuous MoS₂ grown from 0.26 nm Mo precursor, with roughness 0.67 nm.

Individual AFM surface micrographs, shown in Figure 2-2b and Figure 2-2c, reveal the morphology and topography of the MoS_2 films. For example, Figure 2-2b reveals a smooth, complete bilayer sample (from 0.65 nm precursor) with roughness of 0.30 nm. This roughness is mostly caused by the surface roughness of the Si/SiO_2 substrate, which is also measured to be 0.30 nm. In contrast, Figure 2-2c shows a sample from 0.26 nm precursor Mo expressing sub-monolayer average thickness of 0.60 nm, but expressing isolated growth clusters and average roughness of 0.6 nm. The individual clusters show regions of primarily monolayer (0.65nm) with some bilayer (1.3nm) thickness, indicating that some bilayers will grow when mass aggregation occurs due to insufficient Mo coverage; this is likely driven from the extra free energy at exposed MoS_2 edge sites. Therefore, if less Mo precursor is deposited than is required to form a complete monolayer, an incomplete layer is formed composed of monolayer MoS_2 with exposed regions of substrate due to insufficient MoS_2 coverage and with some bilayer regions forming within the monolayer MoS_2 clusters. However, when sufficient precursor Mo is provided, as shown in Figure 2-3, smooth and homogeneous growth occurs. Monolayer, bilayer, trilayer, and 4-layer MoS_2 are confirmed in Figure 2-3 via step height measurements, with thickness controlled by precursor Mo thickness. Complete layers require molybdenum in increments of approximately 0.37nm, and intermediate values yield MoS_2 with average thicknesses intermediate between the incremental layer MoS_2 heights of 0.65nm. This highlights the high controllability of MoS_2 layer thickness produced by TVS. This also is responsible for the variation in thickness measured in some samples on Figure 2-2a; for example, the data point at 0.78nm precursor thickness was measured to have MoS_2 thickness between 1.2nm and 2.06nm when measured at

different points. This precursor thickness resides at an intermediate point to yield

between bilayer and trilayer, and therefore contains regions with bilayer and regions with

trilayer; the average thickness of the MoS_2 from the 0.78nm precursor sample, across all

regions is 1.58nm, showing it to be an intermediate between 2 and 3 layers. Precursor

film thickness may be optimized for specific applications; for example, even sub-

monolayer growths may be useful for applications that benefit from exposed MoS_2 edges,

such as hydrogen evolution reactions[53].
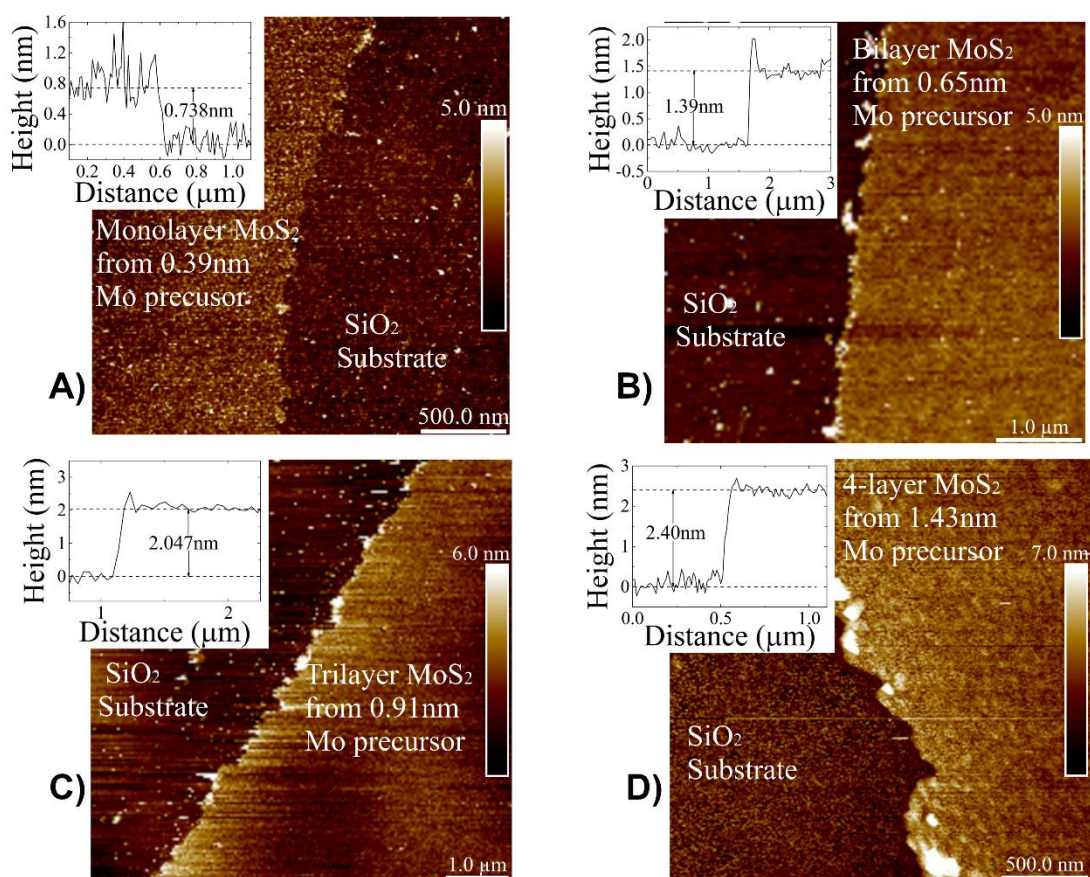
Figure 2-3 AFM surface micrographs of a) monolayer b) bilayer c) trilayer, and d) 4-layer MoS_2 indicating surface smoothness and uniformity.

2.1.3 Transmission Electron Microscopy

Transmission electron microscopy (TEM) is another powerful tool that can be used to image crystalline structures at the atomic level. Figure 2-4a shows a TEM image of monolayer MoS_2 grown from 0.39nm molybdenum precursor and reveals a hexagonal crystal lattice with lattice parameter a=0.310nm, which compares well to literature values of a=0.315 for the common 2H semiconducting phase of MoS_2. [15] FFT analysis (Figure 2-4a inset) reveals two hexagonal lattice domains. Similarly, a TEM image of bilayer MoS_2 is shown in Figure 2-4b, revealing a lattice constant of a=0.319nm.

The bilayer sample of Figure 2-4b also shows distinct features called Moiré patterns, which indicate that the two layers are not stacked in the exact same orientation. The Moiré patterns can be analyzed by assuming two identical hexagonal patterns rotated by an angle α relative to each other, which results in periodic fringes spaced a fixed distance apart. The spacing between each blurry fringe, D, is related to α by $D = \frac{p}{2}/\sin(\frac{\alpha}{2})$, where $p = 0.315$nm is the lattice parameter of MoS_2. This analysis reveals that the adjacent crystal faces are by α=5.2° relative to each other. FFT analysis (Figure 2-4b inset) also confirms two domains rotated ~5° relative to each other. We note that these two rotated domains are continuous laterally, and show larger grain size than the domains shown for monolayer samples (Figure 2-4a). Interestingly, the relative rotation value is similar to those found by Jeon et al.[54] for CVD-grown MoS_2, which may indicate an energetic preference of MoS_2 layers to grow at ~5° angles to each other for certain growth conditions. Future work on this phenomenon could help elucidate more of the MoS_2 growth mechanism.
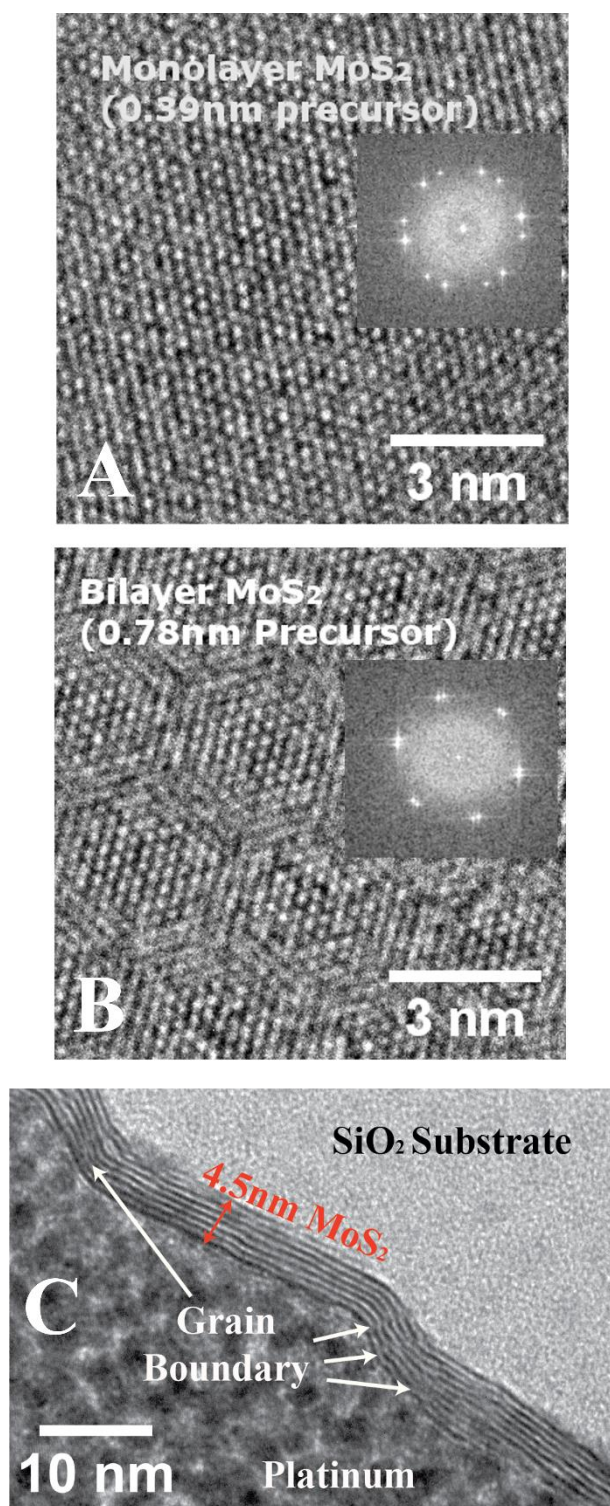
Figure 2-4 High resolution TEM images of (a) monolayer and (b) bilayer MoS$_2$ grown by TVS. (c) Cross-sectional TEM of 7-layer MoS$_2$, showing clear 2D layered ordering and grain boundaries concentrated at rough regions of the underlying substrate.

Figure 2-4c shows a cross-sectional TEM image of MoS_2 synthesized from 2.6 nm precursor molybdenum, a relatively thick sample. A platinum top layer is added post-TVS growth to provide structural support while acquiring the cross-sectional TEM samples. According to our thickness relationship measured with AFM earlier shown in Figure 2-2a, 2.6 nm is expected to yield 7.02 monolayers MoS_2; indeed, 7 layers (each dark streak is an individual layer) can be seen in Figure 2-4c, supporting the measured growth ratio of one monolayer per 0.37nm precursor Mo. Some regions of the cross-sectional TEM can be seen to possess 8 or 6 layers, showing some inhomogeneity in thickness likely due to the particularly thick starting Mo and the SiO_2 substrate surface roughness. The total thickness of 7 layers is measured to be 4.5 nm, corresponding to 0.642 nm per layer, nearly matching the literature value of 0.65nm per MoS_2 monolayer[18]. Additionally, the individual layers stack neatly and coherently throughout the thickness with only a few instances of layers inter-crossing each other. These properties are partially the result of the "top-down" nature of the reaction in which first the top layer of MoS_2 is formed, followed by deeper layers as the sulfur diffuses through the molybdenum. The "top" layer bordering the protective platinum layer is high-quality and continuous, due to it being the first layer formed. The tendency to form distinct lateral layers is a clear illustration of the two-dimensional nature of MoS_2.

Crystal domain edges can be seen in Figure 2-4c as blurry regions that intersect vertically through the cross-section. These edges reveal domains ranging from 5 to 20nm wide. This domain range is consistent with the domain sizes of top-view TEM, highlighted in Figure 2-5. This domain size range is relatively small compared to literature value MoO_3-precursor CVD techniques, which can reach sizes of up to 350 µm per domain for

some growth configurations[33]. The grown MoS_2 conforms well to surface substrate contours, bending around uneven surfaces and generally retaining the same thickness. This substrate conformity is also partially due to the top-down nature of the TVS MoS_2 growth that assumes the contours of the pre-deposited MoS_2 film, which accordingly is contoured to the substrate surface. This capability allows TVS MoS_2 to be grown on a wide variety of substrates. However, rough substrate regions also lead to a higher density of discontinuous "kinked" domains and grain boundaries in the grown film, which reduces the average domain size and electronic quality of the growth technique; in future experiments, use of atomically smooth substrates is expected to significantly increase domain size by reducing contour-induced discontinuities.
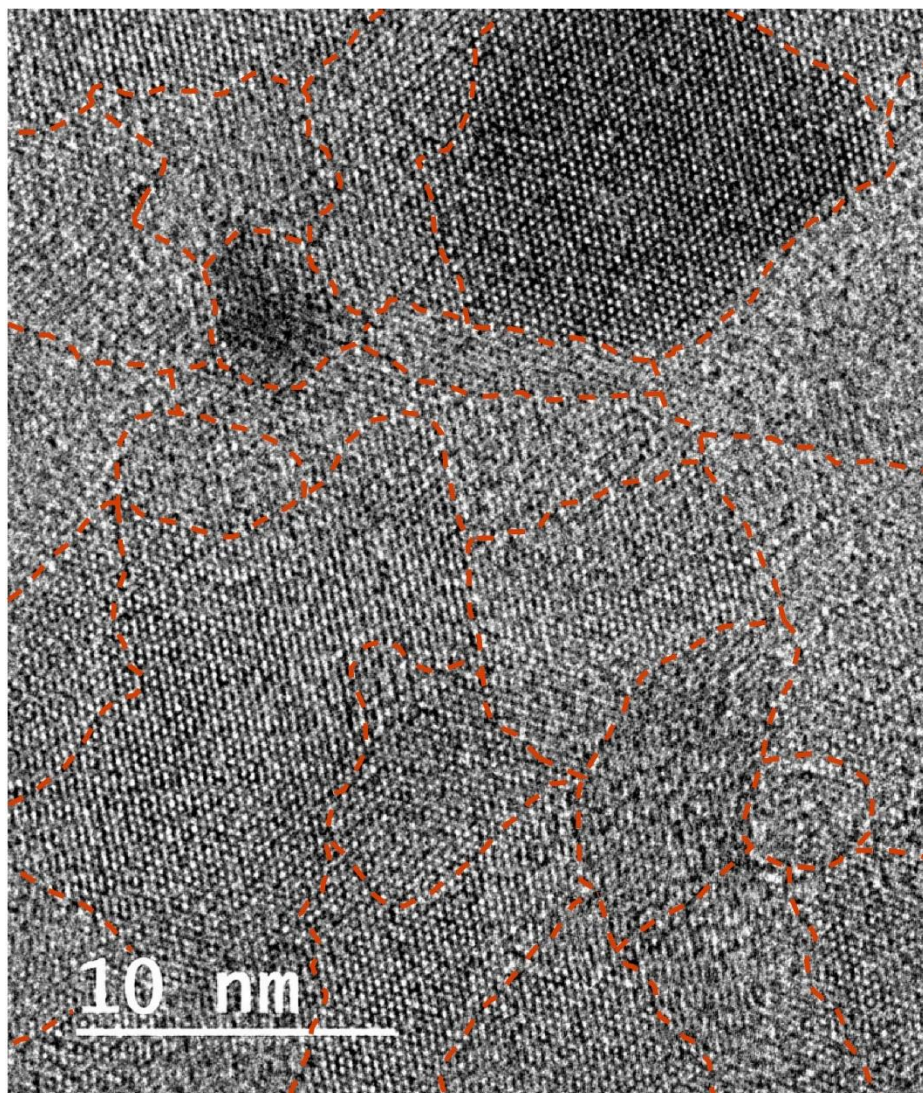
Figure 2-5 HRTEM image of a mostly monolayer MoS$_2$ sample grown from 0.39 nm molybdenum precursor. Red dashed lines follow along the visible domain boundaries, revealing domains 5-20nm wide.

2.1.4 Raman Spectroscopic Analysis of MoS$_2$

Raman spectroscopy is a powerful and non-destructive tool for analyzing the structure of crystalline materials by probing inelastic light scattering and phonon mode interaction. Additionally, Raman spectra are particularly valuable for 2D TMDC's due to the ability to calculate the thickness of a 2D film based on the spacing between the two prominent

A_{1g} and $E_{2g}{}^1$ Raman peaks.[55] Figure 2-6a shows raman scans of MoS_2 grown from 0.325nm Mo precursor on Si/SiO_2 substrate, with corresponding sampling spots marked in Figure 2-6b; the uniformity of the shape of the peaks, along with their common peak spacing of $\Delta = A_{1g} - E_{2g}^1 = 20cm^{-1}$, indicates uniform monolayer coverage across the sampled area, further confirming the thickness expected from AFM and indicating cm-scale uniformity.[55] A bilayer sample is also analyzed, as shown in Figure 2-6c and Figure 2-6d, resulting from 0.585nm thick Mo precursor; in this case, Raman peak spacing of $\Delta=22cm^{-1}$ indicates a bilayer sample, with very little variation in the Raman peak shapes.[55] According to the linear relation of Figure 2-2a, a sample with 0.585nm Mo precursor corresponds to MoS_2 1.18nm thick, or approximately bilayer. This Raman measurement critically shows uniform monolayer and bilayer MoS_2 on the centimeter scale, a key design requirement for the development of this growth scheme.
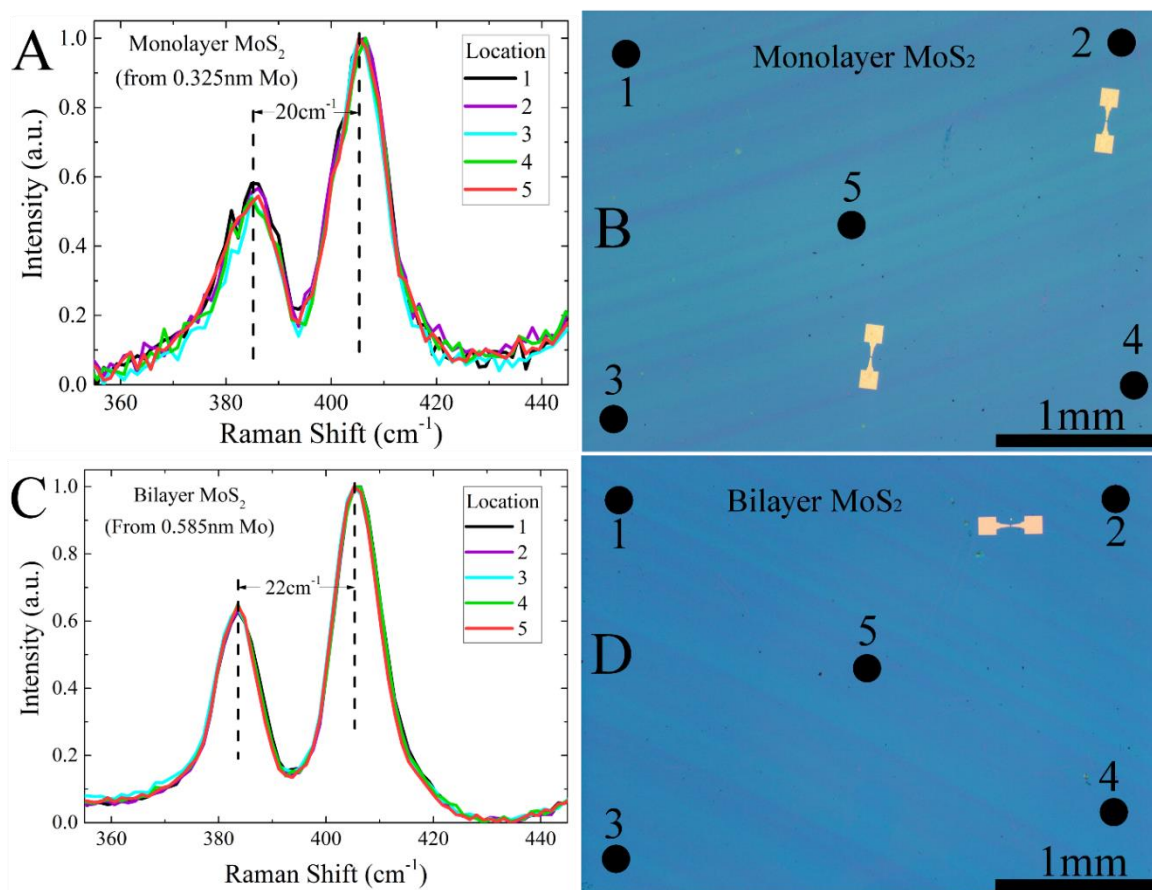
Figure 2-6 (a) Raman spectra from five different sampling spots on a MoS₂ sample grown from 0.325nm precursor Mo, with Δ=20cm⁻¹ indicating monolayer thickness; image of sample shown in (b), with transistors visible as gold features. (c) Raman spectra from five sampling spots on a MoS₂ sample grown from 0.585nm precursor Mo, with Δ=22cm⁻¹ indicating bilayer MoS₂; image of sample shown in (d), indicating different sampling locations.

Raman scans from several different MoS₂ thicknesses are shown in Figure 2-7a, with the Mo precursor thickness on the bottom x-axis. The top x-axis displays the MoS₂ thickness as interpolated from the linear regression of Figure 2-2. The peak spacing between the A_{1g} and E_{2g}^1 are displayed on the left y-axis, showing the correlation of the MoS₂ thickness measurements of AFM with Raman-calculated thickness. The colored

horizontal bars indicate the expected number of layers based on each Δ value and demonstrate the complete range of MoS$_2$ thicknesses from monolayer to 5+ layers (bulk properties). We show that MoS$_2$ is obtained in incremental thicknesses from monolayer to bulk as the precursor Mo thickness is precisely changed. Some samples contained Δ values indicating 4-layer MoS$_2$, but were measured by AFM to be 3-layer, likely the result of an inhomogeneous fourth layer on top of a continuous third. As the thickness transitions from 3 to 4 layers, regions of 4-layer MoS$_2$ dominate the Raman signal; this phenomenon is expected for MoS$_2$ growths derived from intermediate precursor Mo thicknesses, as explored in Figure 2-2c.
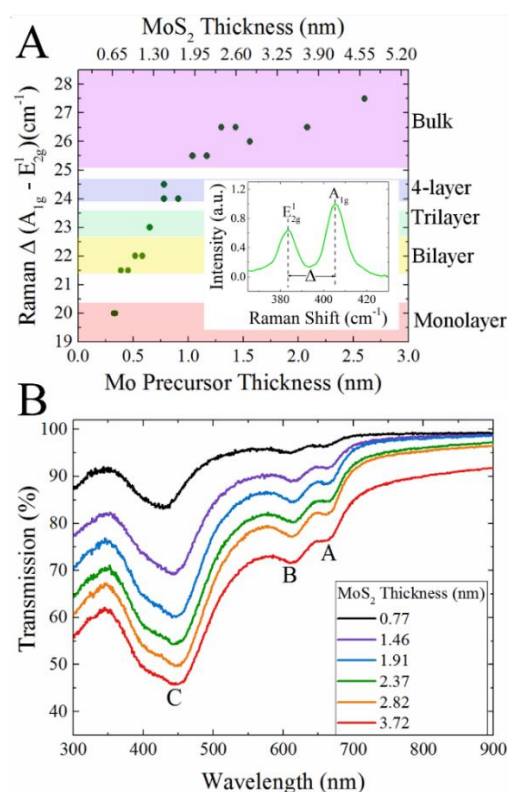
Figure 2-7 (a) Shows Raman Δ values (Inset: Bilayer MoS₂ example) as a function of precursor thickness. Horizontal colored bars represent expected thickness from raman Δ value. (b) Transmission measurements of MoS₂ films grown from different precursor thicknesses, revealing A(660nm), B(620nm) and C(430nm) exciton absorption peaks.

2.1.5 Transmission Spectroscopy of Grown MoS$_2$

Thus far, we have confirmed the material grown via our TVS technique is 2H MoS$_2$ based on Raman scans and by directly imaging the crystal lattice via TEM. We also confirmed via AFM that the material thickness matched the expected values for monolayer, bilayer, and trilayer samples, and cross-confirmed with Raman spectroscopy. These structural and morphological properties are critical for material identification, but we now transition to optical and electrical analysis of the grown films, which directly inform their potential to be made into devices for practical applications. First, transmission spectra of several samples are shown in Figure 2-7b, revealing a glimpse of the band structure of the grown materials. Each sample shows a clear band edge at ~670nm, matching well with the expected 1.85 eV direct bandgap of MoS$_2$.

Transmission of > 98% is seen above the bandgap energy in few-layer samples (trilayer and lower), while thicker samples absorb in that region due to the 1.3 eV indirect bandgap. The A (660nm), B (620nm) and C(430nm) absorption peaks are typical of the MoS$_2$ A, B, and C excitons and are commonly seen in MoS$_2$ transmission and absorption spectra.[56] It is noteworthy that the total integrated transmission decreases linearly with thickness, as shown in Figure 2-8 (left) for integration in the 400-700 nm range. This is to be expected, assuming no significant loss of material occurs during the TVS process. These measurements suggest stacked MoS$_2$ capable of forming various incremental thicknesses, as also supported by cross-sectional TEM and AFM. Furthermore, reflection, absorption, and transmission for grown monolayer MoS$_2$ is shown in Figure 2-8 (right). An average sub-bandgap absorption of 8.06% (400-700nm,) is measured per 0.65 nm monolayer; this value yields an absorption coefficient of 1.24 x 10^6 cm^{-1}. For

comparison, this absorption coefficient is one order of magnitude larger than that of silicon and GaAs in the visible spectrum, allowing MoS_2 to absorb light using much thinner materials.[57] The high monolayer absorption coefficient is a major motivation further research of MoS_2 as an ultra-energy dense photovoltaic material for energy conversion applications[23,37,58].
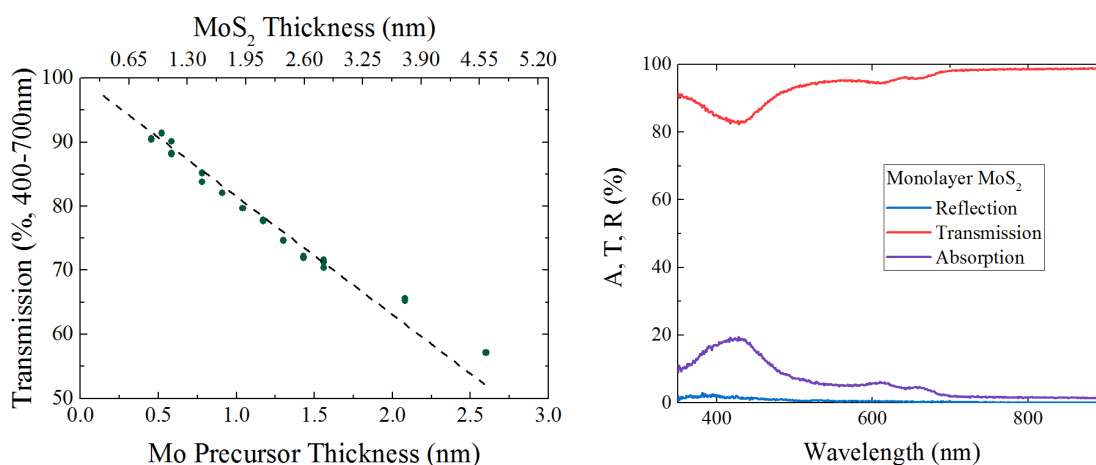
Figure 2-8 Integrated transmission (400nm – 700nm) as a function of Mo precursor thickness and MoS₂ thickness, showing a linear correlation (left) absorption, transmission, and reflection of monolayer MoS₂ (right)

2.1.6   Photoluminescence Analysis

A key property of a material with a direct bandgap is the increased ability for its excitons to radiatively decay back to the valence band. All semiconductors can, in principle, experience radiative recombination, but direct bandgap semiconductors experience this recombination at a much higher rate because no change in exciton momentum is required to excite and decay the exciton. Radiative recombination can be measured via photoluminescence (PL) spectroscopy, which directly measures luminescent output light from a material. Figure 2-9a shows the PL spectra of monolayer (blue), bilayer (red), and trilayer (black), with the characteristic A exciton visible in each spectrum at 660-670nm.

The smaller B exciton, blue-shifted from spin-orbit coupling,[59] is more easily seen as a shoulder on the A peak when plotted in logarithmic scale in Figure 2-9a's inset. The monolayer PL is seen to be two orders of magnitude larger than the trilayer sample, as seen in the integrated PL (integrated from 500 to 800nm) in Figure 2-9b. This sharp increase confirms the indirect-to-direct bandgap transition as MoS_2 is thinned from bulk to monolayer. Because bilayer and trilayer MoS_2 are indirect bandgap semiconductors, their photoluminescence is considerably smaller than monolayer, but non-zero.[19] The integrated PL intensity in Figure 2-9b is plotted as a function of precursor thickness, showing tuning of the direct to indirect bandgap transition by varying only the precursor thickness, which in-turn varies the MoS_2 thickness. The chart shows three distinct regions; a region of high, monolayer-like photoluminescence at precursor thicknesses 0.33nm precursor and lower, a 2 order of magnitude smaller photoluminescence region for samples from precursor thicker than 0.75nm, and an intermediate transition region composed of bilayer and trilayer regions. It should be noted that the largest photoluminescence value is found at the MoS_2 sample measuring 0.65nm thick, matching the expected thickness of monolayer MoS_2. Similar to Figure 2-2a, it can be seen that some samples, such as the 0.78 nm precursor sample, have a large variability that can be explained by its composition of being intermediate between two discrete thicknesses. In the case of the 0.78 nm Mo sample, it is between bilayer and trilayer thickness, and therefore has a large photoluminescence amplitude variability. Growths below 0.65 nm average thickness are composed of patchy island growths, such as the one imaged in Figure 2-2C; these sub-monolayer growths display progressively smaller photoluminescence peaks as the amount of precursor Mo is decreased down to zero due

to diminishing surface coverage of MoS_2. Although these growths were shown in Figure 2-2C to contain some bilayer regions, they also are shown via photoluminescence to contain significant monolayer character. These photoluminescence results further confirm the presence of monolayer MoS_2 in the TVS growths and establish the value of MoS_2-based sulfur precursor for producing monolayer MoS_2.

The photoluminescence external quantum yield (%QY) represents the ratio of luminescent photons to incident photons, an important performance metric in optoelectronic devices. %QY is calculated using the relationship:

$$\%QY = \frac{photons\ out}{photons\ in} *100\% = \frac{A\Theta I_{out}}{hf_2}\frac{hf_1}{P_{in}}$$

Where I_{out} is luminescent light irradiance measured by a fiber-coupled spectrometer at an average frequency f_2=c/660 nm, A=0.0028 cm^2 is the area of the spectrometer fiber aperture, $P_{in} =$ 1.5 mW is the pump power of the 405 nm excitation beam at frequency f_1 =c/405nm, and Θ is the measurement tooling factor. Further details on the calculation of luminescence %QY can be found in 1.1.1Appendix C.

The incident spot size used in the PL measurements is of area ~1256 µm^2, resulting in a pump probe irradiance of ~1.2e-6 µW/µm^2. The pump probe irradiance has been shown to strongly effect the total %QY of MoS_2, and therefore must be considered when comparing results across different setups.[22] %QY values are shown in the 2nd y-axis of Figure 2-9b, illustrating the improvement in optical quality of the samples as they are reduced to monolayer thickness. Furthermore, to accurately compare the optical quality of these grown samples to standard exfoliated MoS_2, photoluminescence internal quantum yield (%IQY) was calculated according to the relationship

$$\%IQY = \frac{\%QY}{a(405nm)}$$

The largest %IQY value for the samples was 3.16 x 10^{-4}% (0.33nm precursor), indicating that our MoS_2 grown by TVS has a similar %IQY, and therefore optical quality, as untreated exfoliated monolayer MoS_2 samples[22,60]. These optical properties are not significantly affected by grain size, helping explain how TVS can have competitive optical properties with exfoliated MoS_2 despite relatively small grain size. The %IQY value drops two orders of magnitude to 2.07 x 10^{-6}% for a 3-layer sample (0.91 nm precursor), expected due to the indirect-bandgap transition as the thickness increases past monolayer MoS_2. These results demonstrate that TVS grown monolayer MoS_2 can be synthesized cm-scale and with high optical quality similar to exfoliated crystals[19,22,60,61], a key result not previously reported from previous TVS growth that critically enables large-scale optoelectronic device production.
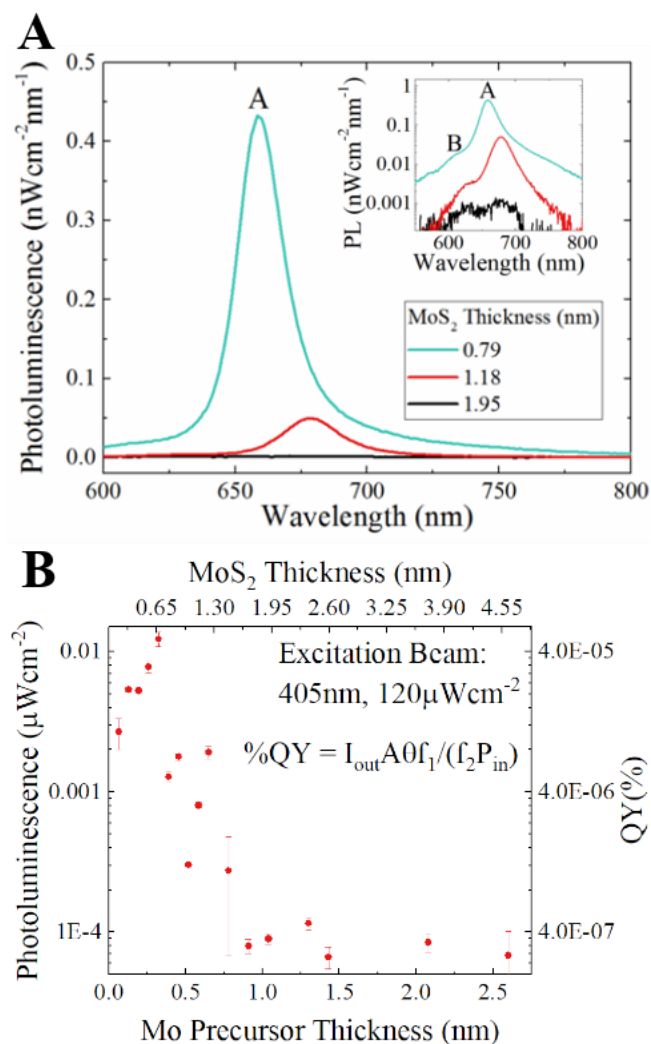
Figure 2-9 (a) Photoluminescence spectra of monolayer (blue), bilayer (red), and trilayer (black) TVS grown MoS₂ samples. Inset shows same PL curves with a log scale (b) Integrated PL plotted vs. precursor Mo thickness, with quantum yield on 2nd y-axis.

2.1.7   Electrical Analysis

One of the bottom-line metrics for 2D material device performance is field effect carrier mobility, which quantifies the response of carriers to an external electric field. In order to measure this property, field effect transistors (FETs) were fabricated to evaluate the electronic properties of the as-grown MoS₂ films.   As shown in Figure 2-10a inset, back-gated two-probe transistors with channel length of L=6μm and width of W=9 μm

were fabricated onto the MoS_2 samples. Deposited 50 nm gold contacts with an adhesion layer of 5nm Ti were used as the electrodes and via electron beam lithography. A back-gate electrode is accessed by scratching through the SiO_2 layer and is used to apply a gate voltage from -80V to 80V to the devices. Also, the threshold voltage V_{th} is calculated based on the x-intercept of the dashed lines in Figure 2-10b to be V_{th}=36.5 V.

Figure 2-10a shows an example series of I_{ds}/V_{ds} sweeps at four different gate voltages, V_g = 0, 20, 40, 80 V, measured on a bilayer TVS-grown MoS_2 device. The linear I_{ds}/V_{ds} behavior indicates ohmic contact between the MoS_2 film and Ti/Au contacts. Gate sweeps of the same device sample are shown in Figure 2-10b, where V_g was swept from 80V to 80V under V_{ds} = 2, 4, and 6 V. With positive gate voltages, the devices can be turned on with a current as high as 100 nA at V_g = 80 V; this indicates n-type MoS_2, a trait seen in all of our standard trials and also seen in both exfoliated and CVD grown MoS_2, likely due to sulfur vacancies.[47] The I_{on}/I_{off} ratio of this device can reach 10^4, which is an acceptable value for chemically synthesized 2D MoS_2. The dashed lines in Figure 2-10b represent the linear "on" section of the gate sweeps, and can be extrapolated to the x-axis to reveal a threshold voltage V_{th} = 36.5 V, consistent for each bias voltage. The calculated carrier density is therefore n_{2D}=3.13X10^{12} cm^{-2} when V_g=80 V for this device. Additional details of these calculations can be found in Appendix E .
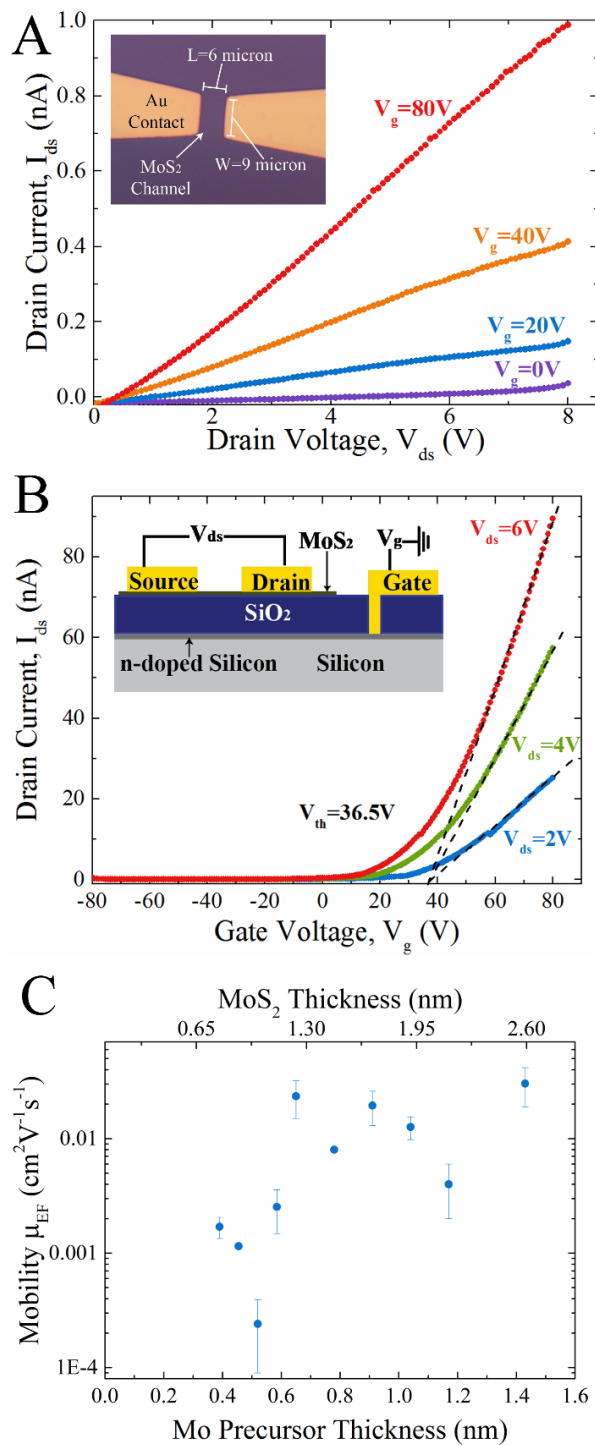
Figure 2-10 (a) I_{ds}/V_{ds} sweeps of a transistor formed from MoS$_2$ bilayer grown from 0.46nm Mo precursor. Inset image shows a top-down view of the MoS$_2$ transistor channel. (b) Gate sweeps of a transistor formed from MoS$_2$. Inset shows a diagram of the device structure. (c) Carrier mobility as a function of precursor thickness.

Each sample's carrier mobility, $\mu_{EF,}$ is plotted logarithmically in Figure 2-10c as a function of molybdenum precursor thickness and resulting MoS_2 thickness, revealing an upward trend in carrier mobility as MoS_2 thickness increases. In particular, the mobility increases by two orders of magnitude as the growth develops from monolayer to 3-layer thickness. Thicker samples (>5 layers) tended to possess large leakage current, likely the result of incomplete reactions of thick Mo precursor samples due to limited diffusion of S through the Mo. Each data point on Figure 2-10c represents a series of measurements on a single growth sample, resulting in some variability in the mobility between different growth trials; this can be seen especially in the sample from 1.20 nm precursor growth, which showed mobility lower than expected. The largest carrier mobilities reach $\mu_{EF} =$ 0.05 $cm^2V^{-1}s^{-1}$, a low value but comparable with literature values of mechanically exfoliated or CVD-grown MoS_2 that typically range from 0.003 to tens of $cm^2V^{-1}s^{-1}$ for two-terminal, back-gated, untreated, ambient environment transistors[20,25,29,62]. A key reason for the relatively small mobility is the small domain size of our samples, as previously shown via TEM to be 5-20 nm. The use of atomically smooth growth substrates would likely increase the mobility substantially by reducing the grain boundary density; however, in this study, only MoS_2 grown on Si/SiO_2 was used for transistor fabrication to facilitate rapid device analysis for a large number of samples. Future device experiments will utilize atomically smooth substrates, such as sapphire or Si_3N_4, to both increase the domain size of the MoS_2 and facilitate coherent interfaces between adjacent domains; these qualities improve electronic performance.[63] Another factor that could contribute to low mobility is a possible sulfur deficiency in the films; future thickness-dependent stoichiometry measurements can help to further assess this potential

deficiency. Subsequent sulfur-annealing treatments may be effective at improving the S:Mo ratio of our films[32], and a study of these treatments is also a potential future direction. However, even the current un-optimized mobility values demonstrate adequate quality to produce electronic devices, with device quality expected to increase with future trials.

2.2 MoS$_2$ TVS Conclusions

We have shown that thermal vapor sulfurization using MoS$_2$ powder precursor can be a reliable way of producing wafer-scale, uniform, and thickness-controlled MoS$_2$ with properties suitable for use in optoelectronic devices. Monolayer MoS$_2$ has been verified by AFM, TEM, Raman microscopy, and photoluminescence to be of good quality. In addition, we have established a strong linear correlation of 0.65nm MoS$_2$ (monolayer thickness) yielded per 0.37nm precursor molybdenum from monolayer to 5 layer MoS$_2$, consistent with cross-sectional TEM data. Our TVS results are of good optical (3.16 x 10^{-4}% IQE) and electrical quality ($\mu_{EF} = 0.05$ cm^{2}V^{-1}s^{-1}), but importantly, they are made in wafer-scale quantities with greater ease, thickness control, and uniformity than competing CVD synthesis methods. Electrical quality can still be optimized further, and recommendations are made to use atomically smooth growth substrates for future trials. These results represent a foundation from which other 2D materials may be synthesized, and onto which cm-scale optoelectronic and photovoltaic devices may be fabricated. These growth results establish TVS as a flexible and scalable platform for producing wafer-scale monolayer and few-layer MoS$_2$, providing a foundation for ultra-lightweight and efficient 2D devices.

2.3 DETAILS OF GROWTH AND ANALYSIS

Si/SiO$_2$ and c-m plane sapphire wafers were used as the MoS$_2$ growth substrates. Before

TVS, the substrates were O$_2$ plasma cleaned at 45 W for 3 minutes, and then

molybdenum films (thickness range 0.1 to 2.6nm) were deposited onto the cleaned wafers

via electron beam evaporation (Angstrom Engineering Nextdep System). During the

molybdenum deposition, the chamber pressure was between 1 and 2 μtorr and the

substrates were mounted on an unheated, rotating stage. The molybdenum film

deposition rate was verified by AFM to determine precursor thickness. The molybdenum

precursor films, on both Si/SiO$_2$ and sapphire, were then placed in a 1" fused quartz tube

inside a double-chamber tube furnace, positioned in the left chamber. A boat containing

1,000mg of powder MoS$_2$ (Alfa Aesar) was placed upstream in the right chamber.

Before the heating process is started, the system is pumped down to 50mTorr for 1 hour

to remove water vapor and other impurities from the chamber. After the pumpdown,

50sccm of argon carrier gas was initiated to flow through the tube and transport the MoS$_2$

vapor downstream to the molybdenum precursor films, resulting in a growth chamber

pressure of 570mTorr. The heating process was then started, bringing the left chamber

(Mo precursor films) to 830℃ and the right chamber (powder MoS$_2$) to 900° with a ramp

time of 90 minutes and soak of 15 minutes. After the heating process, the furnace was

allowed to naturally cool to room temperature. Optimization of growth parameters was

carried out in prior experiments and is detailed in the supplementary data. In addition,

the role of oxygen was probed by experimentally injecting O$_2$ gas into the reaction in

varying amounts, as shown in Appendix A.

The growth process was repeated with differing Mo precursor thickness, with all other process parameters remaining unchanged to ensure consistency between trials. Within a few hours after each growth, photoluminescence measurements were taken on multiple locations on each MoS_2 film with an Ocean Optics QEPro spectrometer. The samples were excited with a 405nm laser. Afterwards, optical transmission measurements were taken of the sapphire-grown MoS_2 samples, also taken using a QEPro spectrometer and a deuterium-halogen white light source. Atomic force microscopy (AFM) was carried out using a Bruker Dimension Icon AFM. Raman spectroscopy was carried out on multiple locations on each sample to determine MoS_2 thickness and verify crystal quality and uniformity. Raman measurements used a 532nm incident laser. Transistor devices were directly fabricated on the MoS_2 films grown on Si/SiO_2 substrate by patterning and depositing 30nm of gold with a 5nm titanium contact layer. Transistor channels were 9µm wide and 6 µm long, with a 300nm thick gate dielectric layer of SiO_2. High resolution TEM analysis was carried out on certain samples using a Jeol JSM-2011 to probe crystal morphology. Cross-sectional TEM samples were prepared using a FEI Quanta 3d SEM/FIB focused ion beam (FIB) and analyzed using a Jeol JSM-2011 high resolution TEM. Further details on growth can also be found in Appendix A.

3   RAPID-THROUGHPUT SOLUTION-BASED PRODUCTION OF WAFER-SCALE 2D MOS$_2$

In this chapter, we introduce a second MoS$_2$ growth technique developed over the course of this thesis work. This growth technique was developed largely in response to the long device processing times required for CVD and furnace-based techniques, which severely limits MoS$_2$ growth throughput. To allow MoS$_2$ growth to proceed at a more practical speed, we devised a growth technique that synthesizes MoS$_2$ using 15 minutes of thermal processing time via the rapid thermal annealing of a solution-processed $(NH_4)_2MoS_4$ precursor. The technique is shown to produce uniform trilayer MoS$_2$ across 4-inch wafers. Raman spectroscopy, in-plane XRD, and XPS are used to confirm a 2H MoS$_2$ crystal structure with stoichiometry of 1.8:1 S:Mo. AFM is used to confirm 2.0 nm thick MoS$_2$ with 0.68 nm roughness. Photoluminescence and transmission spectroscopy reveal the characteristic 1.85 eV bandgap. As-grown films were used to make field-effect transistors with mobility of 0.022 cm^{2}V^{-1}s^{-1}, demonstrating their potential for optoelectronic device development. This rapid thermal processing growth technique reduces MoS$_2$ synthesis time by an order of magnitude relative to comparable techniques and enables greater accessibility to 2D semiconductors for researchers and developers. This chapter details these advances, and the implications for future 2D work.

3.1   DEVELOPMENT BACKGROUND

Although furnace-based techniques such as CVD and TVS, introduced in the introduction and in chapter 2 of this thesis, are the most common means of growing large-area MoS$_2$, an alternative growth route is the thermal reduction of MoS$_4$ to MoS$_2$. This method is

fundamentally different in that, rather than sulfur being added to a molybdenum precursor, sulfur is removed from MoS_4 compounds to ultimately reduce to MoS_2. In particular, $(NH_4)_2MoS_4$ dissolved in ethylene glycol, or similar solvents, has proven to be a reliable precursor for MoS_2 growth. $(NH_4)_2MoS_4$-based liquid precursor can be dip-coated,[64] spin-coated,[65] or bar-coated[66] onto substrates to form thin precursor films, which are then reduced to 2D MoS_2 when heated in the presence of H_2 or sulfur vapor. Variations of this technique show great promise by demonstrating few-layer MoS_2 growth with field-effect mobility up to 4.7 $cm^2V^{-1}s^{-1}$.[64] Because the reaction is solution-processed and requires only one chemical precursor, it is an appealing option for high-yield and rapid TMDC growth, such as roll-to-roll processing.[66] However, roll-to-roll systems are not commonly found in most research labs and are better suited to large-scale manufacturing. To make 2D MoS_2 truly more obtainable for developers, a simpler, faster, and more cost-effective growth technique is needed that can rapidly iterate through samples. In response to this, we have developed a rapid thermal processing (RTP) technique to demonstrate that the reduction MoS_4 to high-quality MoS_2 can be achieved in as little as 15 minutes under the right conditions in a simple setup. The RTP accomplishes this by using high-intensity visible irradiation to heat samples to 1000 °C in an isolated quartz chamber, and by utilizing convective cooling to rapidly cool samples back to room temperature. While traditional furnaces require 1 hour to heat up and 3-4 hours to cool down, the RTP heats to process temperatures within 30 seconds and cools back to <100 °C within 3 minutes. This RTP growth method produces 2D MoS_2 faster than any other reported MoS_2 growth technique and is capable of performing dozens of growth trials per day, increasing MoS_2 synthesis throughput by an order of magnitude.

This speed will accelerate 2D MoS_2 availability and development into commercially viable technologies.

3.2 RTP GROWTH METHODS

Prior to rapid thermal processing, a 0.75% (by weight) solution of $(NH_4)_2MoS_4$ is prepared by combining 60 mg of $(NH_4)_2MoS_4$ (99.97%, Sigma-Aldrich) with 7940 mg ethylene glycol (Sigma-Aldrich) in a small vial. The vial is then sonicated for 20 minutes to mix the solution. Afterwards, solutions are passed through a 220 nm syringe filter to remove particulates. Substrates, either Si/SiO_2 or sapphire, are first cleaned in acetone and isopropanol and then O_2 plasma treated to promote surface activation. Immediately after, the $(NH_4)_2MoS_4$ solution is spin-coated onto the substrate at 3000 RPM for 30 seconds. The sample is then annealed on a hot plate at 100 ^{o}C to remove residual solvent. Solutions of 0.25%, 0.5%, 1.25%, and 2.5% $(NH_4)_2MoS_4$ in ethylene glycol were also prepared using corresponding precursor ratios in order to produce MoS_2 of different thicknesses. Once the solution is mixed, which may be done in large batches, the total time to prepare the precursor film for thermal processing, in a non-automated lab process, can be as low as 10 minutes.
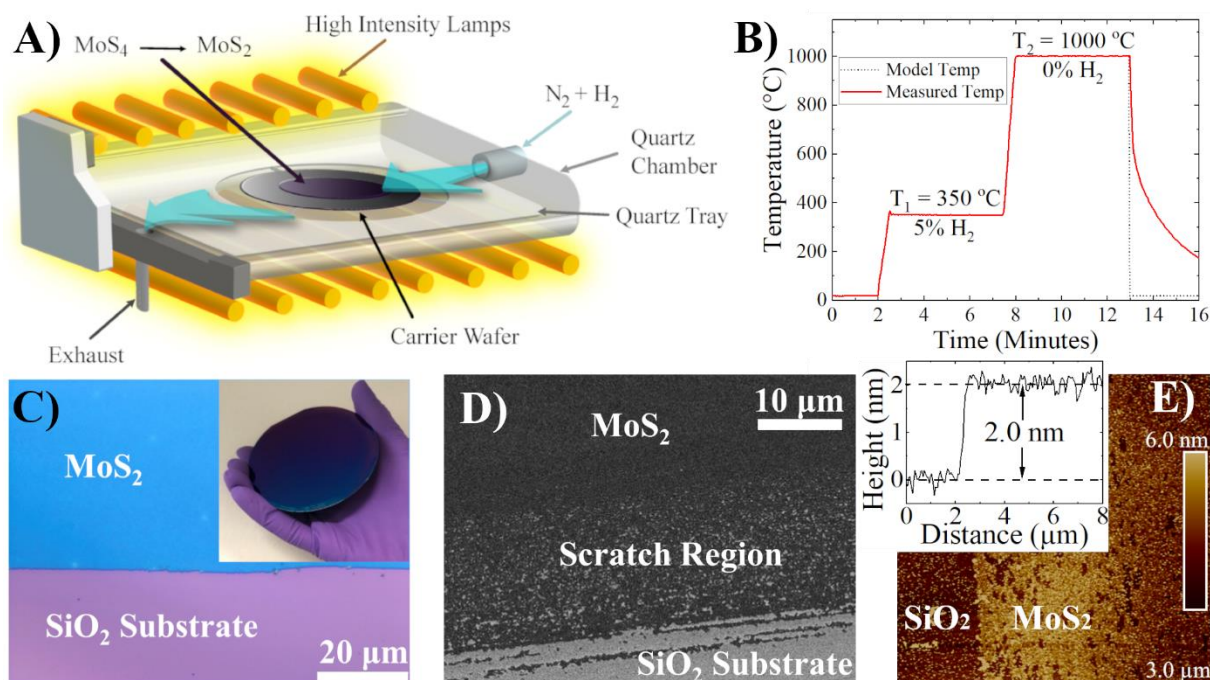
Figure 3-1 (A) Schematic of RTP growth chamber (B) RTP growth temperature profile showing 15-minute growth sequence (C) optical microscope image showing intentionally-induced scratch step edge and growth on a 4 in wafer (inset) (D) High-resolution SEM image of trilayer MoS_2 showing a scratch region and uniform MoS_2 beyond the scratch (E) AFM micrograph of trilayer MoS_2 scratch region showing a 2.0 nm step edge (inset)

After spin-coating, samples are placed in an RTP system (Allwin21 Corp. AccuThermo AW 610), as shown in Figure 3-1A. The samples sit in a transparent quartz isolation chamber atop a silicon carrier wafer. The chamber is maintained at atmospheric pressure, and N_2 and H_2 gas are flowed through the chamber using two mass flow controllers. The samples are surrounded by 21 1.2 kW tungsten halogen lamps external to the quartz chamber. The lamps directly heat the sample at a rate of 22 °C/s via absorption of visible light, with minimal heating of the optically transparent chamber walls. The temperature of the sample is monitored using a k-type thermocouple in physical contact with the silicon carrier wafer. To rapidly form MoS_2, the samples undergo a two-step heating

process, as shown in Figure 3-1B. Prior to the first step, 10 SLM N_2 with 5% H_2 is flowed through the chamber at room temperature for two minutes to purge the chamber of residual gases. During the next step, called T_1, the sample is heated to 350 ºC with a 30 s ramp, and held for 300 s while under 10 SLM N_2 with 5% H_2. It is primarily during T_1 that MoS_4 is reduced to MoS_2 according to the following two-step reaction:

(1) $(NH_4)_2MoS_4 + H_2 \rightarrow 2(NH_4) + MoS_3 + H_2S$

(2) $MoS_3 + H_2 \rightarrow MoS_2 + H_2S$
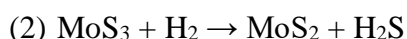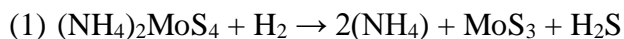
The ammonium and H_2S molecules evaporate and are carried out of the system via the process gas, leaving behind solid MoS_2 on the substrates. During the following step, called T_2, samples are heated to 1000 ºC within 30 s, and held for 300 s under 10 SLM N_2 without hydrogen. This high-temperature step induces MoS_2 crystallization into 2D sheets. Afterwards, the samples are convectively cooled to room temperature under 10 SLM N_2 for 180 s.
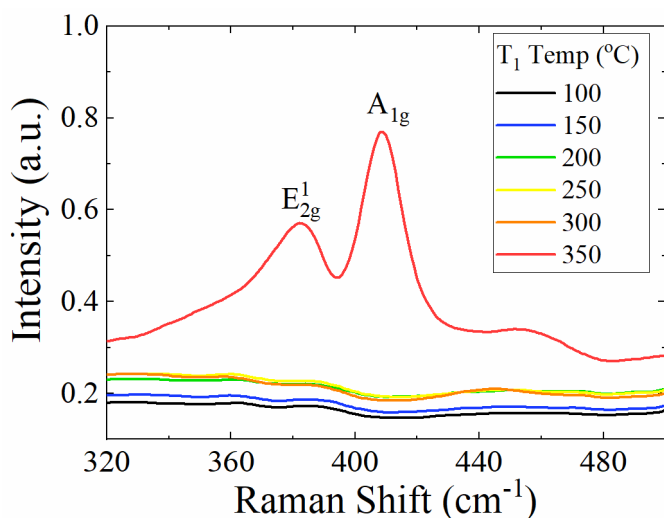
Figure 3-2 Raman scans of samples after only low-temperature first step. MoS$_2$ characteristic Raman peaks first appear at T$_1$ = 350 ºC. Raman spectra are normalized to the silicon substrate Raman peak.

Temperatures T_1 and T_2 were independently experimentally optimized for growth quality.

First, T_1, was optimized by seeking to find the minimum temperature at which MoS_2 was

formed. This was done using the RTP system under 10 SLM N_2 flow (99.999% purity)

with 5% H_2 (99.999% purity) for 5 minutes at temperature, with resultant Raman scans

shown in Figure 3-2. The characteristic A_{1g} and E_{2g}^1 peaks appear only at temperatures

of 350 ºC and above, indicating that this is the minimum required temperature to form

MoS_2 given our growth conditions. Therefore, 350 ºC was selected as the growth

temperature of the first temperature step, T_1, with the intention of forming mostly

amorphous MoS_2 with minimal thermochemical etching. From there, T_2 could be

optimized to tune the crystallization of the MoS_2, as shown later in this chapter.
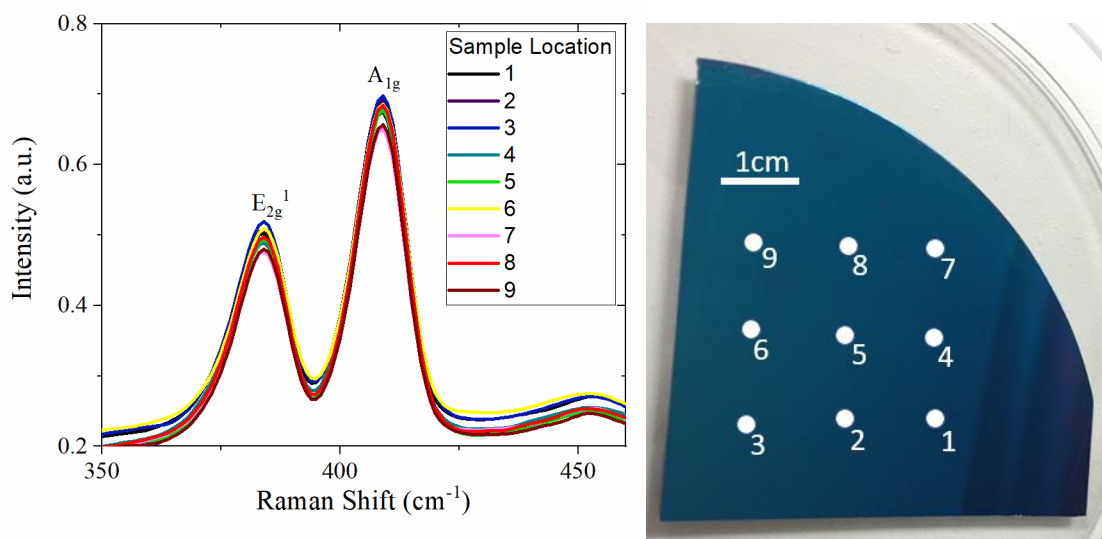
Figure 3-3 (left) Raman mapping of multiple different locations on a 0.75% concentration sample, showing good uniformity. Raman scans normalized to the height of the silicon Raman peak. (right) Scan locations separated by ~1 cm on sample.

3.3 RTP GROWTH RESULTS

The RTP growth method described above produces uniform MoS_2 across 4 inch wafers, as shown in Figure 3-1C (inset), and has capacity to process 6 inch wafers. Some non-uniformity near the edges of the samples is often observed as an artifact of the spin-coating process, but all other regions contain uniform MoS_2. Figure 3-1C shows an optical microscope image of an MoS_2 step edge formed by scratching, contrasting the uniform MoS_2 with the SiO_2 substrate. An SEM image of a similar scratch is shown in Figure 3-1D, resolving a MoS_2 film without pores or notable defects, and also a porous region caused by the scratching. Figure 3-1E shows an AFM map of a 0.75% precursor concentration sample, revealing a surface roughness of 0.68 nm. MoS_2 from a 0.75% sample is shown via AFM step profile analysis to be 2.0 nm thick, corresponding to three molecular MoS_2 layers. This value is in good agreement with MoS_2 thickness from furnace-based synthesis methods, and the ability to control the thickness of MoS_2 by adjusting precursor concentration is a known benefit of the thermal reduction technique.[64,67] In addition, the samples are also shown to be of uniform trilayer thickness across the surface of the samples, as shown via Raman spectroscopy in Figure 3-3.
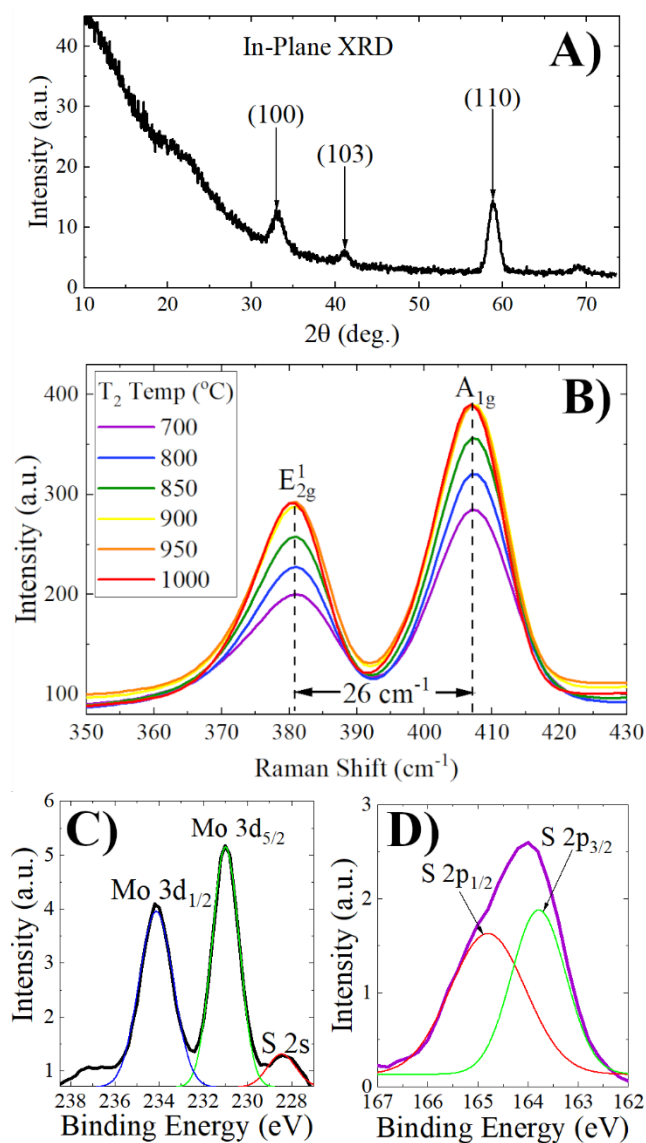
Figure 3-4 (A) In-plane XRD scan of MoS₂ grown via RTP (B) Raman spectroscopy of trilayer MoS₂ from multiple T2 growth temperatures during RTP growth process (C, D) XPS spectra of trilayer MoS₂ showing molybdenum and sulfur peaks

The structure of the grown MoS_2 is analyzed using in-plane x-ray diffraction (XRD), as shown in Figure 3-4A. The prominent peaks at $2\theta = 33.1°$ and $2\theta = 58.9°$ correspond to the (100) and (110) planes of 2H MoS_2, respectively. A smaller peak at $2\theta = 41.1°$ is identified as the (103) peak of 2H MoS_2, further validating the presence of the expected 2H semiconducting MoS_2 phase. These peaks are consistent with XRD peaks expected

from the MoS_2 lattice from the symmetry group P63/mmc, and also with card number 77-1716 of the hexagonal lattice parameters after Joint Committee on Powder Diffraction Standards.[68] Raman spectroscopy, as shown in Figure 3-4B for the 0.75% concentration trial, shows the MoS_2 E_{2g}^1 and A_{1g} peaks at 381 cm^{-1} and 407 cm^{-1}, respectively. The 26 cm^{-1} spacing between peaks indicates 3-layer MoS_2, in agreement with AFM findings.[55] The T_2 process temperature was optimized by determining the temperature at which Raman peak height was maximized and full-width half-max was minimized, as shown in Figure 3-4B. The Raman indicate improving peak height and narrower peak full-width-at-half-max with increasing processing temperature, revealing an optimal T_2 temperature of 1,000 °C. X-ray photoelectron spectroscopy (XPS) analysis of a 0.75% concentration sample is shown in Figure 3-4C and Figure 3-4D. The characteristic Mo $3d_{1/2}$ and $3d_{5/2}$ peaks are seen at 234.1 eV and 231.0 eV, while S $2p_{1/2}$ and $2p_{3/2}$ peaks are observed at 164.8 eV and 163.7 eV. In addition, the S 2s peak is also observed at 228.4 eV. From these values, the stoichiometric ratio of S/Mo is calculated to be 1.80, indicating a relatively high density of sulfur vacancies. This is likely caused during the high-temperature annealing phase in which S atoms evaporated from the MoS_2 lattice cannot be replenished due to a lack of sulfur partial pressure in the chamber. This deficiency is likely to cause a high defect density in the lattice, but may be mitigated in future trials by introducing sulfur vapor to the processing chamber, as has been done in other techniques.[64]

3.4   OPTICAL QUALITY

Bulk MoS_2 contains an indirect bandgap at 1.3 eV, which transitions to a direct 1.85 eV gap in the monolayer regime, as already explored with TVS-grown MoS_2.[18,19] This

bandgap is revealed through photoluminescence spectroscopy, as shown in Figure 3-5A

for trilayer MoS_2. The large A exciton peak is seen at $\lambda = 665$ nm, while the smaller B

peak is located at $\lambda = 618$ nm. The splitting of the A and B peak again occurs as a result

of spin-splitting from spin-orbit coupling.[59] The photoluminescence spectra here are

notably smaller than those seen for TVS MoS_2, primarily because the RTP-produced

trilayer MoS_2 is dominated by its indirect bandgap, whereas monolayer TVS-produced

MoS_2 exhibits a direct bandgap. The spin-split A and B peaks can also be seen via

transmission spectroscopy, as shown in Figure 3-5B with multiple sample concentrations

on sapphire substrates. The sample concentrations of 0.25%, 0.5%, 0.75%, and 1.25%

correspond to MoS_2 thickness (layers) of 0.66 nm (1), 1.3 nm (2), 2.0 nm (3), and 3.3 nm

(5). A sharp band edge can be seen at energies lower than the 1.85 eV transition,

indicating that visible light photon absorption in 2D MoS_2 is dominated by excitonic

effects at energies higher than the 1.85 eV band edge at the K-point, although some

absorption is to be expected all the way out to the 1.3 eV indirect bandgap.[19] The

trilayer (0.75% concentration) MoS_2 sample is shown to absorb 23.4% of light in the 400

nm – 700 nm visible range, or 7.8% per MoS_2 layer, similar to other MoS_2 samples.[41] It

is this high per-layer absorption, combined with the direct K-point transition, that enables

MoS_2 to be made into high-quality optoelectronic devices despite nanometer-thick active

areas.
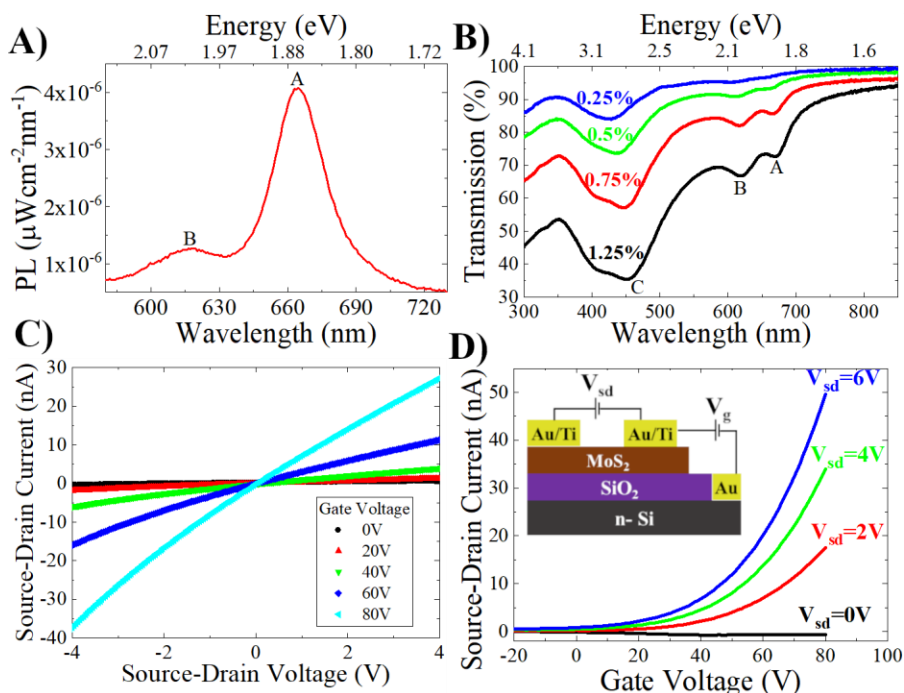
Figure 3-5 (A) Photoluminescence (PL) spectrum from a trilayer MoS$_2$ sample taken with a 532 nm excitation laser (B) Transmission spectra of MoS$_2$ from multiple precursor concentrations (C) Gate-sweep at 6 V source-drain with device configuration inset (D) Source-drain current vs source-drain voltage at different gate voltages

3.5   ELECTRONIC QUALITY

Field-effect transistors were fabricated onto as-grown MoS$_2$ on SiO$_2$/Si substrates to test electronic and optoelectronic performance relevant to potential applications. The transistors contained 40 nm thick Au contacts with a 15 nm Ti adhesion layer as shown in Figure 3-5D's inset. Devices were made with several different channel widths ranging from 9 μm to 30 μm, with channel length of 6 μm. Source-drain sweeps are shown in Figure 3-5C, with linear correlation indicating ohmic contacts are made. An example back-gated field-effect transistor with a 30 μm gate width and 6 μm length is shown in in Figure 3-5D, with gate sweeps taken at source-drain voltages V_{sd} = 0 V, 2 V, 4 V, and 6 V. The transistor demonstrates n-type transistor behavior and I_{on}/I_{off} ratio of 100.

Fabricated devices exhibit field effect mobility of up to 0.022 $cm^2V^{-1}s^{-1}$, a relatively low mobility value but comparable to many other large-area growth techniques which require much longer MoS_2 synthesis time than the results shown here.[28,29] The low mobility is partially due to sub-stoichiometric MoS_2, which may be addressed in future trials by introducing sulfur vapor to the chamber, as discussed earlier. A second reason for low mobility is likely small crystal domain sizes on the order of tens of nanometers, similar to TVS-grown MoS_2; however, in the future, it is expected that vertical device architectures will become the common orientation for optoelectronic applications, in which case the mean free path length of charge carrier transport will be on the order of nanometers and not be significantly affected by lateral grain boundaries.[24,58] Further discussion on this will be made in the following chapter. We furthermore show in Figure 3-5D that the source-drain sweeps of these devices are approximately linear, indicating that ohmic contact has been achieved between the contacts and the MoS_2.

3.6 FUTURE STEPS

The results obtained and presented thus far for RTP-grown MoS_2 are both remarkable and limited. A key limitation has been that growths have been most successful at growing trilayer MoS_2, while further optimization is necessary to achieve growth of various 2D thicknesses on-demand. Monolayer MoS_2 would be a crucial next step to proving out RTP as a broadly useful technique. We and others[66] have demonstrated that the thickness of MoS_2 can be tuned by tuning the concentration the ethylene glycol/$(NH_4)_2MoS_4$ precursor spin-coated onto substrates. However, as the concentration lowers below 0.75% to approach the monolayer regime, we observe that spinodal decomposition begins to occur, resulting in discontinuous island growth rather than

uniform 2D sheets. Several routes exist to overcome this limitation. For example, we demonstrated that treating growth substrates with O_2 plasma to induce hydrophilicity helped to improve MoS_2 growth and adhesion on the substrates; further improvements in adhesion or hydrophilicity may enable sufficiently dilute $(NH_4)_2MoS_4$ solutions to adhere to substrates without collapsing into islands. Increased adhesion may be made with dry plasma treatments or with liquid chemical treatments. Other researchers have also proposed and demonstrated dissolving MoS_2 precursor into viscous polymer-based solvents, rather than ethylene glycol, to promote structural stability during the thermal reduction phase.[69,70] Combinations of these efforts will likely allow monolayer-thick MoS_2 to be reliably produced by solution-processed means in the future, and therefore should be a continued research effort.

3.7 CONCLUSIONS

In summary, few-layer MoS_2 has been synthesized in approximately 15 minutes using a $(NH_4)_2MoS_4$ precursor and a visible-light based rapid thermal processing system. This synthesis requires an order of magnitude less time than any comparable MoS_2 growth technique, enabling rapid production of wafer-scale MoS_2. The MoS_2 is shown to be crystalline and of the 2H phase, showing characteristic MoS_2 in-plane XRD peaks, Raman signal, and XPS peaks. The 1.85 eV bandgap yields a prominent photoluminescent peak at 665 nm, and transmission spectroscopy shows a clear band edge at 1.85 eV. Trilayer MoS_2 displays a visible-spectrum absorption of 23.4% and 7.8% per layer. Transistors show a field-effect mobility of 0.022 $cm^2V^{-1}s^{-1}$ and display ohmic contact. These results indicate that the MoS_2 grown via this rapid thermal processing technique is of good quality and can be used to fabricate a variety of

optoelectronic devices. The rapid production technique shown here will lead to more frequent growth iterations, which will in-turn produce more data and discoveries regarding 2D MoS_2 and other 2D TMDC's. Furthermore, combined with roll-to-roll solution processing, this synthesis technique is promising as a high-throughput method of producing MoS_2, assisting with the development of commercially-viable 2D materials and technologies.

3.8 EXPERIMENTAL DETAILS

We list some key experimental details are listed in this final section, with remaining details to be found in Appendix B.

3.8.1 Sample Characterization

High-resolution SEM images were taken using a Hitachi S-4800 FESEM, and AFM data was taken in tapping mode with a Bruker Dimension ICON AFM. In-plane XRD spectra were taken using a Bruker AXS GmbH D8 Discover at an incident angle of $\alpha_i = 0.251^\circ$. Raman spectra were taken using a 532 nm excitation beam (Kaiser Optical Systems). Photoluminescence spectra were taken using a 532 nm excitation beam (Fianium SC 400 supercontinuum laser with laser line tunable filter) and measured via an Ocean Optics QEPro spectrometer. Transmission spectra were taken using a Perkin-Elmer Lambda HP system. Photocurrent measurements made using the above-referenced tunable supercontinuum laser (Fianium).

3.8.2 XPS Characterization and Analysis

XPS measurements were conducted on a VG Scientific MKII system using a Mg Kα anode as excitation source (hν = 1253.4 eV). The pressure in the chamber during analysis

was $<5\times10^{-8}$ mbar. Peak fitting was performed with a custom VBA program using Voigt profiles together with a Shirley background function.

4 OPTOELECTRONIC DEVICES OF SYNTHETICALLY GROWN MoS₂

In our previous two chapters we introduced two unique growth methods with which to synthesize large-area MoS_2. With each of those methods came a suite of analyses to validate the structural, optical, and electronic quality of the grown MoS_2. However, because the long-term goal of this growth, and the motivation for this thesis, is ultra-thin optoelectronics from MoS_2, we dedicate this chapter to the fabrication, testing, and analysis of optoelectronic devices on our grown MoS_2. The devices shown in this chapter indicate the potential for the grown MoS_2 to be further developed into detectors, LED's, or photovoltaics, and in the final section of this chapter we propose a roadmap to achieve large-area 2D photovoltaics.

The simplest optoelectronic devices fabricated onto our grown MoS_2 films are biased photodetectors. Conveniently, the same device structure used for field-effect transistors can also be used for photodetectors, and so in most cases the same actual devices are used for both electronic and optoelectronic tests. As in previous tests, a bias must be applied between the source and drain electrodes of the photodetectors in order for current to flow through the channel. However, rather than using an external electric field to induce conduction via a gate bias, as is the case with field-effect transistors, photodetectors reduce channel resistance when irradiated with light, thus resulting in current flow through the channel. Both the intensity and the energy of the incident light affect the

current flowing through the channel. The first standard experiment performed on our MoS$_2$ photodetectors is a monochromatic power sweep, which measures photoresponsivity as a function of incident light power. The second is a spectral photocurrent sweep, which measures channel current as a function of incident light wavelength. To account for varying light powers with spectral sweeps, this measurement is expressed as quantum efficiency, either internal or external. The following sections detail these measurements and summarize the results for synthetically grown MoS$_2$.

4.1 DEVICE MEASUREMENT METHODS

We start with the devices described previously in chapter 2 and chapter 3, and diagramed in Figure 2-10B (inset) and Figure 3-5C (inset). To measure these devices as transistors, a source-drain bias V_{sd} is applied across the source and drain contacts. With no other stimuli, the device with only a source-drain voltage will not conduct current and is effectively in an "off" state. However, if the channel is irradiated with light of energy greater than the bandgap of the MoS$_2$, current flows through the channel and the device effectively becomes a photodetector. In our case, the light is provided by a Fianium supercontinuum laser coupled to a laser line tunable filter (LLTF), which can output individual monochromatic laser lines in user-controlled 1 nm spectral increments. A 20x microscope objective lens is typically used to focus the laser to a small spot size, and the spot is then manually aligned onto the device channel.

A useful way to quantify the performance of a photodetector is through external quantum efficiency (EQE), equivalent to the fundamental ratio of the number of electrons collected by a device divided by the number of photons incident on the device.

Experimentally, we measure EQE by sweeping the laser wavelength from 400 nm to 800

nm in 1 nm increments, while the source-drain current, I_{sd}, is measured at every

wavelength. Immediately following the photocurrent measurement, the sample is

removed and the laser power, P, is measured at each wavelength using a NIST-calibrated

photodiode. From this power, the power incident on the channel area, $P_{in}(\lambda)$, can be

calculated according to the equation:

$$P_{in}(\lambda) = \frac{PA_{channel}}{A_{spot}}$$

Where $A_{channel}$ is the area of the device channel, and A_{spot} is the area of the laser spot.

From there, the EQE can be calculated according to the relationship:

$$EQE(\lambda) = \frac{Electrons\ Out}{Photons\ In} = \frac{I_{sd}(\lambda)}{q}\frac{hc}{\lambda P_{in}(\lambda)}$$

Where q is the charge of one electron, h is Planck's constant, c is the speed of light in

vacuum, and λ is the incident wavelength. EQE is a measure of the efficiency at which a

device absorbs photons and extracts them in the form of conduction electrons. However,

an absorption-independent variation known as internal quantum efficiency (IQE) is also a

useful metric to calculate. IQE can be calculated using the simple expression

$$IQE(\lambda) = \frac{electrons\ out}{photons\ absorbed} = \frac{EQE(\lambda)}{A(\lambda)}$$

Where $A(\lambda)$ is the MoS_2 absorption at a particular wavelength. Generally, absorption is

measured separately by using optical spectroscopy to measure transmission $T(\lambda)$ and

reflection $R(\lambda)$. Absorption can then be calculated according to $A(\lambda) = 1 - R(\lambda) - T(\lambda)$.

Another metric commonly used to characterize photodetector performance is responsivity, which measures the current output per optical power input of a device. Responsivity can be calculated using the relationship:

$$Responsivity(\lambda) = \frac{I_{sd}(\lambda)}{P_{in}(\lambda)}$$

However, unlike EQE, responsivity is measured at a single wavelength while only P_{in} is varied. MoS_2-based photodetectors have been shown to have a strong responsivity dependence on incident power due to trap states at higher powers.[35] Both responsivity and EQE will vary based on V_{sd}, and we have typically measured both at a constant $V_{sd} = $ 6 V.

4.2   PHOTODETECTORS ON MOS$_2$ GROWN VIA TVS AND RTP

In previous chapters, we have established the crystalline and electrical quality of MoS_2 grown via our custom-developed synthesis techniques. However, optoelectronic measurements will speak more directly to the potential for development into photovoltaics. For example, Figure 4-1 shows the performance of a RTP-grown MoS_2 transistor illuminated with a laser without any gate voltage applied. In this ungated state, the device is considered "off", but can be turned on using an incident laser beam. In this case, the lase is focused on the transistor channel with a wavelength of 625 nm and a power of 0.012 mW. This simple experiment shows that the grown MoS_2 has a photoresponse, which we may quantify using responsivity and quantum efficiency metrics.
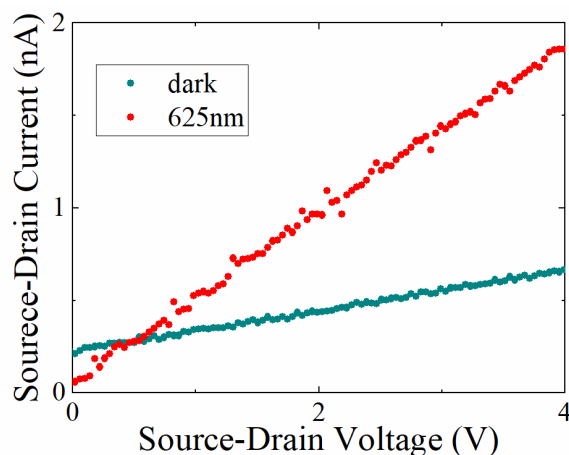
Figure 4-1 Dark and illuminated source-drain sweeps (625 nm illumination at 0.012 mW) taken on trilayer RTP-processed MoS$_2$

In Figure 4-2, the measured responsivity of monolayer and bilayer MoS$_2$ grown via TVS is displayed, with the device measurement schematically illustrated in Figure 4-2 inset. The first striking attribute is the ~12x increase in responsivity of monolayer MoS$_2$ vs bilayer MoS$_2$. This result is not unexpected, given the similar increase in photoluminescence quantum yield at the monolayer MoS$_2$ transition (Figure 2-9). Monolayer responsivity reaches approximately 35 mA/W, whereas bilayer reaches 1 mA/W. In 2012, Yin and co-workers first reported responsivity from very similar devices on exfoliated MoS$_2$ and showed a maximum responsivity of 7.5 mA/W.[71] Considering the responsivity of MoS$_2$ has been shown to vary under different contact schemes and external conditions,[35] we can conclude that the responsivity, and therefore optoelectronic quality, of TVS-grown large-area MoS$_2$ is similar or greater than exfoliated MoS$_2$, thus accomplishing a primary initial goal of our MoS$_2$ growth.
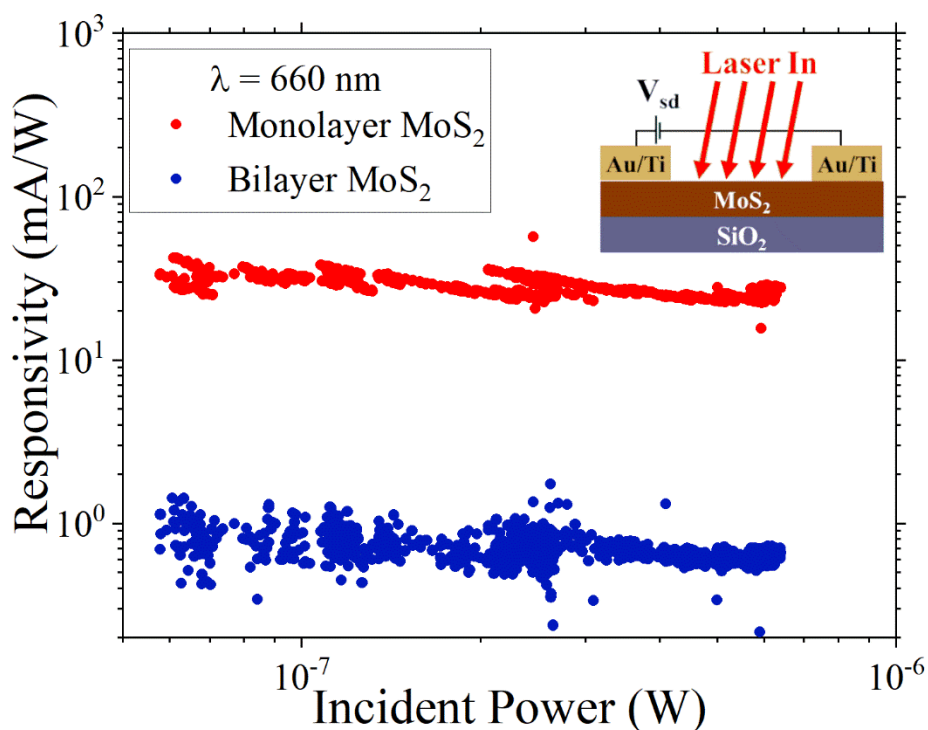
Figure 4-2 Responsivity of monolayer and bilayer MoS$_2$ grown via TVS, showing a ~12x improvement in responsivity for monolayer MoS$_2$. Measurements taken at source-drain bias V$_{sd}$ = 6V and at room temperature with no gate voltage applied.

The responsivity study was expanded to include RTP-grown MoS$_2$, as shown in Figure 4-3. In this case, a wider range of lower incident laser power was used to irradiate the device, enabling a maximum responsivity of 300 mA/W, with an excitation wavelength of 620 nm. This result also demonstrates the trend seen in literature in which the responsivity of biased 2D photodetectors increases as power incident on the channel decreases due to the presence of trap states in the films.[35] The responsivity is comparable to that seen in untreated exfoliated MoS$_2$ measured at similar incident light irradiance. In the case of these RTP-grown MoS$_2$ devices, it is highly encouraging that responsivity remains competitive despite using MoS$_2$ grown in a fraction of the time of

competing techniques. It is also believed that this responsivity could improve further if the crystal lattice quality is improved in the ways outlined in chapter 2 and chapter 3.
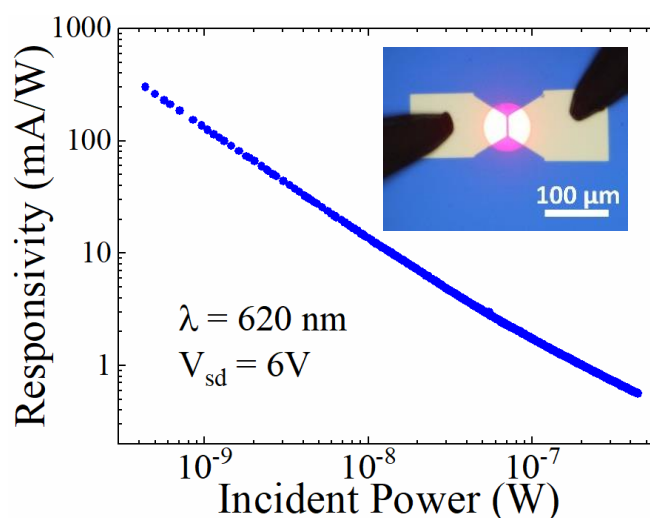
Figure 4-3 Responsivity of a device fabricated onto a trilayer MoS₂ film grown via RTP showing responsivity up to 300 mA/W while under low incident power.

We next present the spectral EQE measured for TVS-grown monolayer and bilayer MoS$_2$, as shown in Figure 4-4. EQE gives a unique glimpse into the fundamental photon-electron conversion efficiency of a device, rather than the power conversion efficiency. As such, spectral EQE plots can reliably show energy-independent spectral regions of increased collection efficiency. Similar to responsivity, a ~12x increase in EQE is shown in monolayer MoS$_2$ relative to bilayer MoS$_2$. We also see the A and B exciton peaks, matching those seen in transmission spectra in MoS$_2$. We note that the EQE peaks seen in this case are largely due to increased photon absorption in those regions, which can then be converted to electrons which are subsequently collected at the contacts. We also see a distinct C peak at ~411 nm, offset from the typical location of C peaks as resolved

from transmission spectroscopy. For both samples, the largest EQE values are found at the C-peaks, where high-energy photons are efficiently converted and collected.

,
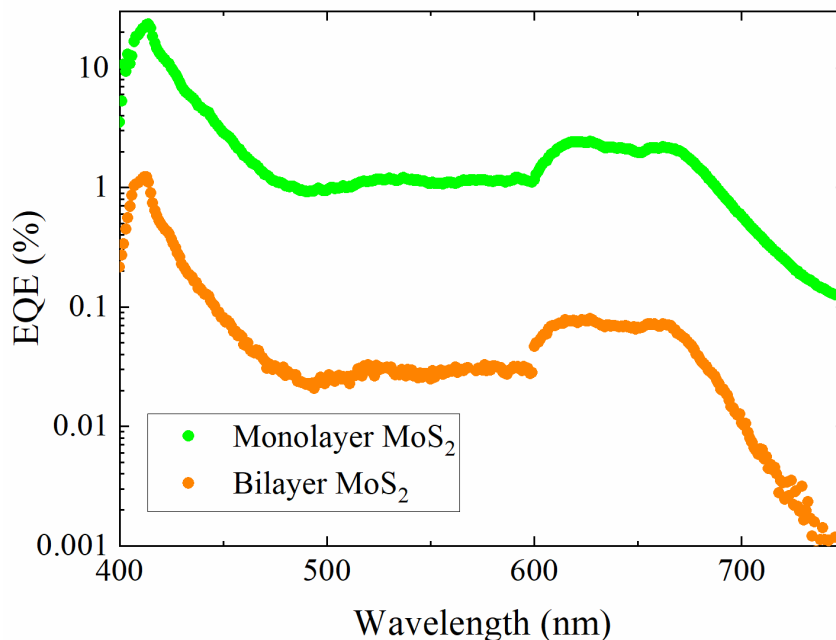
Figure 4-4 External quantum efficiency of monolayer and bilayer MoS₂ grown via TVS. Measurements taken at source-drain voltage of $V_{sd} = 6V$.

4.3 ROADMAP TO LARGE-AREA 2D PHOTOVOLTAICS

The devices measured thus far in this chapter are all biased photodetectors. As such, they can be used to measure or determine incident light levels, but require an external voltage to do so. In other words, they cannot directly convert optical power to electrical power in the way photovoltaics can. We next propose the steps necessary to develop grown MoS_2 devices from photodetectors to photovoltaics, while doing so in a scalable architecture with the potential for commercial development.

A key limitation of MoS_2 is a relatively low carrier mobility. Carrier mobility in excess of 1000 $cm^2V^{-1}s^{-1}$ has been demonstrated under certain conditions such as high-k encapsulation, 2D edge contacting, and low-temperature measurement. However, single-crystal MoS_2 under normal conditions shows mobility in the range of 1 to 20 $cm^2V^{-1}s^{-1}$ under normal configurations and at room temperature. Mobility is typically even lower for polycrystalline MoS_2, such as that grown synthetically, including through TVS and RTP. Therefore, any design for 2D TMDC photovoltaics must include features to mitigate carrier recombination associated with carrier diffusion lengths longer than the average domain size of the TMDC. One way to do this is to increase the domain size of the MoS_2, which has been a primary goal of the MoS_2 CVD community for the past five years. However, another way to accomplish this is to minimize the carrier diffusion length necessary for photovoltaic carrier collection. In the case of lateral optoelectronic devices, such as those reported in previous chapters, charge carriers must traverse the length of the device channel, or 6 microns in our example. The lower limit of channel length attainable is approximately 50 nm using electron beam lithography techniques, on the same order as the domain size of large-area growth techniques; however, this will require non-standard contact deposition and production techniques, and is therefore not an ideal solution for photovoltaic production.

4.3.1 Vertical Device Architecture

Alternatively, we suggest a transition from lateral device architectures to vertical devices, as is standard for nearly all mainstream photovoltaic systems. This architecture is shown in Figure 4-5 A and B, and contrasted with the lateral devices. In the vertical configuration, the TMDC must lay on top of its bottom contact, rather than on an

insulating dielectric layer. Contacts can then be deposited on top of the TMDC using normal deposition techniques. In this way, the distance that must be traveled by the carriers through the material is approximately equal to the thickness of the material, a few nanometers. Because of this, carrier conduction and collection will not be significantly affected by the small lateral domain size of synthetically grown 2D materials, and therefore the vertical orientation will suffer from a far lower rate of carrier recombination losses relative to lateral devices. The top contact scheme can be demonstrated experimentally using a metallic grid-finger architecture. Alternatively, a transparent top contact such as indium tin oxide (ITO) or graphene could be used to reduce shadowing and lateral transport losses. Another advantage of vertical photovoltaic devices is increased aperture size relative to lateral devices, ultimately leading to increased photovoltaic current. We therefore suggest that future 2D photovoltaic development efforts pursue this end, and we also contribute preliminary results attained over the course of this thesis work.
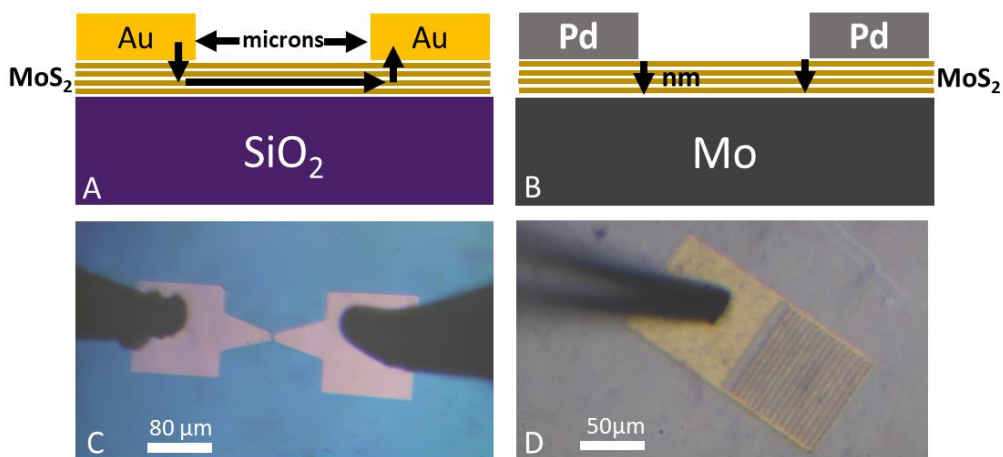
Figure 4-5 (A) Schematic of a lateral MoS₂ device, such as used for FET's, in which electrons must travel microns to traverse the space between contacts (B) Schematic of a vertical MoS₂ Schottky-type photovoltaic device proposed for 2D photovoltaics in which electrons must travel nanometers between contacts (C) microscope image of probed lateral device (D) microscope image of a vertical device on top of MoS₂

A simple first demonstration 2D photovoltaic is the Schottky photovoltaic.[23,72,73] A

Schottky photovoltaic operates by using asymmetric top and bottom contacts such that

one contact selectively accepts holes, and the other selectively accepts electrons. This

asymmetry of contacts creates an asymmetry of charge density, which therefore produces

an internal electric field that drives photovoltaic action. For example, for MoS_2, low

workfunction contacts such as titanium are able accept electrons because their

workfunction aligns with the conduction band of MoS_2. Similarly, high-workfunction

metals such as palladium can align with the valence band of MoS_2, and therefore conduct

primarily holes. When MoS_2 is contacted by both a high workfunction contact and low

workfunction contact, an internal electric field is formed within the material, driving the

photovoltaic effect.[73] This effect has been demonstrated for exfoliated-scale MoS_2,[23,73]

but a scale-up to the mm^2 or cm^2 scale would be a giant leap in 2D TMDC photovoltaics,

and is only possible using synthetic TMDC growth techniques. In the following

paragraphs, we suggest a plausible means to accomplish this for the first time, and present preliminary results toward this goal.

The standard growth substrates for large-scale TMDC growth are high-melting-point insulators such as SiO_2 and sapphire due to their chemical and thermal stability. Currently, to obtain MoS_2 on other substrates, such as metals, MoS_2 is typically first grown on an oxide substrate and then transferred to other substrates using post-processing wet transfers.[74] However, such transfer techniques inevitably leave gaps and holes in the transferred 2D film, which will lead to catastrophic shunt leakages between top and bottom contacts. A preferable route is to grow the 2D material directly onto the bottom contact metal, which removes the defect-prone transfer step. For the MoS_2 to be grown directly onto a metal contact, the metal must be carefully chosen to fit the following criteria:

1. The metal must have a sufficiently high melting point to withstand growth temperatures of up to 1000 °C without physically deforming

2. The metal must be chemically inert such that it will not react with the MoS_2 or precursors

3. The metal must have a sufficiently high or low workfunction to serve as either an electron acceptor or a hole acceptor, respectively

The metals that fit these criteria best are nickel, molybdenum, platinum, and tungsten. Molybdenum and tungsten are appealing choices due to their high melting points, but may be susceptible to sulfur diffusion into the metal forming a chemical gradient. Platinum satisfies all criteria, but is likely too expensive to be a long-term solution, and therefore is not preferred. Nickel also satisfies all criteria and is known to be stable

chemically under high temperatures. Furthermore, both nickel and molybdenum foils

have already been demonstrated to work as MoS_2 growth substrates.[66,75] Nickel and

molybdenum are therefore suggested as the first bottom-contact metal candidates. The

RTP technique can be easily employed to spin-coat TMDC precursor and rapidly form

2D MoS_2 on top of nickel foils. In addition, nickel has already been shown as a viable

growth substrate under certain conditions.[66,75,76] If this growth can be optimized further,

the first large-area 2D photovoltaics can be accomplished with the straightforward

addition of electron-accepting top contact grid finger arrays such as titanium/gold. A

further advancement would be replacing grid fingers with a transparent 2D top electrode,

such as graphene.

4.3.2   Preliminary Vertical Device Results

Progress toward vertical 2D large-scale devices has thus far been primarily confined to

growth on the target bottom contact substrates. For example, the TVS growth technique

of chapter 2 can be modified to replace a thin Mo layer on SiO_2 with a sheet of

molybdenum foil, as illustrated in Figure 4-6. Initial testing indicates that this technique

does indeed synthesize surface MoS_2, as shown in Figure 4-7A, such that a light

scratching can remove the MoS_2 layer to reveal the molybdenum layer underneath. This

is desirable, as it allows the bottom contact to be accessed easily. Furthermore, the

grown MoS_2 is identified by Raman spectroscopy, as shown in Figure 4-7B. Although

this technique appears promising, much work remains to be done toward optimizing the

growth to 2D films, as thicker films are more commonly obtained that are not suitable for

2D applications.

Figure 4-6 Modified TVS growth to use molybdenum foil as a growth substrate to yield a thin MoS$_2$ surface layer, with a large Mo layer remaining underneath.

In addition, some efforts have been made to grow MoS$_2$ onto non-molybdenum metals by spin-coating (NH$_4$)$_2$MoS$_4$ precursors and performing a thermal reduction in the same way as RTP in chapter 3. Limited success has been met thus far, although it is suggested that an optimization of thermal parameters such as was done for RTP can yield MoS$_2$ growth on certain metals. For example, it was found in chapter 3 that RTP growth on SiO$_2$ did not produce MoS$_2$ of adequate electrical quality until process temperatures of T$_2$ = 1000 °C were reached; such high temperatures are likely also necessary for MoS$_2$ thermal reduction on metals. We suggest that these higher temperature regimes be attempted on the metals described above, followed by electrical testing. Finally, we suggest a further study into the mismatch of the coefficients of thermal expansion (CTE) between MoS$_2$ and metal substrates, as any large CTE mismatch will inhibit the proper adhesion of MoS$_2$ onto its substrate.
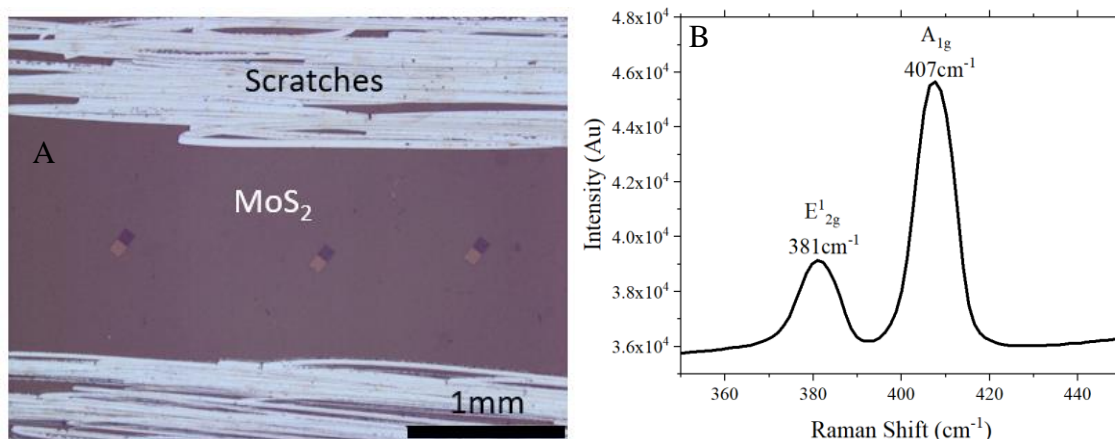
Figure 4-7 A) MoS₂ grown on molybdenum foils using the TVS method, showing a layer of MoS₂ that can be scratched off to reveal molybdenum underneath, B) Raman spectroscopy showing MoS₂ Raman peaks of the grown MoS₂

4.4 CONCLUSIONS

In this chapter, we have demonstrated the optoelectronic qualities of large-scale synthetic 2D MoS₂ via phototransistors, and have also suggested a new architecture to enable large-area 2D photovoltaics in the future. In particular, we argue that vertical devices are critical for 2D photovoltaics. If MoS₂ can be grown directly on top of a bottom metal contact such as nickel or molybdenum, such a device would be very straightforward to produce on both the laboratory scale and the industrial scale, potentially paving the way for widespread 2D photovoltaic use. Before this can happen, 2D MoS₂ must be reliably grown, and we suggest this as a research effort for the near future to prove out the large-area vertical 2D device architecture.

5 FIELD TESTING OF A SPECTRUM-SPLITTING TRANSMISSIVE CONCENTRATOR PHOTOVOLTAIC MODULE

In this chapter we transition from 2D semiconductors and devices to the realm of transmissive photovoltaics. The content of this chapter represents a technology with a relatively high maturity, and with the possibility of large-scale production within just a few years. We therefore include this material with a focus on the steps needed to take this technology from a test-scale validation to large-scale implementation.

5.1 BACKGROUND AND MOTIVATION

The work of this chapter is motivated by the growing demand for more secure, reliable, and cost effective thermal and electric power, and the public and business shift towards renewable energy systems.[77] The increase in energy demand includes both electrical power[78] and process heat.[79] As discussed in section 1.2.1, ~19% of energy incident on photovoltaics (PV) is in the form of above-bandgap infrared (IR) light, which is wasted as a heat byproduct in conventional PV. To circumvent this loss and increase PV system efficiency, there has been a movement over the past 15 years towards hybrid photovoltaic-thermal (PV/T) systems that output both electricity and heat while more efficiently converting the entire solar spectrum.[80,81] In this way, the heat from solar infrared light can be captured and utilized, rather than wasted. For example, significant research has been done on topping mode designs in which PV components absorb all wavelengths and waste heat is captured through a cell cooling system.[82–85] However, this architecture generally cannot yield heat outputs at temperatures above 80 ºC, and

consequently cannot satisfy the heat requirements for most commercial and industrial applications.[79] Furthermore, topping PV/T suffers from reduced PV cell efficiency due to elevated cell temperatures. An alternative is to use spectrum-splitting PV cells that selectively absorb ultraviolet and visible (UV-vis) light for energy conversion, while either reflecting or transmitting IR wavelengths to a physically separated thermal receiver.[86–92] Transmissive photovoltaics have been developed in the past for applications such as building and window-integrated PV, with 1% to 13% efficiency.[93] By utilizing concentrated sunlight and high-efficiency III-V based photovoltaics, and by focusing transmitted light into a dedicated thermal receiver, a new system architecture is made that drastically improves total collection efficiency.[94] This configuration enables thermal decoupling of the PV and thermal systems, allowing the PV components to operate at low temperatures and thermal components at high temperatures.[95] Parabolic troughs can be used to concentrate sunlight onto such a hybrid transmissive receiver, but troughs generally achieve lower concentration than two-axis parabolic mirrors, which can achieve concentration in excess of 1000 suns.[87,96,97] Such concentrations are critical for concentrator photovoltaic (CPV) designs in which the cells operate at >500 suns with thermal system stagnation temperatures of up to 450 °C.[98] Operation at high concentrations allows for both increased PV cell cost effectiveness ($/W) and higher process heat temperatures. In particular, high temperature output heat enables use in industrial processes, the largest consumers of heat.[99] Furthermore, the shared PV and thermal collector infrastructure in concentrator PV/T (CPV/T) designs enable cost reductions, facilitating commercialization in previously unavailable markets.[100] In light

of this, this chapter presents a transmissive CPV (tCPV) module designed for high solar concentrations with applications in industrial process heating and electricity production.

The module designed here, similar to PV/T systems, seeks to optimize performance within the trade-space of electrical performance, thermal performance, and PV thermal management. Most importantly, unlike topping modes, specular transmissivity must be achieved in the tCPV/T module. We have previously discussed the development of GaAs-substrate III-V triple junction PV cells that absorb light of wavelength $\lambda < 870$ nm for electricity conversion, while transmitting IR light for thermal collection.[40] These bare cells achieved up to 24.9% full-spectrum efficiency under 1-sun, and 29.5% efficiency at 500x concentration.[40] In this chapter we demonstrate a module that encapsulates, protects, cools, and electrically connects these cells for outdoor use on a concentrator dish and 2-axis tracker. Along with the cells, all module subsystems are designed to be transparent, including substrates, superstrates, encapsulant, and active cooling systems.[101] Non-transparent module components, such as copper wire electrodes, are utilized sparingly to reduce shadowing while maintaining acceptable series resistance.

5.1.1 Performance Metrics

We introduce three metrics for describing the PV efficiency of the tCPV module, as shown in Table 5-1; the cell efficiency, η_c, describes the power conversion efficiency (PCE) of a bare PV cell in air. The cell area is defined as 0.29 cm^2 and excludes the regions covered by busbar. Module efficiency, η_m, describes the collective PCE of all working cells in the module, and accounts only for sunlight incident on the cell area, given that light spilled outside of the cell area is directed to the thermal receiver by

design. Receiver efficiency, η_r, describes the total PCE of the module aperture and is dependent on the number of cells in the module and their spacing. Because the cells are only designed to convert light of wavelength $\lambda < 870$ nm, we define solar spectrum light of wavelength $\lambda < 870$ nm as "in-band" light, and similarly define solar spectrum light of wavelength $\lambda > 870$ nm as "out-band" light. Therefore, each efficiency metric can be further specified as full-spectrum (AM1.5D) or in-band ($\lambda < 870$ nm). All electrical output power numbers represent two-terminal, max-power-point measurements. One-sun measurements are taken at 25°C and use an AM1.5D calibrated multi-zone solar simulator to define input power. High flux measurements use real outdoor testbed conditions for temperature and input flux, as described further in the text. The key figure of merit for our tCPV system is in-band module efficiency, η_m^{IB}, which most directly speaks to the electrical quality of the module in the context of a tCPV system. We also highlight the out-band transmission ($\lambda > 870$ nm) through the cell area as a key metric.

Table 5-1: Electrical Efficiency Definitions

Term	Definition
Full-Spectrum Cell Efficiency, η_c	$$\eta_c = \frac{Power\ produced\ from\ bare\ cell}{Power\ incident\ on\ bare\ cell}$$
In-band Cell Efficiency, η_c^{IB}	$$\eta_c^{IB} = \frac{Power\ produced\ from\ bare\ cell}{Inband\ power\ incident\ on\ bare\ cell}$$
Full-Spectrum Module Efficiency, η_m	$$\eta_m = \frac{Electrical\ power\ produced\ from\ module}{Power\ incident\ on\ operational\ module\ cell\ area}$$
In-Band Module Efficiency, η_m^{IB}	$$\eta_m^{IB} = \frac{Electrical\ power\ produced\ from\ module}{Inband\ power\ incident\ on\ operational\ module\ cell\ area}$$
Full-Spectrum Receiver Efficiency, η_r	$$\eta_r = \frac{Electrical\ power\ produced\ from\ module}{Power\ incident\ on\ module\ aperture}$$
In-Band Receiver Efficiency, η_r^{IB}	$$\eta_r^{IB} = \frac{Electrical\ power\ produced\ from\ module}{Inband\ power\ incident\ on\ module\ aperture}$$

5.2 DESIGN METHODS

The primary purpose of the module is to encapsulate, protect, and electrically connect an array of cells[40] such that they can reliably perform under concentrated sunlight while still transmitting IR light. As part of these design points, the cells must be actively cooled, which necessitates a unique active cooling system. Electrical, physical, optical, and thermal constraints are balanced to create a module that can operate under the intense conditions associated with concentrated PV.

5.2.1 Physical Design

Figure 5-1A shows an exploded CAD view of the module. The module contains an opto-electronic stack, microfluidic cooling system, and aluminum housing. The opto-

electronic stack is composed of a quartz superstrate, PDMS encapsulant layer, CPV cells, sapphire substrate, and 34 AWG copper electrodes embedded in the superstrate and substrate via InPb solder. The module optical aperture is a 75 mm diameter circular opening at the top of the module, and each CPV cell is 5.5 mm x 5.5 mm x 0.45 mm. Cells are arranged in an array between the quartz superstrate and sapphire substrate and soldered to the embedded copper electrodes. The arrangement of the CPV array can be changed to control the fraction of transmitted light through the module for thermal applications, and a 36-cell 4-quadrant array was chosen for this module. The CPV array and optoelectronic stack is encased in transparent PDMS encapsulant (Sylgard 184). The previously developed microfluidic cooling system contains an aluminum mounting collar, quartz support window, and patterned PDMS microchannels connected to the sapphire substrate.[101] Water is flowed via the channel plate to the cooling channels, which run parallel to and in contact with the sapphire substrate. The CPV cells are cooled via heat transfer from the channels to the cells through the sapphire layer. Water inlet and outlet ports are located in the cooling channel manifold below the channel plate. Sapphire was chosen as the substrate material because it is both thermally conductive and transparent into the IR range, allowing it to transfer heat between the cell layer and cooling water. The cooling water is flowed through a closed-circuit loop, and the PV heat can be extracted through the cooling water system. Figure 5-1B illustrates the operating principle of the photovoltaic module, in which IR light transmits through the module, while visible light is converted to electricity. A photograph of the module is shown in Figure 5-1C, taken after outdoor testing. The CPV cells are visible through the

transparent optical stack, and a white silica ceramic plate covers the top aluminum collar to diffusely reflect spillage light and protect the housing.
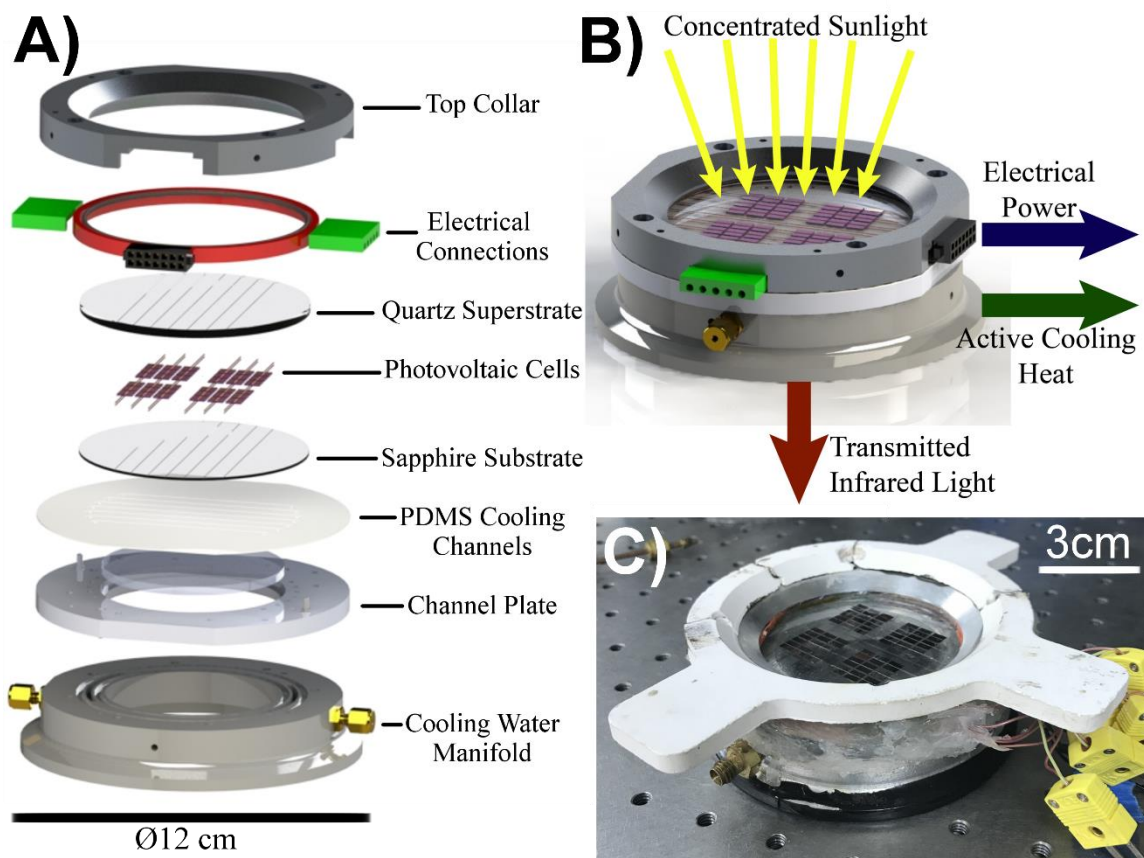
Figure 5-1 A) Exploded diagram of Module 6, including photovoltaic and cooling systems B) Working principle of the photovoltaic module C) Photograph of Module 6 after outdoor testing

5.2.2   Optical Modeling

A transfer matrix-style method is used to calculate the reflection, absorption and transmission of each layer of the module.[91] All interfaces are assumed to be planar, and secondary internal reflections are taken into account. Starting from a simple triple-layer structure, the reflection and transmission between entrance and exit interfaces is obtained

using Fresnel equations. The internal transmittance of each layer can be described by the absorption coefficient of the material and the light path of the beam through the corresponding layer. When multiple reflections between interfaces are considered, the overall transmittance is calculated by summing all light exiting the bottom layer, and the overall reflectance is obtained from the sum of all light exiting at the top interface.[102] When more layers are added, the triple-layer structure can be treated as a single layer with the transmission and reflection calculated as above. Using the same method, the optical parameters for subsequent interfaces can be obtained layer-by-layer. At the interfaces where anti-reflection coatings (ARCs) are applied, the transmittance, reflectance and absorption of ARCs are taken from the ARC model rather than calculated with Fresnel's equation.[91] Shadowing effects from the electrical system wires are included as reflectance at the interfaces in the front and back side of the PV cell.

5.2.3   Thermal Modeling

A 1D thermal model was built to determine photovoltaic cell temperatures and thermal loads during on-sun operation. The model assumes that the entirety of the thermal load conducts through the PDMS encapsulant and sapphire layer directly under the cell. The sapphire is cooled by water flowing through microchannels 100 μm deep and 5.5 mm wide, located below the sapphire layer as shown in Figure 5-1a. The model physical input parameters are displayed in Table 5-2. The temperature of the cells is therefore calculated according to the relationship:

$$T_{cell,ij} = T_{water,ij} + Q_{ij}R_{microfluidics}$$

Where i and j index the cells in the array, $T_{cell,ij}$ is the temperature of cell i j, $T_{water,ij}$ is the calculated temperature of the microfluidic channel water beneath cell i j, Q_{ij} is the heat from cell i j, and $R_{microfluidics}$ is the thermal resistance of the microfluidic channel. The thermal model was used to determine the maximum flux, position the module relative to the concentration focal point, and predict temperature performance for on-sun testing. Further details on this model can be found in appendix F.

Table 5-2: Cooling channel design parameters

Cooling Channel Width	5.5 mm (x 7)
Cooling Channel Depth	100 µm
Reynolds Number (Re)	953
Fluid Flow Velocity	4.3 m/s
ΔT Between Fluid and Cell	40 ºC
Nusselt Number (Nu)	5.36
Convection Coefficient (h)	17,247 W/m^{2}K

5.2.4   Electrical Modeling

The output of the CPV cells was modeled on the system level to predict total module output as a function of incident irradiance. It is assumed that cell current increases linearly with incident solar irradiation such that

$$I = \frac{E_e}{E_{AM1.5D}} I_0$$

where E_e is the irradiance incident on the solar cells, $E_{AM1.5D} = 900$ W/m^2 is the

irradiance at AM1.5D intensity, and I_0 is the current at AM1.5D. We also assume that

the open-circuit voltage of each cell increases logarithmically with current according to:

$$V_{OC} = \frac{nkT}{q} \ln\left(\frac{I}{I_0} + 1\right)$$

Where n=1 is the ideality factor, k is the Boltzmann constant, T is temperature (K), and q

is the elementary charge. From these, the electrical output of the module can be

predicted based on the physical circuit orientation and Kirchhoff's laws. Two modules

with different cell orientations were explored, called Module 5 and Module 6. Module 5

contained a 7x7 array of CPV cells wired all in parallel, as shown in Figure 5-2A. In this

configuration, current adds across all cells while total V_{oc} remains constant at 4 V,

matching that of individual cells. This high-current orientation is prone to resistive losses

according to the relationship $P_{loss}=I^2R$, where P_{loss} is power lost due to resistance R in a

circuit. To reduce internal series resistance losses and electrical current, Module 6 was

designed with four quadrants of 9 cells, as shown in Figure 5-2B. In this configuration,

cells within each individual quadrant are connected in parallel while the 4 quadrants are

wired in series. This results in a relative 4x reduction in current and a 4x increase in

voltage, delivering an expected V_{oc} of 16 V. This reduces resistive losses and also

eliminates the need for external DC/DC converters. However, the quadrant design is

vulnerable to current mismatch losses, as the overall system power will be limited to the

current of the lowest current quadrant. The results presented herein all represent those of

Module 6. The electrical model also incorporates series resistance losses, current

mismatch losses, and optical reflection losses. The CPV cells used in the tCPV module

had an average in-band efficiency at 1-sun of $\eta_c^{IB} = 32.0\%$.[40] For concentrated testing

and modeling, we use the definition of 1 sun as 900 W/m^2 for the AM1.5D spectrum.
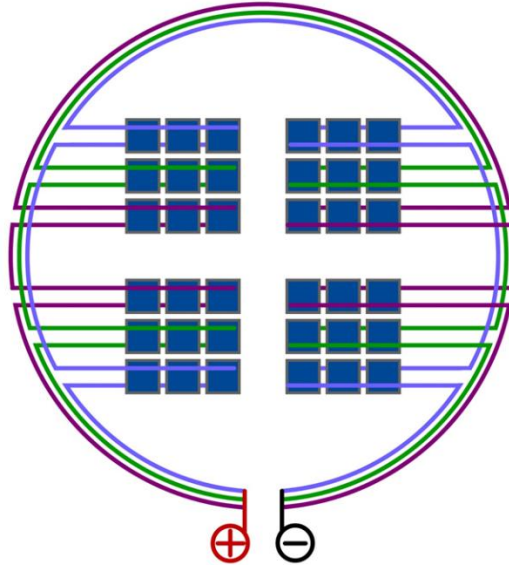
Figure 5-2 4-quadrant circuitry of the module, with each quadrant containing three strings of cells, with total module output voltage of 12 V.

5.3   TESTING METHODS

The module was tested under 1 sun using a solar simulator (AM1.5D Spectrum, TS

Space) as well as outdoors in San Diego using a two-axis tracked 2.72 m^2 concentrating

dish collector (45° rim angle, 1.5m focal length), shown in Figure 5-3. Electrical

performance was measured using a BK Precision 8514 programmable DC electronic load

controlled by a custom LabVIEW code. The load performed an IV sweep on the tCPV

module every 10 minutes and calculated the voltage at the max power point, V$_{max}$.

Between IV sweeps, the programmable load operated at V$_{max}$, recording power

measurements every 15 seconds. Additional details of the testing can be found in

1.1.1Appendix F.
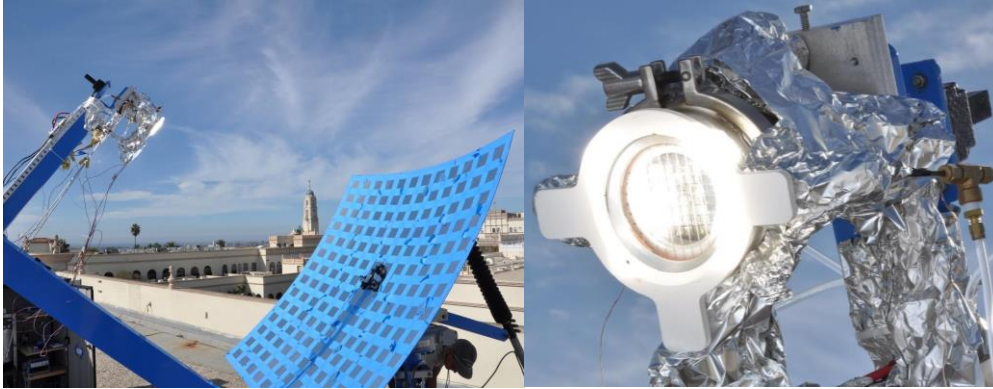
Figure 5-3 (left) Module mounted on top of 2-axis tracker at the focal point of a 2.7m parabolic concentrator dish; blue tape is used to "mask down" dish to control incident flux. (right) close-up of module "on-sun" with concentrated sunlight striking the cells.

5.4 TEST RESULTS AND CHARACTERIZATION

To validate performance, the module underwent more than 60 hours of outdoor concentrated testing, spanning 11 individual test days. Figure 5-4a plots the power flow for one full-day (~7 hour) test of the system at an average concentration of 130 suns, with three distinct power output streams of PV electrical power, PV cooling power, and transmitted optical power. The black line represents the total input power incident on the module aperture, calculated from DNI incident on the mirror calibrated for the mirror and module. In total, 52.7% of the power incident on the module aperture is transmitted through the tCPV module, 18.2% is collected as heat via the PV cooling channels, 4.1% is converted to electrical power via the photovoltaics (η_r), and 22.7% is reflected off the front side of the module. Roughly 4% of the incident power is unaccounted for, which is within instrumentation error and the noise of thermal characterization losses from the thermal receiver and PV cooling heat load. In total, 75% of the optical power incident on the module is therefore collected through one of the output streams, although the PV

electricity and high-temperature thermal receiver power are more useful than the low-temperature PV cooling water. Modeled power output is shown in Figure 5-4a, calculated from module parameters and mean input power. Experimental and modeled results are within 5% agreement for transmitted power and reflected power, matching the model well. Electrical power output is 14% lower than modeled, which is primarily due to the occurrence of cell failures at high concentrations, which will be further detailed in the following sections. This, in combination with increased scattering at the cell surfaces, led to a cooling power output 45% larger than expected from the model. Overall, the power flows are within their expected range and illustrate the multiple output power streams available from this module design.
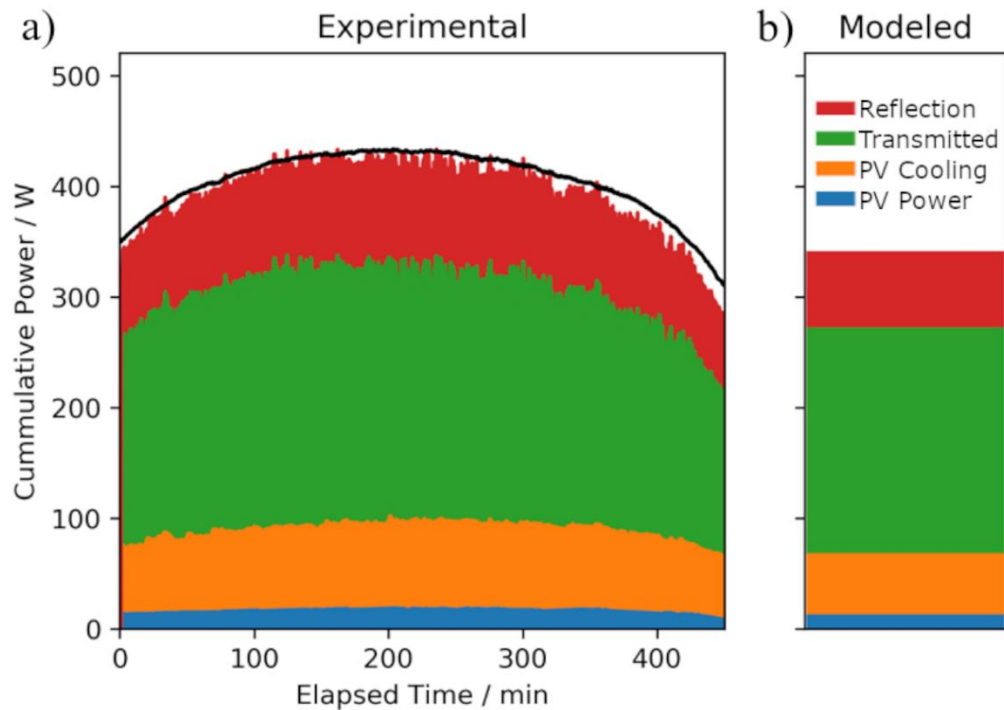
Figure 5-4 a) Power flow measurement and b) model from on-sun testing for tCPV module.

5.4.1 Optical Analysis

One major design requirement for the module is infrared transmissivity. To quantify this, the transmission of the module was measured in an indoor test setup prior to outdoor testing. The modeled and measured transmission of different locations of the module is shown in Figure 5-5, as measured using ocean optics. Some regions of the module contain cells, whereas some contain only "bypass" regions primarily composed of PDMS encapsulant and cooling water. Figure 5-5a shows spectral transmission through the region of the module containing CPV cells. In this region, essentially all in-band light of energy above the 870 nm GaAs bandgap is absorbed by the photovoltaic cell or reflected, whereas 58.8% of light below the bandgap is transmitted. This measured transmission value is lower than the computationally modeled value of 62.9%, a discrepancy which is likely caused by un-optimized anti-reflection coatings on the cell and from diffuse scattering. A prominent transmission dip at 1400-1500 nm is caused by optical absorption in the 100 µm thick water layer of the microfluidic water channels beneath the cells.
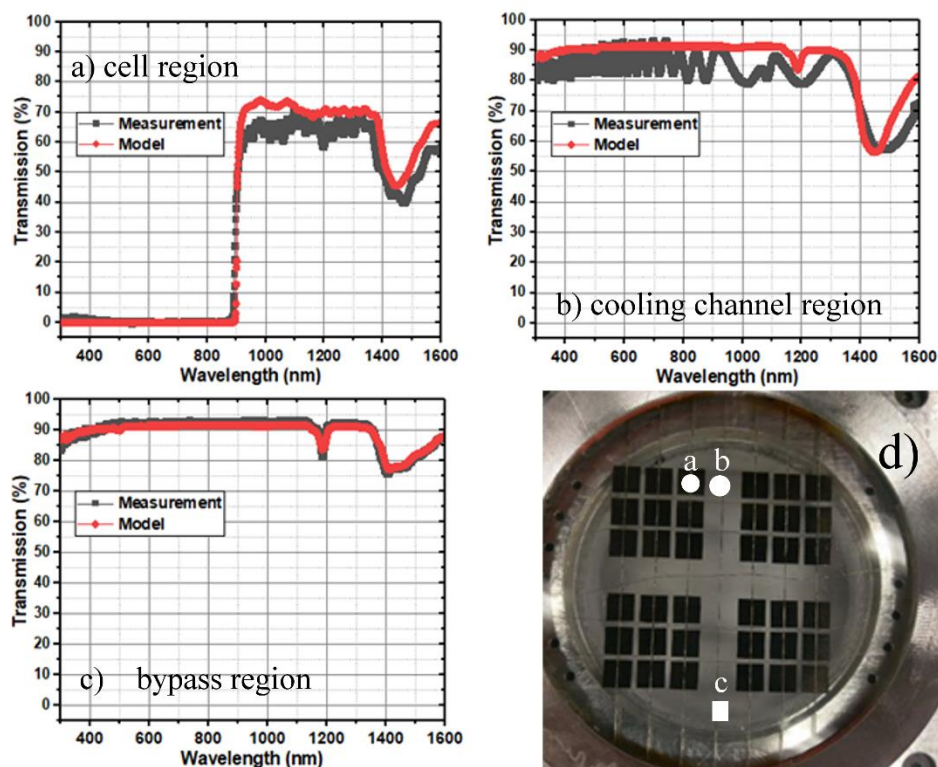
Figure 5-5: Indoor transmission measurements comparing optical model and measurement results on (a) cell region, (b) bypass region with channel and (c) bypass region, with no cells or cooling channels. d) Locations of each measurement point on the module.

Figure 5-5b shows the transmission of an adjacent bypass region that contains microfluidic water channels and a 500 µm thick PDMS layer, but no cells. Through this region, 85.0% of full-spectrum AM1.5D transmits through. Similar to the cell region, a 1400-1500 nm water transmission dip and a 1200 nm PDMS transmission is seen.[103] The fringes in the measurement are caused by a SiO_2 thin film layer on the fused quartz substrate, which was added to enhance the adhesion between PDMS and quartz. Figure 5-5c shows transmission through the bypass regions without cooling channels, which lack a strong water absorption peak and show 91.7% transmission of AM1.5D light. A small water film is still observed, and a thickness dependent fitted transmission line indicates a

45 μm film of water. These bypass regions are intentionally included in the module to provide spacing between CPV cells and to allow extra light to be transmitted to the thermal receiver. Figure 5-5d shows the locations of the three measurement spots on the module for reference.

Some delamination and hazing of the PDMS encapsulant layer occurred during extended concentrated testing, as shown in Figure 5-6. The delamination also made some of the transmitted light diffuse rather than specular. This decrease in specular transmission after extended trials contributed to the increased heat load from the PV cooling system, although the total transmission to the thermal receiver still remained within 2% of modeled values.
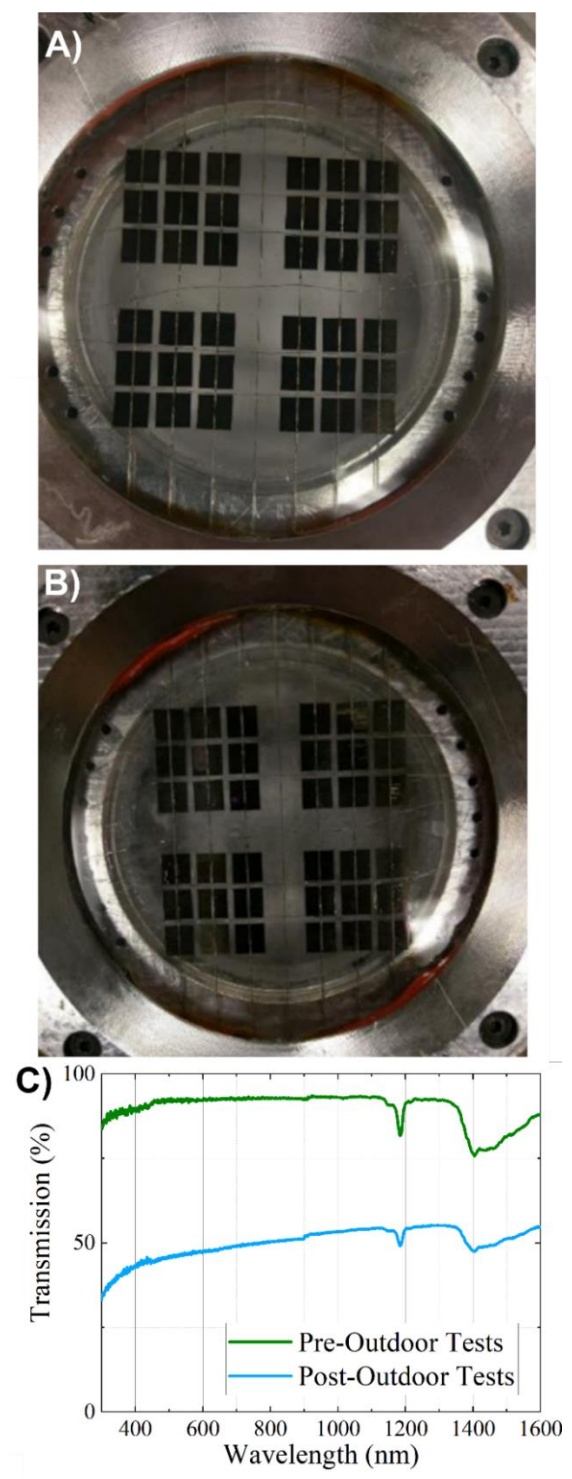
Figure 5-6: A) module 6 before on-sun testing B) module 6 after on-sun testing showing some haziness C) Comparison of module 6 specular transmission before and after high-concentration outdoor testing, with degradation leading to reduced transmission after outdoor testing.

5.4.2 CPV Cooling

During on-sun testing the module active cooling system maintained all monitored cells below the maximum threshold value of 105 ºC. The cells experienced an average temperature of 50 ºC, which matches the model +/- 5 ºC. Minor discrepancies relative to the modeled cooling potential occurred due to ignored effects of convective cooling off the top of the module superstrate, as the calculated natural convective thermal resistance was significantly larger than conduction through the microfluidics (15:1). Contributions of forced convective components due to wind over the surface of the module would reduce the total thermal resistance and therefore the temperature of the cells. Larger differences between predicted and measured temperatures (>10 ºC) are most likely due to the introduction of air bubbles in the encapsulant layer during the manufacturing process or from PDMS delamination during on-sun testing. Additional details can be found in appendix F.

The cooling system extracted a total of 70.6 W of heat from the cells, equivalent to 18.2% of power incident on the module. This power extraction is greater than the predicted 48.4 W and is likely due to larger than expected cell heating. The increase in cell heating is mostly due to an increased heat load from the CPV cells caused by low-efficiency cells, as the thermal model assumed cells operating at in-band cell efficiency of $\eta_c^{IB} = 40.2\%$ efficiency, whereas the batch used in the module performed at $\eta_c^{IB} = 32.0\%$. Furthermore, some cell failures occurred at higher concentrations, also contributing to the extracted heat power from the PV cooling loop. From the model it is expected that 73% of absorbed light is converted into heat while experimental results show the PV cooling makes up ~82% of the CPV power stream (CPV cooling + electric).

5.4.3   Electrical Power

The module was tested outdoors over the course of eleven days, with example all-day

electrical test data shown in Figure 5-7. The tests were performed on days with few

clouds and high DNI in the range of 800-1000 Wm^{-2}, during which the cells experienced

an average concentration of 130 suns. The short-circuit current density, shown in Figure

5-7a, increases by up to 40% of its initial value during the course of a day as DNI

increases during mid-day hours, maximizing around the 200th minute. Open circuit

voltage and fill factor remain approximately constant over the course of a day, as shown

in Figure 5-7b and Figure 5-7c.   Module efficiency, η_m, shows a slight increase at mid-

day and tracks with DNI, as shown in Figure 5-7d. Efficiency values in Figure 5-7d are

lower than expected due to cell failures causing current mismatch between quadrants and

reducing total power output.
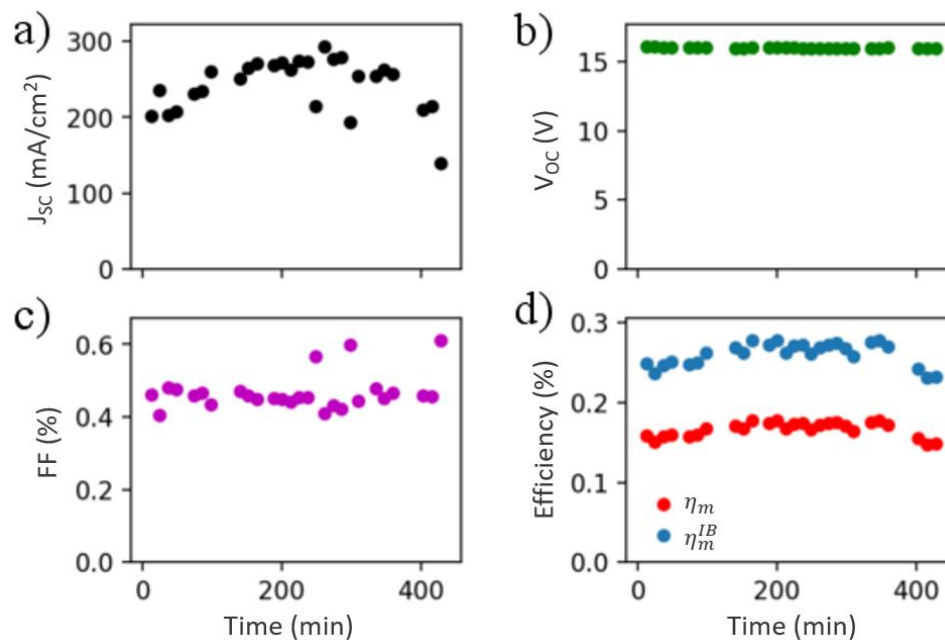
Figure 5-7 Electrical performance of Module 6 over a one-day test at 130 suns average concentration: a) Short-circuit current density b) open-circuit voltage c) % fill factor d) Module efficiency, full-spectrum (η_m) and in-band (η_m^{IB})

The module was also tested under different concentrations; the concentration was varied from trial to trial by selectively masking the concentrator mirror area. Example IV sweeps from different concentrations are shown in Figure 5-8a. The module performed best at 35 suns concentration primarily because no cell failures occurred at that point. At 35 suns, the module showed full-spectrum efficiency of $\eta_m = 21.6\%$ and FF = 78%, with in-band efficiency of $\eta_m^{IB} = 34.7\%$. This module efficiency matches modeled values to within 5%, as shown in Table 5-3; the measured efficiency is slightly higher due, in-part, to cells operating at lower temperatures than predicted. There is also some uncertainty in the input flux to the cells due to momentary fluctuations in the flux distribution relative to the measured flux map (e.g. due to wind, mirror sagging, thermal fluctuations, etc.). In any case, the close match between model and experiment is a noteworthy validation of

module performance, and also indicates that future CPV cell efficiency improvements will enable target module efficiencies of η_m^{IB} = 42.3% by using higher efficiency cells.

At higher concentrations the module performance suffered from CPV cell failures, during which up to 2/3 of all cells suffered from significantly decreased output. These failures caused in-band module efficiency, η_m^{IB}, to drop from 34.7% to 20.3% when raised to 130 suns. IV sweeps from trials at 70 suns and 160 suns show the characteristic shape associated with current mismatch caused by cell failures in different quadrants.[104,105] The short-circuit current showed no signs of deterioration after high-concentration extended testing, but fill factor was reduced from 78.1% at 35 suns to 42.6% under 130 suns. When placed under high concentration, open circuit voltage increased from V_{oc}=13.5 V to V_{oc}= 16.0 V, an increase of 19% relative to 1-sun data in accordance with the relation V_{oc}~log(E_e), where E_e is the irradiance on the cells. From the electrical model, it is estimated that 8.6% of the total power capacity is lost due to current mismatch between the different quadrants caused by asymmetries in the concentrator mirror. A module series resistance of R_{ser} = 370 mΩ and shunt resistance of R_{sh} = 2.3 kΩ were measured during the 35 sun trial.

Figure 5-8b shows the composite PV power output of Module 6 over several days of testing under different concentrations, with power shown as a function of average solar concentration on the module cell area. The modeled electrical power output is represented by the red line. The photovoltaic output matches modeled values to within 5% at low concentrations, but reduced power output from cell failures at higher concentrations causes the module to output at 60% of its expected capacity. Future

module iterations will feature more robust cells and electrical connections to allow

concentration to increase to 500 suns without cell failures.

a)

	1 Sun	35 Suns	70 Suns	160 Suns
I_{SC} (A)	0.017	0.6	1.1	2.8
V_{OC} (V)	13.4	16.0	16.0	16.0
P_{max} (W)	0.146	7.5	9.0	19.1
η_m^{IB} (%)	31.3	34.7	24.1	20.3
FF (%)	64.1	78.1	51.1	42.6
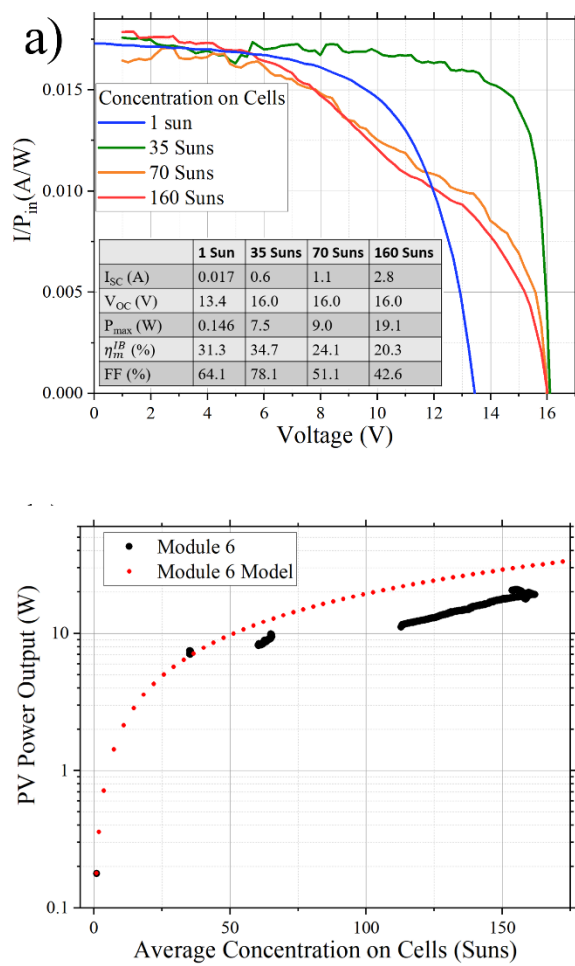
Figure 5-8 a) IV sweeps normalized to input power. b) Total output power as a function of solar concentration on cells, compared to modeled values.

5.5 FUTURE DIRECTIONS FOR MODULE IMPROVEMENT

The key measurements of the module are summarized in Table 5-3, along with

projections of future module performance based on design improvements being

implemented in upcoming iterations. A key limitation of this module was the occurrence

of cell failures at high concentration, preventing the long-term operation of the module at

the target 500 suns concentration. These cell failures were primarily caused when the solder bonds between cells and copper electrodes were damaged from heating and expansion. It is noted that this failure mechanism is largely the result of imperfections traced back to manual prototyping methods, and is expected to be completely resolved as automated module assembly develops. Solder paste is currently applied manually to the busbars of the cells and is prone to spreading over the surface of the cells during curing; this spreading creates both a weak bond and an opportunity for point heating of the exposed solder. To mitigate this problem, future prototype iterations will feature a combination of automated solder pre-form bonding and formic acid fluxes to contain solder only on the busbars and electrodes, which will reduce cell failures under concentration and yield more robust connections. The improved robustness will allow cells to remain active at concentrations of up to 500 suns.

In future modules, transmission will be improved by using chemical primers to enhance PDMS encapsulant adhesion to surfaces and eliminate delamination. Furthermore, UV-resistant PDMS and UV-blocking top glass pieces will prevent UV degradation of the PDMS layer under concentration. Further improvements to the cell ARC will also be pursued in future builds. Finally, diffuse scattering from the backside of the CPV cells can be reduced through improved surface finish during cell fabrication. It is projected that, with these improvements, a total out-band transmission of 65.3% through the cell area of the module can be achieved. By removing the cell's GaAs substrate via epitaxial lift-off, out-band transmission may be improved further to 71.9%. [91]

Additionally, the receiver aperture diameter will be increased from 75mm to 143mm in order to fit all of the light from the dish into the aperture and minimize spillage light

striking the circumferential aluminum collar. This larger aperture will also allow for an

increased number of CPV cells, and 100-cell variants are currently in production. The

increased number of cells is expected to increase receiver efficiency (η_r) from 4% to

10%. Variants with more cells will increase the total power output per module, but will

suffer from efficiency losses due to increased series resistance, and so an optimal cell

number is critical.

Table 5-3 Module 6 electrical and optical performance summary and future projections

	Measured	Modeled (based on Module 6 as-built)	Projected (future module build)
In-Band Cell Efficiency, η_c^{IB} (1 sun, AM1.5D)	32.0%	-	40.2%
In-Band Module Efficiency, η_m^{IB}	34.7% (35 suns)	33.1% (35 suns)	42.3% (500 suns)
Out-Band Transmission (through cell area)	58.8%	62.9%	71.9%

Lastly, the CPV cells used in Module 5 and Module 6 have in-band cell efficiency of η_c^{IB}

= 32.0% at one sun. Next-generation cells have already been made that achieve η_c^{IB} =

40.2% efficiency at one sun.[40] The higher-efficiency cells will be used in future

modules to yield improved electrical performance and reduced cell heat loads. We

anticipate that with these cells, in combination with the previously mentioned module

modifications and 4% quadrant current mismatch loss, we will achieve η_m^{IB} = 42.3% and

η_m= 26.3% based off of Module 6 on-sun performance. These expected performance

values will make this tCPV/T system price-competitive, in many locations, compared to

established electrical and thermal energy generation systems, such as natural gas boilers,

grid electricity, and side-by-side flat-plate-PV and CSP, bringing about a new wave of combined heat and power and zero-net-energy solar energy opportunities.[100]

5.6 SUMMARY

This chapter presents the design and field testing of a spectrum-splitting CPV module that is optimized to convert in-band light ($\lambda < 870$ nm) to electricity and to transmit out-band light ($\lambda > 870$ nm) to a thermal receiver. The module was tested and validated outdoors at an average concentration of 130 suns across 11 days. The results of outdoor testing show 58.8% transmission of out-band incident light (through cell area) and in-band module electrical efficiency of $\eta_c^{IB} = 34.7\%$, in good agreement with modeled values. By using transmissive photovoltaic elements, the PV and thermal components are thermally decoupled, allowing for optimal cell efficiency at low cell temperatures and heat collection at temperatures far exceeding that of the cells. Transmissive active-cooling water channels maintain CPV cells at an average temperature of 50 ^{o}C while allowing for extraction and possible utilization of excess PV heat. Total module power flows match well with modeled values, with 52.7% of incident light transmitting through the module, 18.2% captured in the CPV cooling system, and 4.1% converted to electrical power. Several degradation mechanisms were studied, and improvements to module design, tCPV cell transmissivity, tCPV cell efficiency, encapsulant adhesion, and electrical robustness will be implemented to improve performance and reliability of future modules. This first outdoor test of a spectrum-splitting tCPV module validates the design concept and opens opportunities for a wide range of full spectrum solar conversion applications.

6 CONCLUSIONS AND OUTLOOK

In this thesis, we have detailed two promising routes for future photovoltaic innovation: 2D TMDC-based photovoltaics, and IR-transmissive photovoltaics. In the case of 2D TMDC's, we have developed two new large-area growth techniques designed to improve the availability of wafer-scale MoS_2 for optoelectronic applications. We have also used these grown materials to fabricate electronic devices. We subsequently developed optoelectronic devices such as photodetectors to demonstrate their validity for photovoltaic applications. Secondly, we have used previously-developed IR-transmissive photovoltaic cells to build a spectrum-splitting transmissive PV module, and have demonstrated its performance under concentrated sunlight in an outdoor testbed. These projects all represent distinct advances in their respective fields, and in the field of photovoltaics as a whole. In the coming years, it is expected that these projects will continue under the work and guidance of the next generation of researchers. We therefore dedicate this conclusion chapter to both a final summary of the work accomplished here, as well as a future outlook for these respective research areas.

6.1 THERMAL VAPOR SULFURIZATION FOR 2D MoS_2 GROWTH

In chapter 2 we described a growth technique called thermal vapor sulfurization (TVS), a 2D MoS_2 growth technique that is particularly well suited for large-area growth with precise control of thickness. This thickness control was shown to hold true down to the monolayer of MoS_2. The monolayer MoS_2 growths were shown to have a thickness of 0.738 nm, consistent with the expected value of 0.65 nm per layer. In addition, the

samples were shown to have Raman peak spacing of 20 cm^{-1}, further confirming monolayer thickness. TVS was also used to synthesize other thicknesses, including bilayer, trilayer, and 4-layer MoS$_2$, and the transition from bulk to monolayer was accompanied by the expected two order of magnitude increase in photoluminescence output. However, the great weakness of TVS growth in general is the relatively small domain size of the polycrystalline samples. The domain size of TVS-grown samples was shown via TEM to be 5 to 20 nm, consistent with other reported TVS-derived techniques. The detrimental symptom of this small domain size is a relatively low carrier mobility of $\mu_{EF} = 0.05$cm^{2}V^{-1}s^{-1}. The low mobility will handicap TVS growth for use in electronic and optoelectronic applications unless vertical devices can be made such that the carrier diffusion length is on the same size order as the crystal domains, as discussed in section 4.3 in detail. Overall, TVS is a growth option with the advantage of consistent cm-scale substrate growth coverage, precise layer control, and good optical quality. The disadvantage of TVS is small crystal domain size, which hinders electronic performance.

6.2   RAPID THERMAL REDUCTION 2D MoS$_2$ GROWTH

In an effort to increase the speed and throughput of 2D MoS$_2$ growth, we also described the development of a new growth technique called rapid thermal processing (RTP) in chapter 3. Where virtually all other large-area 2D MoS$_2$ synthesis techniques require at least six hours of thermal processing time, the RTP technique requires only 15 minutes. This reduction in process time leads to an equally dramatic increase in MoS$_2$ growth throughput. Dozens of growths can be performed per day on a single RTP growth instrument, whereas traditional growth could achieve one or two growths per day. This increase in throughput leads to more opportunity for optimization, and also a larger

supply of MoS_2 available to researchers and developers. The MoS_2 was shown to be of comparable quality to TVS, with a carrier mobility of $\mu_{EF} = 0.022$ cm^{2}V^{-1}s^{-1} and with the expected photoluminescence output. The low mobility is an indicator that RTP growth also suffers from small domain size, similar to TVS, and is similarly best suited for vertical device architectures. Thickness control using the RTP technique is more difficult than with TVS due to its solution-processed nature, especially if monolayer MoS_2 is desired, although monolayer may be possible with a sufficiently optimized process. In general, RTP gives MoS_2 of a similar quality as TVS and other growth techniques, but at a far higher throughput that will benefit the capacity of 2D TMDC research as a whole.

6.3 FUTURE TMDC GROWTH DISCUSSION

While we have developed and described two unique and powerful 2D MoS_2 growth techniques, much work remains to be done before MoS_2 is available in sufficient quantity and quality for developers. In particular, efforts to improve the carrier mobility and electrical quality of grown MoS_2 are imperative, while not sacrificing the valuable qualities of throughput capability and molecular layer thickness control. One unique avenue for this is to use growth substrates that are lattice-matched to MoS_2, such as sapphire or doped Si_3N_4. It has been shown that, if properly epitaxially grown, domain boundaries exist without strain or bond misalignment, and therefore do not contribute to detrimental defect-induced carrier recombination.[30,49,106] We therefore believe that epitaxially grown MoS_2, whether through TVS, RTP, CVD, or some other means, is a crucial pursuit that may alleviate the constant issue of low carrier mobility. We also suggest a shift from lateral device architectures to vertical device architectures to minimize the effect of polycrystalline samples, especially for photovoltaics, as discussed

in chapter 4. Lateral devices have been the standard 2D device architecture since the discovery of graphene in 2004 due to their simplicity to fabricate, but their usefulness for photovoltaics has reached its practical limit, and vertical devices represent a new and mostly unexplored direction for improved 2D devices. Finally, as these photovoltaics are developed, we suggest honest comparisons between 2D photovoltaics and traditional PV to determine the impact 2D PV will have on its relevant applications.

6.4 SPECTRUM-SPLITTING SOLAR COLLECTION TECHNOLOGIES

In chapter 5 we discussed the development and testing of a transmissive spectrum-splitting concentrator solar system. Unlike the fundamental research of 2D materials, the development of this concentrator module and system has the potential for commercial applications within the next few years, which motivates this study. The critical innovation of the system is the ability to convert high-energy photons to valuable electricity using photovoltaics, while capturing low-energy IR photons as heat using a thermal receiver. This ability to collect the entire spectrum enables 75% of the solar spectrum power to be collected, higher than conventional photovoltaics achieve. The system also uniquely offers both high-temperature thermal energy and electricity using low temperature, efficient cells from a single system with a shared infrastructure, allowing for reduced installation area and increased land use efficiency. Furthermore, the high-efficiency power collection is expected to yield electrical and thermal power at prices competitive with current electricity and natural gas prices.[100] This first prototype used a relatively small number and density of photovoltaic cells in its aperture, leading to a relatively small receiver electrical efficiency of $\eta_r = 4\%$. However, as detailed in chapter 5, the receiver efficiency is expected to increase to 10% by using a larger number

of cells and by implementing previously-developed higher-efficiency cells. Increasing the cell density will also increase the receiver efficiency, but with the tradeoff of lower thermal power. These efforts are short-term roadmap goals; however, a key purpose of this research is to demonstrate the viability of such a transmissive system in general, and a scale-up of all components could lead to commercially viable systems. Critical to this goal is improving the reliability of the system, as cell failures at high temperatures led to severely reduced power outputs. A long-term pilot-scale field demonstration at full-scale will prove out the innovations put in place to extend the longevity of the module and system.

6.5 FINAL THOUGHTS

It is my sincere hope that the work performed over the past five years, and detailed in this dissertation, may be of value to future generations of scientists and engineers. As with all technologies, their ultimate value will be their usefulness to humanity, and it is by this metric that the innovations presented in this thesis must be judged. In due time, this judgement will reveal itself, and I excitedly wait to see what role 2D materials will play in our future technological advancements, and in what way spectrum-splitting solar collection becomes implemented.

Appendix A   TVS MoS₂ Growth Notes

The TVS process, as described in chapter 2, placed unreacted molybdenum-coated substrates in the left, 830°C side of a tube furnace and powder MoS_2 in a crucible in the right, 900ºC side of the tube furnace. Argon carrier gas was flowed from right to left through the tube, with its flow rate controlled by a mass flow controller (MKS). On the left (downstream) side, past the end of the furnace, a rotary vane roughing pump (Leybold Trivac, 8.5m³/hr) is used to keep the system under vacuum for the duration of the process. MoS_2 powder was used as an alternative to S powder as the S source for several reasons, but primarily because it produces a near-ideal rate of sulfur vapor release at 900ºC; this makes the reaction very quick to optimize and also more stable for monolayer-thickness growths. In addition, MoS_2-based growths leave significantly less sulfur residue on the sides of the reaction chamber, allowing for faster cleanup and longer lifetimes of instrumentation.

In order for MoS_2 synthesis to be reliably achieved, certain growth parameters must be carefully monitored and recorded. These parameters were optimized during the course of this study.

1. Molybdenum precursor thickness: See section 2.1.2

2. Temperature: The temperature of the samples was optimized to produce samples with the greatest optical quality. Ultimately, a furnace temperature of 830ºC was chosen. It was found that temperatures significantly lower (assuming the same precursor mass, heat duration, and flow rate) insufficiently sulfurized the molybdenum film, resulting in some patches of residual molybdenum. These patches were detrimental to both the electronic and optical properties of the

sample. Similarly, as hotter temperatures, a thermal etching effect occurred, which acted to remove some regions of MoS_2. $830°$ was therefore chosen because it maximized molybdenum conversion while minimizing thermal etching.
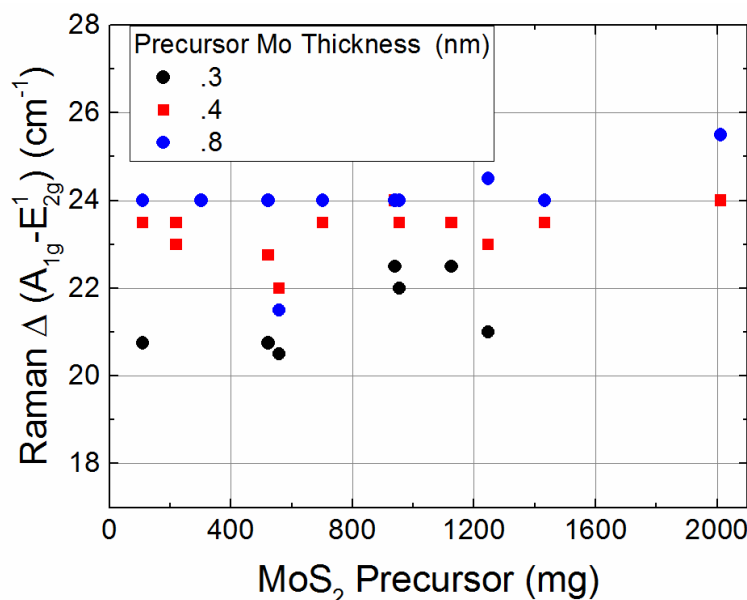

Figure A-1: Raman delta values of three Mo precursor thicknesses as a function of MoS_2 powder precursor mass. It was found that increasing MoS_2 powder precursor increased the thickness of the resultant MoS_2 films, a phenomenon that is most evident for the thin 0.3nm precursor Mo films.

3. MoS_2 powder precursor: During growth optimization, it became clear that the amount of powder MoS_2 was proportional to the partial pressure of sulfur in the reaction chamber and therefore affected the rate of the reaction. Figure A1 displays Raman delta as a function of MoS_2 precursor mass for three different precursor Mo thicknesses. The results show that increased MoS_2 powder precursor yields thicker overall MoS_2 films, a phenomenon more obvious for the thinner Mo precursor films. One explanation is that increased MoS_2 precursor

leads to increased sulfur partial pressure, and therefore yields more complete reactions. Trials with less initial MoS_2 are more likely to contain unreacted molybdenum, which would result in thinner overall MoS_2. Increased sulfur content likely converts the Mo film to MoS_2 more quickly, converting it to MoS_2 before it can be etched by trace atmospheric oxygen. This explains why the effect of increasing precursor mass is more pronounced for thinner samples, which have a larger surface-to-volume ratio and would therefore be more susceptible to thermal or chemical etching.

4. Argon flow rate: The flow rate of Ar carrier gas was modulated using an MKS 200 sccm mass flow controller (MFC). A standard flow rate of 50 sccm is used in the trials displayed in the manuscript; however optimization trials revealed that modulating the flow rate affected the growth. The flow rate affected the pressure in the chamber, with 50sccm Argon yielding chamber pressure of 579 mTorr, 5sccm yielding values close to the base pressure of 50 mTorr, and a 200 sccm flow rate subsequently yielding chamber pressure up to 5torr. While these values are likely to fluctuate based on the dimensions and configuration of individual CVD systems, it was found that increasing flow rate had an effect similar to increasing the MoS_2 precursor mass, exposing the molybdenum precursor to more sulfur and increasing the reaction rate.

5. Pressure: The pressure of the vacuum chamber can be adjusted by changing the Ar carrier gas flow rate, or also by throttling the pump inlet using a valve. Nominal trials were performed at 479mTorr, but results from a higher-pressure, ~5 Torr trial, yielded long, thick single crystal MoS_2, as shown in Figure A-2.

These crystals reached hundreds of microns in length and may be of use for some non-2D applications calling for single crystal bulk MoS_2. It was generally seen that higher pressure favored thicker crystal growth, however lower pressure needed to be balanced with sufficient carrier gas to permit thin-film MoS_2 growth.
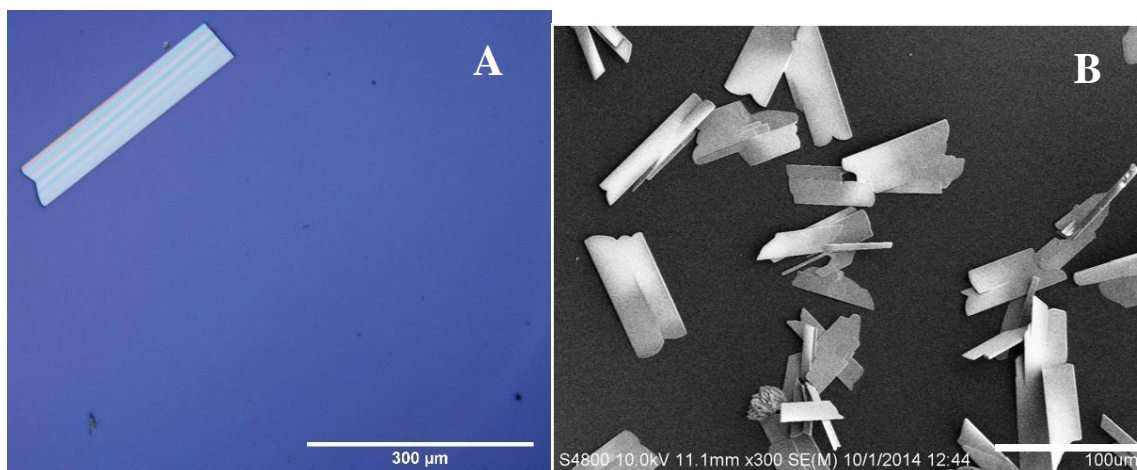

Figure A-2: Long MoS₂ crystals synthesized under higher pressure (>5 torr) TVS trials viewed under (A) optical microscope and (B) scanning electron microscope

6. Soak time: Nominal TVS treatments ramped for 90 minutes and soaked at 830°C (left, samples) and 900 °C (right, MoS_2 powder precursor) for 15 minutes. It was found that increasing the soak time to 20 minutes slightly improved the photoluminescence of some samples, but that increasing the soak time beyond 25 minutes resulted in significant etching of the MoS_2 surface and subsequent deterioration of its properties.

7. Oxygen treatment in-situ: It was found that by flowing small amounts of O_2 into the furnace during the reaction, a controllable etching effect took place that could be used to produce monolayer MoS_2. Although this technique was not used for

the trials reported in this manuscript, it showed some promise for modulating the thickness of final MoS$_2$ by adjusting only the O$_2$ flow rate. As seen in Figure A-3, increasing the oxygen flow rate showed a steady increase in carrier mobility, and a sharp spike in photoluminescence quantum efficiency was seen at ~0.011 sccm O$_2$. These results are explained by the oxygen in the reaction etching and smoothing the MoS$_2$. Some O$_2$-modulating trials also yielded relatively high field effect mobilities of $\mu_{EF} = 0.17$cm^{2}V^{-1}s^{-1}. However, these results proved difficult to reproduce, ultimately resulting in the modulated oxygen flow being phased out of the growth process entirely to improve stability and reproducibility.
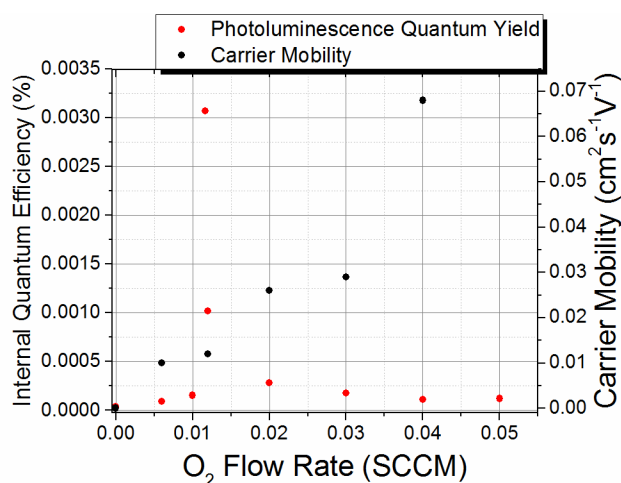

Figure A-3: The effect of oxygen flow on the photoluminescence Internal Quantum Efficiency and carrier mobility of grown MoS$_2$.

Furthermore, in later trials, it became apparent that, even by replicating the same growth parameters listed above, the MoS$_2$ films were under-sulfurized. It is believed that subtle differences in oxygen content of the growth chamber have profound effects on the MoS$_2$ growth, and this oxygen content can be affected my microleaks, pump performance, and humidity. It is suggested that the sulfur partial pressure be increased in future trials in

order to account for this effect. The sulfur partial pressure can be increased by either increasing the amount of sulfur precursor (MoS_2 powder or Sulfur powder), or by increasing the temperature of the precursor during the reaction. This may result in more sulfur depositions on the wall of the chamber, but will help guarantee the correct MoS_2 stoichiometry.

Appendix B   RTP MoS$_2$ Growth Details

Below are listed additional details that are key to a deeper understanding of, or

reproduction of, the RTP results presented in chapter 3.

Precursor Solution Processing

Several techniques were developed to yield high-quality spin-coated $(NH_4)_2MoS_4$

precursor films. For example, it was found that surface treatment of substrates with O_2

plasma was required for the precursor solutions to adhere to the substrate. This is likely

due to the polarity differences between the ethylene glycol-based solution and the SiO_2

and sapphire substrates. Five minutes of treatment within an O_2 plasma cleaner is

sufficient to activate the surface of the SiO_2 and sapphire and promote adhesion. The

effect from the plasma treatment generally lasts only a few minutes, and so immediate

spin-coating after plasma treatment is necessary. In general, the longer a substrate is

treated by O_2 plasma, the better the precursor adhesion during spin-coating. The

development of new and improved adhesion promotion steps will be of great use for this

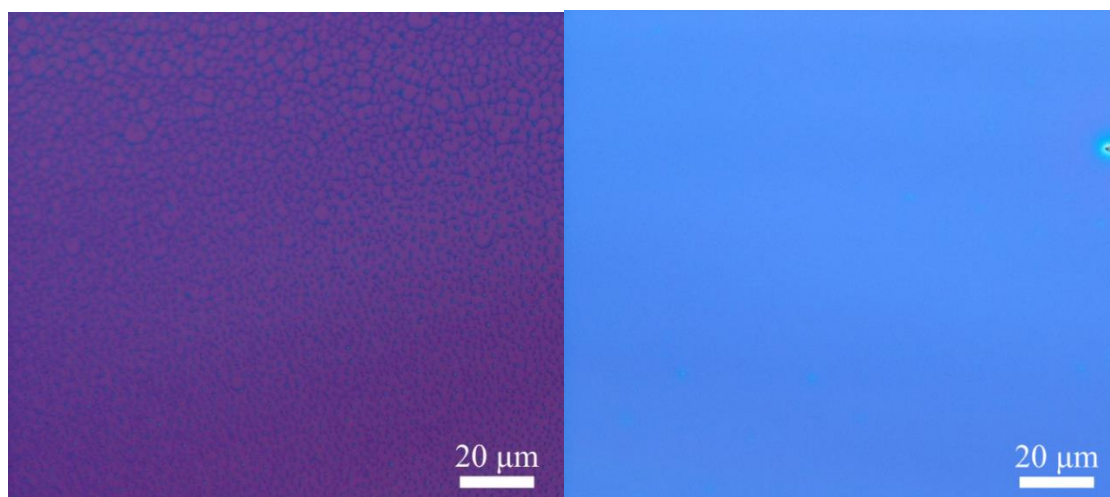growth technique and should be pursued in the future.

Figure B-1. (left) Spin-coated precursor films from magnetic stir bar-mixed solutions and (right) from ultrasonicated solutions showing that ultrasonicated solutions have improved uniformity

It was found that mixing the $(NH_4)_2MoS_4$ ethylene glycol solution using a magnetic stir bar for 12 hours did not sufficiently dissolve the $(NH_4)_2MoS_4$, leading to spinodal decomposition and non-uniform islanding and beading of spun-on films, as shown in B-1 (left). In order to sufficiently dissolve the precursor, it was necessary to submerge the solution vial in a sonicator bath for 20 minutes. No magnetic or other mechanical stirring was used, and the process eliminated the non-uniformity of the spun films, as shown in Figure B-1 (right).
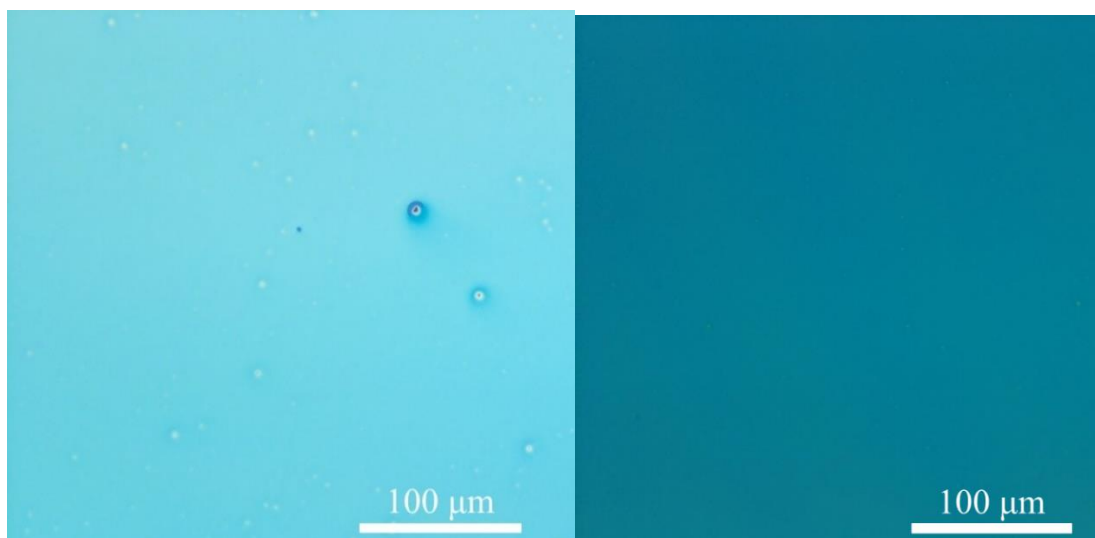
Figure B-2. (left) Unfiltered precursor films show high density of pores caused by particulates; (right) Pore density is greatly reduced by passing the precursor solution through a 220 nm membrane filter prior to spin-coating

Spin-coating substrates with as-mixed solutions resulted in a high density of pores in the spun-on films, as shown in Figure B-2 (left). The pores ranged in size from a few hundred nanometers to tens of microns, and usually contained a visible nucleus in the center of the pore which contained a physical particle. The pores were formed when particulates within the precursor solution, either from undissolved $(NH_4)_2MoS_4$ or external contaminants, were deposited on the surface and absorbed surrounding solution. To mitigate this effect, solutions were passed through a 220 nm membrane syringe filter after solution mixing and prior to spin-coating. After passing through the filter, spun-on solutions had a greatly reduced occurrence of pores, both in size and density, as shown in Figure B-2 (right). However, a small number of pores still exist, and further treatments to resolve this issue should be an area of continued study.

Using two mass flow controllers, the samples were exposed to 5% H_2 gas during the first heating step, T_1. This was done to both accelerate the reduction of MoS_4 to MoS_2 (equations 1 and 2 in main text) and also to remove water and oxygen from the process gas to prevent MoS_2 oxidation. It was found that adding additional hydrogen beyond 5% did not affect the quality of the grown MoS_2, but increased the combustion risk in the chamber, so 5% H_2 flow was ultimately used for T_1. Consistent with other reports,[64] it was found that flowing any H_2 during the high-temperature T_2 segment resulted in significant or total etching of the MoS_2 layer. Because of this, no H_2 was used during the high-temperature step, although 10 SLM of N_2 were still flowed through the chamber. This lack of H_2 makes the grown MoS_2 prone to oxidation, and a safe reducing gas such as sulfur gas should be implemented in the future to prevent oxidation and improve stoichiometry of the grown MoS_2 films.

Curiously, we found that if T_2 was not sufficiently high (>900 ºC), the MoS_2 films were conductive and did not show any gate response when fabricated into transistors. Trials with T_2 temperatures of 500 ºC to 900 ºC all behaved like electronic resistors. This effect is possibly due to excessive S doping in the film, or some other doping effect. However, relatively little source-drain leakage was seen in trials with $T_1 > 900$ ºC, indicating that these higher temperatures are needed, in contrast to the results found by other researchers.[67]

Sample temperature during the RTP synthesis was measured with a K-type thermocouple in contact with the bottom of the silicon substrate. A thermal model was built to confirm that the MoS_2 on top of the substrate is at approximately the same temperature as that at the thermocouple measurement point.

Appendix C   Luminescence Quantum Yield Measurements

The measurement tooling factor of the luminescence %QY measurements, Ɵ, was calculated using the formula:

$$\theta = \frac{Irradiance\ exiting\ sample}{Irradiance\ reaching\ spectrometer}$$

For the Ɵ calculation, to simulate omnidirectional luminescence typical of samples, a 99% diffuse reflectance standard (spectralon) was used in place of the sample, allowing us to calculate how much diffuse light from the sample reaches the measurement spectrometer. This therefore assumes that all photoluminescent samples act as diffuse light sources and emit in all directions. These calibration measurements were taken at the luminescence wavelength of 660 nm, provided by a tunable supercontinuum laser.
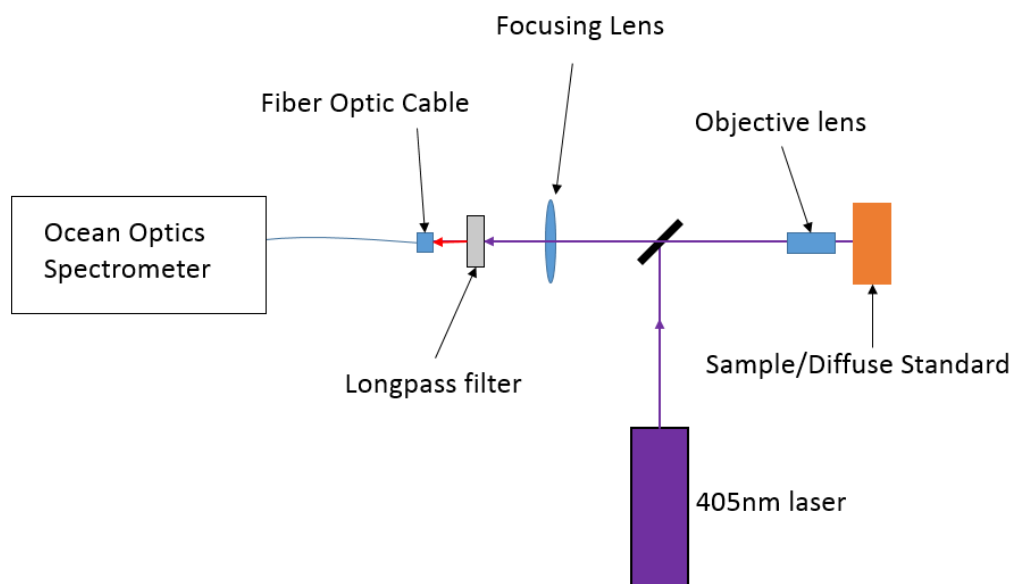

Figure C-1: Diagram of the photoluminescence/quantum efficiency measurement set-up.

Appendix D   *Device Fabrication Notes*

Devices fabricated via Electron Beam Lithography (EBL) are fabricated according to the following process:

1. Submerge sample in acetone for five minutes to clean, dry with dry N_2

2. Submerge sample in IPA, dry with N_2

3. Spin-coat PMMA A7 onto sample, 500 RPM for 15 seconds, followed by 4000 RPM for 45 seconds

4. Anneal on a 100°C hotplate for one minute

5. Pattern desired device pattern using the NPGS software with an area dose of 420

6. Develop lithographed sample in 1:3 MIBK:IPA for 30 seconds, remove and blow dry with dry N_2

7. Inspect developed pattern via optical microscope and optical profilometer

8. Use electron beam evaporation system to deposit desired metal contacts onto sample

9. After metal deposition, submerge sample in acetone and gently agitate for 10 minutes or until all excess metal is removed from the sample

10. Remove from acetone, blow dry with dry N_2

11. Submerge sample in IPA, remove and blow dry with dry N_2

12. Inspect devices under optical microscope

13. Perform electron beam lithography (Hitachi S-3400 SEM + NPGS)

    a. 360 area exposure parameter

14. Develop sample in 1:3 MIBK:IPA developer for 30 seconds

15. Inspect under optical microscope to ensure pattern is completely developed

16. Deposit contact metals (E-beam evaporator, sputterer)

17. Lift-off metal by submerging sample in acetone and agitating for 10 minutes

    a. Note: sonication can be used to quickly remove metal contacts, but may damage delicate 2D samples

18. Rinse sample with IPA and blow dry with dry nitrogen

Appendix E   Device Measurement Notes

The carrier density, n_{2D}, induced by the gate voltage can be calculated using the parallel-plate capacitor model $n_{2D} = C_{ox}(V_g - V_{th})/e$, where C_{ox} is the dielectric capacitance per unit area of the SiO_2 dielectric layer, V_{th} is the threshold voltage, and *e* is the unit charge. C_{ox} can be calculated using $C_{ox} = \varepsilon_0\varepsilon_r/d_{ox}$, where ε_0 is the dielectric constant of vacuum, and ε_r is the relative dielectric constant of 3.9 for SiO_2, and d_{ox} is the dielectric layer thickness of 300nm. Also, the threshold voltage V_{th} is calculated based on the x-intercept of the linear portion of the gate sweep measurements (represented by dotted lines in Figure 2-10).

The field effect mobility μ_{EF} can be calculated using the field effect transistor model:

$$\mu_{EF} = \frac{dI_{ds}}{dV_g} \frac{L}{W C_{ox} V_{ds}}$$

Where W is the width of the channel (9-30 μm in our case), and L is the length of the channel (L=6 μm in our case).